Springer Earth System Sciences

V.P. Dimri *Editor*

Fractal Solutions for Understanding Complex Systems in Earth Sciences

Springer

Springer Earth System Sciences

Series editors

More information about this series at http://www.springer.com/series/10178

V.P. Dimri
Editor

Fractal Solutions for Understanding Complex Systems in Earth Sciences

Springer

Editor
V.P. Dimri
CSIR-National Geophysical Research Institute
Hyderabad
India

ISSN 2197-9596 ISSN 2197-960X (electronic)
Springer Earth System Sciences
ISBN 978-3-319-24673-4 ISBN 978-3-319-24675-8 (eBook)
DOI 10.1007/978-3-319-24675-8

Library of Congress Control Number: 2015950883

Springer Cham Heidelberg New York Dordrecht London

Printed on acid-free paper

Springer International Publishing AG Switzerland is part of Springer Science+Business Media
(www.springer.com)

Dedicated to the Victims of June, 2013,
Kedarnath (Uttarakhand) Tragedy

Foreword

It is with pleasure that I write the foreword to this excellent book entitled "Fractal Solutions for Understanding Complex Systems in Earth Sciences" edited by Professor V.P. Dimri. The book deals with a role of fractals and multi-fractals in understanding problems of earth sciences and their solutions. The chapters on potential fields suggest that mono-fractals or homogeneous functions are scaling function, whereas multi-fractals and multi-homogeneous models have to be dealt separately by specific techniques. Some of the chapters deal with Detrended Fluctuation Analysis (DFA) for better understanding the intrinsic self-similarities for non-stationary well-log geophysical data. The Fractal Differential Adjacency Segregation (F-DAS) is found better than the conventional box counting technique to estimate fractal dimension. Amongst different types of earthquakes analysed, the multi-fractal properties are more pronounced for signals with distinct P, S and coda waves. Finally, an overview of fractal approach to fire problems is worth mentioning.

The editor, Professor Dimri, is to be congratulated on putting together various aspects of fractal and multi-fractal in the problems of earth sciences and their solutions. The book is recommended for the researchers who are using fractals and multi-fractals in earth sciences including seismology. The papers included are important for both fundamental and applied research perspective.

USA Donald L. Turcotte
May 2015

Preface

1. Introduction

The role of fractals in understanding the complex system in earth science has opened a new branch of science applied in geophysics, geology, geomorphology, environment, seismology, etc. (Mandelbrot 1982; Feder 1988; Barton and La Pointe 1995; Turcotte 1997; Dimri 2000, 2005a, b; Dimri et al. 2012). Time series generated by earth sciences observation are in general having long-term persistence with certain degree of correlation. Such correlation can be mapped in terms of fractal dimension for homogeneous models as the mono-fractals. For heterogeneous functions, mono-fractals are not applicable and multi-fractals have been proposed. A typical geological structure such as fault shows a relation with fractal in terms of fault length and displacement of fault zone thickness and throw. Methods such as Detrended Fluctuation Analysis (DFA) and Multi-fractal Detrended Fluctuation Analysis (MDFA) are central to many chapters applied to geophysical well-log data, seismological data and fire time series.

In Chapter "Scaling Laws in Geophysics: Application to Potential Fields of Methods Based on the Laws of Self-Similarity and Homeogeneity", Prof. Fedi systematically described the interpretation of potential field data in a frequency domain. Initially, a relation between random sources (density/susceptibility) and their fields was established which led a spectral analysis method. This method was extensively used by geophysicists for the estimation of depth or thickness of sedimentary basin from gravity and magnetic data. Later, it was found that the source is not a random; rather it is a fractal distribution, and hence, a new method called scaling spectral analysis method was proposed. This method finds its application in interpreting gravity and magnetic data, e.g. Chapter "Scaling Laws in Geophysics: Application to Potential Fields of Methods Based on the Laws of Self-Similarity and Homeogeneity " of this book. On the other hand, the author has elegantly described the homogeneous source distributions called "one point" distributions. Dr. Fedi has proposed, as a multi-homogeneous model, having a variable homogeneity degree versus the position. He concluded that while mono-fractals or homogeneous functions are scaling functions, multi-fractal and multi-homogeneous models are necessarily described within a multi-scale data set and recommended that specific techniques are needed to manage the information contained on the whole multi-scale data set.

In another Chapter "Curie Depth Estimation from Aeromagnetic for Fractal Distribution of Sources", Dr. Bansal et al. described scaling spectral method for estimation of Curie depth. The earth's magnetic field is used to find depth of anomalous sources as shallow as few metres to tens of km. The deepest depths found from magnetic field sometimes correspond to Curie depth a depth in crust where magnetic minerals lose their magnetic field due to increase in temperature. Estimation of depth from magnetic/aeromagnetic data generally assumes random and uncorrelated distribution of magnetic sources equivalent to white noise distribution. The white noise distribution is assumed because of mathematical simplicity and non-availability of information about source distribution, whereas from many borehole studies around the world, it is found that magnetic sources and also other physical properties such as density, conductivity, etc. follow fractal distribution. The fractal distribution of sources found many applications in depth estimation from magnetic/aeromagnetic data. In this chapter, Curie depth estimation from aeromagnetic data for fractal distribution of sources has been presented.

In Chapter "Fractal Faults: Implications in Seismic Interpretation and Geomodeling", Dr. Ravi Prakash Srivastava has combined the concept arrived from two different words, one called "Fractals" that follows scaling law seen in many natural phenomenon and the other called "Faults" encountered in geological studies. Author presented most updated use of fractal concept in geological understanding of faults and their significance in geological modelling of hydrocarbon reservoirs. It is reported in many studies that the faults show fractal/scaling behavior in terms of fault length and displacement fault zone thickness versus fault throw. However, large faults are identified and integrated in seismic data, but same is not true when they are small and hence below the resolution limit of seismic data. Thus, author is able to map smaller faults with geological knowledge of the faults in the reservoir model studies using a concept of fractals.

In Chapter "Detrended Fluctuation Analysis of Geophysical Well-Log Data", Subhakar and Chandrasekhar used geophysical well-log data as it provides a unique description of the subsurface lithology as well as they represent the depositional history of the subsurface formations, vis-à-vis the variation of their physical properties as a function of depth. For this, DFA technique has been described and applied to gamma-ray log, sonic log and neutron porosity log of three different wells from west coast of India. The whole chapter is organized in seven sections dealing with geology of the area, data used in the present study, basic theory of DFA, methodology used, discussion and interpretation of results derived and finally the conclusion of the studies.

Drs. Banerjee and Nimisha Vedanti in Chapter "Fractal Characters of Porous Media and Flow Analysis" proposed a fractal model of continuum percolation which quantitatively reproduces the flow path geometry. Porosity is an important property of geological formation and a complex function of many variables which control fluid flow. The variables include essentially the characteristics of pore structures such as type, size, shape and arrangement of pores; pore space connections; area of pores open for flow; and tortuosity of the flow paths and composition of pore. There is no general framework which explains the fluid flow through the fractured and complex subsurface geometry. In fact, a direct measurement of flow through complex permeable media is time taking; hence, an analytical model has been recommended. Therefore, the aim of this chapter is to develop a simple analytical model based on the medium structural characteristics to explain the flow in natural fractures. The authors showed that the pattern of fracture heterogeneity in reservoir scale of natural geological formations looks as the distributed self-similar tree structures.

In Chapter "Estimation and Application of Fractal Differential Adjacency Segregation (F-DAS) Scores in Analysis of Scanning Electron Micro Graph (SEM) Imageries Towards Understanding the Adsorption unto Porous Solids", Prof. Das et al. presented Fractal Differential Adjacency Segregation (F-DAS) which is different from the conventional approach for estimation of fractal dimension (FD) using box counting method. The box counting method is one of first methods to estimate fractal dimension and is also simple to use. However, for heterogeneous system, mono-fractal seems to be inappropriate. In this chapter, the limitation of use of mono-FD is explained and thus extended the concept of Fractal dimensioning into lower scale segregation levels and evaluating their differential scores. In this approach, F-DAS scores are estimated for each of the image pixels of scanning electron microscopy (SEM) imageries using the arithmetic means of the grey levels of the adjacency pixels enclosed by the box used for counting in the conventional methods. The authors claimed that the present analysis provides better understanding of variability of the system (in this case, adsorbents), unexplored by qualitative analysis of SEM imageries, as well as the functional groups using Fourier transform infrared spectroscopy.

Dr. Padhy in Chapter "The Multi-fractal Scaling Behavior of Seismograms Based on the Detrended Fluctuation Analysis" has explained the use of the multi-fractal scaling properties of seismograms in order to quantify the complexity associated with high-frequency seismic signals and hence to characterize medium heterogeneities at different scales. He recommended the MDFA method is capable of characterizing the multi-fractality of earthquake records associated with frequency- and scale-dependent correlations of small and large fluctuations within seismogram. The multi-fractal nature of earthquake records has been explained by computing the generalized Hurst and mass exponent and multi-fractal singularity spectrum. One of the findings is that the degree of multi-fractality decreases with increasing frequency, and is generally more for the time period windowing dominant seismic phases in the seismogram.

Finally in Chapter "Fractal Methods in the Investigation of the Time Dynamics of Fires: An Overview", Prof. Telesca reviewed the fractal methods applied to fire point processes and satellite time-continuous signals that are sensitive to fire occurrences. Fires represent one of the most critical issues in the context of natural hazards. Most of these fires could be natural as well as anthropic. Sometimes, summer drought can influence the ignition and spread of devastating fire.

The author gave very good description of methods to find the temporal distribution of sequence of fire. These methods include coefficient of variation (CV), Detrended Fluctuation Analysis (DFA) and Multi-fractal Detrended Fluctuation Analysis (MDFA). Other techniques such as Fano Factor (FF), Allan Factor(AL) and Count-based Periodogram (PG) for fire sequence as the count process has also been described through fire satellite time series. Author also applied these methods to know the information about the "health" of vegetation which is very important and can be used to find the status of vegetation after the big forest fire.

2. Acknowledgments

I am grateful to all contributors who wrote very relevant and significant chapters for this book. I am also thankful to all reviewers who took so much pain in completing the review process in time.

I shall always be grateful to Prof. D.L. Turcotte, USA, who wrote a very encouraging foreword for the book. I thank my Ph.D. students Mr. Shib S. Ganguli and Ms. V. Uma, and colleague Mr. P. Nagarjuna, for helping me in editing the book.

Thanks are due to Indian National Science Academy (INSA) for granting INSA Senior Scientist while writing this book. CSIR-National Geophysical Research Institute has provided me the necessary facilities for completion of this book.

I am also thankful to Ms. Schwarz Johanna, Sangeetha and others from Springer publishers for bringing out this issue as per schedule.

V.P. Dimri

References

Barton CC, La Pointe PR (1995) Fractals in the earth sciences. Plenum Press, New York, p 265

Dimri VP (2000) Edited: application of fractals in earth sciences. A.A. Balkema, USA; Oxford and IBH Pub. Co., New Delhi, p 238

Dimri VP (2005a) Edited: fractal behaviour of the earth system. Springer, New York, p 207

Dimri VP (2005b) Edited: fractals in geophysics and seismology: an introduction; fractal behaviour of the earth system. Springer, New York, pp 1–22

Dimri VP, Srivastava R, Vedanti N (2012) Fractal models in exploration geophysics. Elsevier Science Ltd., Amsterdam, p 165

Feder J (1988) Fractals. Plenum Press, New York, p 283

Korvin G (1992) Fractal models in the earth sciences, Elsevier Science Ltd, Amsterdam, p 424

Mandelbrot BB (1982) The fractal geometry of nature. W.H. Freeman and Company, New York, p 460

Turcotte DL (2011) Fractals and chaos in geology and geophysics. Cambridge University Press, Cambridge, p 41

Contents

Scaling Laws in Geophysics: Application to Potential Fields of Methods Based on the Laws of Self-similarity and Homogeneity

Maurizio Fedi

Abstract We analyse two classes of methods widely diffused in the geophysical community, especially for studying potential fields and their related source distributions. The first is that of the homogeneous fractals random models and the second is that of the homogeneous source distributions called “one-point” distributions. As a matter of fact both are depending on scaling laws, which are used worldwide in many scientific and economic disciplines. However, we point out that their application to potential fields is limited by the simplicity itself of the inherent assumptions on such source distributions. Multifractals are the models, which have been used in a much more general way to account for complex random source distributions of density or susceptibility. As regards the other class, a similar generalization is proposed here, as a multi-homogeneous model, having a variable homogeneity degree versus the position. While monofractals or homogeneous functions are scaling functions, that is they do not have a specific scale of interest, multi-fractal and multi-homogeneous models are necessarily described within a multiscale dataset and specific techniques are needed to manage the information contained on the whole multiscale dataset.

1 Introduction

The Earth is a heterogeneous medium, meaning it is characterized by a complex distribution of its physical properties. In general, a proper representation of its complexity has to explicitly refer to the specific scale of observation of a given phenomenon. To this regard, a special class of phenomena share a scaling property: that of not exhibiting any characteristic scale. The behavior of scaling phenomena assesses that all the scales within some range are equally important and the signals

---

M. Fedi (✉)
Dipartimento di Scienze della Terra, Università Federico II di Napoli,
dell’Ambiente e delle Risorse Largo san Marcellino 10, 80138 Naples, Italy
e-mail: fedi@unina.it

V.P. Dimri (ed.), *Fractal Solutions for Understanding Complex Systems in Earth Sciences*, Springer Earth System Sciences,
DOI 10.1007/978-3-319-24675-8_1

at different scales are each one related to another. Different types of scaling are known in the literature, including the long-range dependency, self-similarity, fractal statistical similarity (monofractals) and local self-similarity: multifractals and infinite divided sequences. Since there is no characteristic scale, in many areas of science it has been useful integrating models across a broad range of scales.

Earth's physical parameters, such as magnetic susceptibility, resistivity or others, have been studied within the frame of fractals. At the same time, potential field anomalies (gravity, magnetic, self-potential) have been studied under the framework of scaling laws based on the homogeneity law. In particular, multiscale methods, such as the continuous wavelet transform (CWT), will be specifically designed to study field anomalies exhibiting such scaling properties.

In this paper, we will try to analyse these two kinds of scaling laws in parallel, in order to define their similarities, limitations and advantages for determining the properties of the potential field sources.

2 The Fractal Scaling-Law in Geophysics

Random fractals are complex signals that, at first sight, seem not to deserve any useful information, due to their too strong erratic behavior. However, valuable information may be achieved if, instead of exploring the signal at a fixed scale, we try to search for a relationship existing between the observations of the signal at different scales. Scale-invariant fractals, in fact, are uniquely characterized by a single parameter, the fractal dimension, which gives us a description of its type and complexity.

Consider a signal $Y(x)$ and write the self-similarity equation (e.g. Mandelbrot 1983):

$$Y(ax) = a^H Y(x), \quad a > 0, x \geq 0, \tag{1}$$

where $Y(x)$ is a self-similar homogeneous fractal (or monofractal) with $0 < H < 1$. The value of H, referred to as the Hurst parameter, will catch the degree of self-similarity of $Y(x)$. For self-affine processes, the local properties are reflected in the global ones, resulting in the relationship:

$$D + H = q + 1 \tag{2}$$

where D is the fractal dimension and q is the space dimension (e.g. Russ 1994; Muniandy et al. 2003; Gneiting and Schlather 2004).

$Y(x)$ is indeed equal to its scaled version $Y(ax)$ after the normalization by a^{-H}, so that the phenomenon, observed at whatever scale, will present the same information and may be explained by the same model, no matter the scale.

However, for more complex phenomena, reasonable models explaining a given phenomenon at a given scale may be different from those found at a different scale. In this case we may write (for instance, Arneodo 2000):

$$Y(ax) = a^{H(x)} Y(x), \quad a > 0, x \geq 0 \tag{3}$$

where $H(x)$ is now a function of x, so as to allow for more complex scaling behaviors. Consequently, the process is said to be multifractal and the function $H(x)$ is referred to as Holder exponent. While self-similarity describes space scale invariance, which is the permanence of a structure on all scales ruled by a single law independent of x, multifractality captures different behaviors on small and large scales: characteristic features of the signal (for instance, bursts) are detectable on all scales, but they obey different laws depending on x.

Real-world phenomena may be rarely described in terms of simple deterministic fractal models, but similarity can hold on several scales in a statistical sense, leading to the notion of random fractals. As an example, random fractals are the model assumed for well logs: Marsan and Bewan (1999) evidenced a multifractal distribution for the P-wave sonic velocities recorded at the German Continental Deep Drilling Programme (KTB) main borehole and for the gamma log. Fedi (2003) analysed susceptibility data from the deep KTB log and found that a multifractal model was more appropriate than a monofractal one for the statistical modelling of these signals. Power spectra or variogram analysis are in fact useful for the characterization of the signal up to the second-order statistics, but may fail in explaining more complex structures. Fedi et al. (2005) extended this kind of analysis to different geophysical KTB well logs (density, magnetic susceptibility, self-potential and electrical resistivity) and found consistent information about the KTB well geological formations. They characterized the lithological changes of the drilled rocks and identified zones of macro- and microfractures by using a regularity analysis, which maps the measured logs to profiles of Holder exponents, or regularity. Regularity generalizes the degree of differentiability of a function from integer to real numbers and is useful to describe algebraic singularities related not only to the classical model of jump discontinuity, but to any other kind of 'edge' variations.

3 Estimation of the Source Properties Using the Fractal or the Spector and Grant's Scaling-Law

An important issue is linking in a coherent way the complex behavior of the physical properties measured with well logs to other physical quantities, which are related to those parameters, but are independently measured. More clearly, we may define how the complexity of the medium, revealed from well logs of susceptibility, density or wave speed, is mapped to the complexity of fields, like the magnetic field, the gravity field or the seismic wavefield.

Herrmann (1997) evidenced an inhomogeneous scaling for both well-log acoustic waves and reflectivity, so implying that the singularity structure is carried out from space to space-time. Other authors (for instance, Gregotski et al. 1991;

Pilkington and Todoeschuck 1993; Maus and Dimri 1994; Bansal et al. 2010) interpreted susceptibility and density logs in terms of scaling sources and considered their magnetic or gravity fields as scaling quantities, with fractal dimensions related in a simple fashion to the fractal dimension of the source parameters. Naidu (1968), assuming a homogeneous random density sources confined to a thick semi-infinite medium, derived the relationships between the spectrum of the sources and the spectrum of the related gravity or magnetic fields. Pilkington and Todoeschuck (1993) assumed a 3D fractal magnetization, with power spectrum $S_j(k_x, k_y, k_z) = (k_x^2 + k_y^2 + k_z^2)^{\alpha/2}$, $(\alpha < 0)$, and obtained for the field spectrum P:

$$P(s, h_1) = \frac{8(-\alpha - 1)!!}{\pi(-\alpha)!!} \exp(-2sh_1) s^{\alpha + 1} \tag{4}$$

where k_x, k_y, k are angular frequencies; $s = (k_x^2 + k_y^2)^{1/2}$ is the radial wave number; h_1 is the depth of the half-space; P is the power spectrum of the magnetic field vertical component observed on the plane $z = 0$.

Note that, by this approach, the scaling exponent is assumed to vary in the fractal range and, in turn, to depend on geology (Bansal et al. 2011).

However, Fedi et al. (1997) have shown that other kind of correlated sources, such as the magnetically homogeneous blocks, inherently assumed by Spector and Grant (1970), also originate fields whose scaling exponent is in the fractal range, being it equal to about 3. To be clear, Spector and Grant (1970) modelled the susceptibility distribution using independent ensembles of rectangular, vertical-sided parallelepipeds. Each ensemble is characterized by a joint frequency distribution for depth (h), width (a), length (b), thickness (t), magnetization intensity (j/ab) and direction cosines of magnetization. Under the hypothesis that the parameters vary independently and that they are randomly and uniformly distributed about their mean values, the authors derived the well-known analytical expression of the radial power spectrum of the reduced to the pole magnetic field:

$$P(s) = \left(\frac{\mu_0}{2}\right)^2 \bar{j}^2 C(s, \bar{a}, \bar{b}) G(s, \bar{t}) P(s, \bar{h}) \tag{5}$$

where:

$$\bar{j}^2 = \langle j^2 \rangle; \quad \bar{a} = \langle a \rangle; \quad \bar{b} = \langle b \rangle; \quad \bar{h} = \langle h \rangle; \tag{6}$$

$$C(s, \bar{a}, \bar{b}) = \frac{1}{\pi} \int_0^{\pi} \langle S^2(s, \theta, a, b) \rangle d\theta \tag{7}$$

$$S(s, \theta, a, b) = \frac{\sin(as\cos\theta)}{as\cos\theta} \frac{\sin(bs\sin\theta)}{bs\sin\theta} \tag{8}$$

$$G(s,\bar{t}) = \left\langle (1 - e^{-ts})^2 \right\rangle = 1 - \frac{\left[(3 - e^{-2\bar{t}s})(1 - e^{-2\bar{t}s}\right]}{4\bar{t}s} \tag{9}$$

$$Q(s,\bar{h}) = \left\langle (e^{-hs})^2 \right\rangle = e^{-2\bar{h}s} \frac{\sinh(2s\Delta h)}{2s\Delta h} \tag{10}$$

$\theta = \tan^{-1} u/v$ represents the angular direction of the radial frequency vector and the symbol <> stands for ensemble average.

Now, the factor C was shown in Fedi et al. (1997, Fig. 1) to clearly follow a power law of exponent nearly equal to −3 for intermediate-to-large values of $\bar{a}$, while for small values of $\bar{a}$ the spectrum is generally flat at low-to-intermediate wavenumbers and continues to follow the above power law only at large wavenumbers. So, especially for large thicknesses and when measurements are close to the source, the factors Q and G will both tend to 1 and the spectrum decay of the logarithm of power spectrum will be only determined by the power law of C (of exponent equal to −3), according to:

$$P(s) \simeq \left(\frac{\mu_0}{2}\right)^2 \bar{J}^2 C(s,\bar{a},\bar{b}) \tag{11}$$

It is important to stress that it is not correct to consider the Spector and Grant model a random uniform uncorrelated distribution of sources (e.g. Pilkington and Todoeschuck 1993; Ravat et al. 2007; Bansal et al. 2011). As a matter of fact, this model is a statistical distribution of homogeneous sources (prisms) under the hypothesis that the source parameters (thickness, width, depth and others) vary independently and that they are randomly and uniformly distributed about their mean values. Hence, being the sources of the ensemble homogeneous, this is not yet an uncorrelated source distribution, but an ensemble of sources, which are, at least locally, correlated. The misunderstanding may be explained in this way: even though the magnetization factor $\bar{J}^2$ is a constant (i.e. a white power spectrum), the magnetization distribution must instead be defined by the whole product $\bar{J}^2 C(s,\bar{a},\bar{b}) T(s,\bar{t})$, which is a red power spectrum, as discussed above (Eq. 11).

One more misunderstanding (e.g. Ravat et al. 2007; Bansal et al. 2011) is on using the definition of $C(s,\bar{a},\bar{b})$ for making a correction factor (a k^3 spectral correction) no matter the case. This is, in practice, a deconvolution of the spectrum for C, which was originally proposed in Fedi et al. (2007) and Quarta et al. (2000). However, these last authors made it well clear (Fig. 1 in Fedi et al. 2007) that the correction allows an improved estimation of $\bar{h}$ only when anomalies are big enough to justify, roughly, a homogeneous-block kind of source. Therefore, it should not be applied when $\bar{a},\bar{b}$ are too small or, in other words, when most anomalies appear to have in the map a too short wavelength.

To explain a possible spatial variability of the scaling exponent, a relation to different geology units was invoked (Bansal et al. 2011). However, there is still a large amount of ambiguity, as shown by Quarta et al. (2000) who have studied the behavior of fields generated by sources other than fractal and have clearly shown

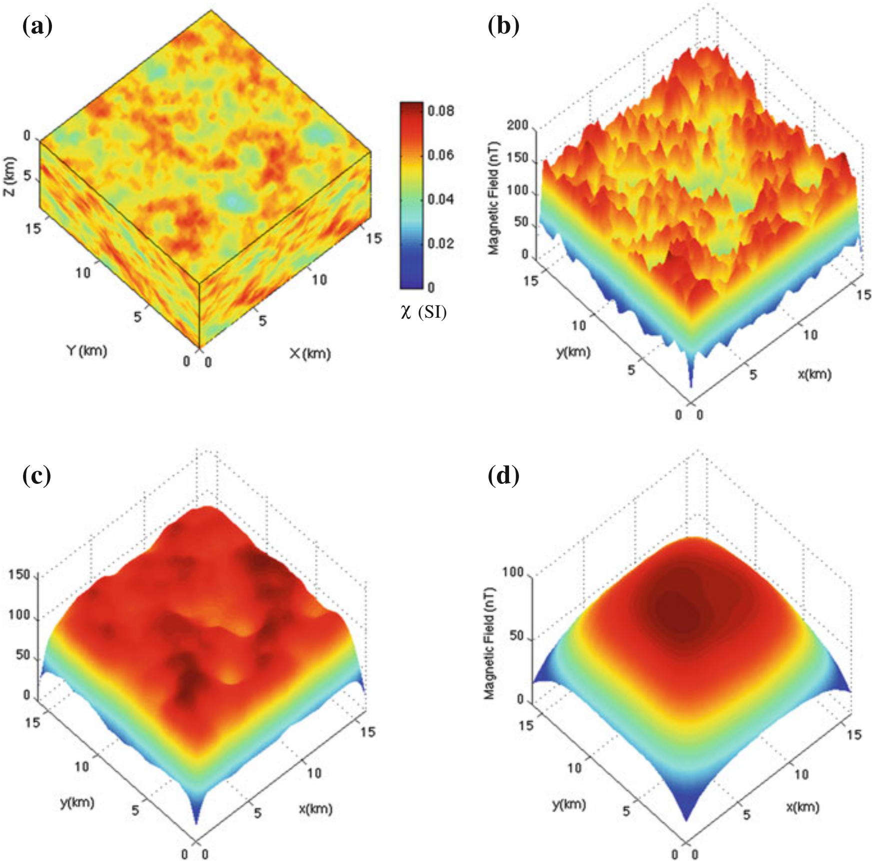

Fig. 1 A fractal 3D homogeneous distribution of magnetic susceptibility (SI), with fractal dimension $D = 3.5$ (**a**) and its generated magnetic fields measured at: a negligible distance (**b**), 0.5 km above the surface (**c**) and 2.5 km above the surface (**d**). As the altitude increases, the information about the fractal distribution is progressively lost

that their spectral scaling exponents can assume values in the so-called fractal range. More specifically, sources with intermediate characteristics between Naidu's (uncorrelated source distribution) and Spector and Grant's (locally correlated source distribution) models will produce fields whose power spectra scaling exponent depends on the ratio between the horizontal extent of the source and the field sampling-interval.

So, to verify the goodness of a fractal source model for experimental data, a simple test could be made, examining the properties of the whitened field at source level, since it must be random when any correlation is removed in the amplitude spectrum.

More recently, Bouligand et al. (2009) have proposed a model of depth to the Curie temperature isotherm from magnetic anomalies in the western United States, based on a fractal model. Their spectral model has a fractal exponent of 3.0, by which the depths to the bottom of magnetic sources were close to the depths to the Curie temperature isotherm derived from heat flow data. However, from the inherent spectral ambiguity discussed above, it is clear that there is no clear evidence that the source distribution is fractal, being it explained well also by a Spector and Grant's model based on relatively homogeneous magnetized blocks.

4 The Homogeneity Scaling-Law in Geophysics

We have described above how scaling laws, of the fractal or multifractal type, are important to model the Earth as a scaling medium and to describe its degree of complexity. In particular, we have seen that either monofractal or multifractal models have been used to describe the well logs of susceptibility, seismic wave speed and other physical properties of the Earth's rocks.

In addition, we have mentioned in the previous section some studies linking, in the Fourier domain, geophysical quantities to physical rock parameters for fractal models. This shows that, besides modelling the direct information coming from the logs of physical properties of the rocks, geophysics may provide much wider and depth-related information through the study of measured quantities, which are related to such properties.

In particular, spectral methods could allow the fractal properties of the source distribution to be estimated from the field. As already said, however, this is possible only when the field is studied very close to the source distribution, so that the Spector and Grant's model becomes (Eq. 11): $E(s)\overset{\sim}{=}\left(\frac{\mu_0}{2}\right)^2\bar{j}^2C(s,\bar{a},\bar{b})$.

This is however also true for other models, such as that of the half-space fractal random noise in Eq. (4) (Naidu 1968; Pilkington and Todoeschuck 1993), which, in fact also assumes the form of a power law:

$$P \cong \frac{8(-\alpha-1)!!}{\pi(-\alpha)!!}s^{\alpha+1}. \tag{12}$$

In order to illustrate better this concern, let us use half-space fractal random noise in order to generate a fractal 3D homogeneous distribution, with fractal dimension $D = 3.5$ (Fig. 1a). The corresponding magnetic field (Fig. 1b), when measured at a negligible distance, is, in effect, very similar to the source distribution, showing an irregular behavior typical of the fractal model. It is so consistent with its power spectrum, fully reflecting the fractalness of the source distribution.

However, when we are only a 0.5 km above the surface, the complexity of the field disappears(Fig. 1c) and when we are at 2.5 km it is completely lost and the field has a nearly regular shape (Fig. 1d): we can only argue that the source volume contains magnetized sources, but any other information about the fractal distribution can no longer be obtained.

This behavior is because the convolution factor related to the depth (Eqs. 4 and 5) is clearly dominant and obscures the other one. So, being this last the most typical situation, we must resort to some other laws, better describing the source distribution. To this end, we will illustrate now the use of other types of scaling laws, widely used in applied geophysics, owning to the homogeneity law

$$f(ax, ay, az) = a^n f(x, y, z) \quad a > 0, \tag{13}$$

where n is the degree of homogeneity and f is a homogeneous function (e.g. Florio and Fedi 2013). As for the fractal scaling law, a key role is again played by the mathematical properties related to the convolution. In fact, geophysical potential fields are mathematically expressed as the convolution of a source-density property with some specific operator. For instance, consider the total-magnetic-field:

$$T(\mathbf{r}_k) = -\frac{1}{4\pi}\frac{\partial^2}{\partial f \partial t}\int_V \frac{|\mathbf{J}(\mathbf{r})|}{|\mathbf{R}|}\mathrm{d}V, \tag{14}$$

where $\mathbf{J}$ is the magnetization intensity, V is the source volume, $\mathbf{R}$ is the distance $|\mathbf{r}_\mathrm{k} - \mathbf{r}|$ between the observation point, at $\mathbf{r}_\mathrm{k}$, and the source points, at $\mathbf{r}$ in V, and $\mathbf{f}$ and $\mathbf{t}$ are, respectively, the main field and magnetization unit-vectors. Since the integral has itself the form of a convolution, its Fourier transform may be simply expressed in the harmonic region as (Maus and Dimri 1994; Caratori Tontini et al. 2009):

$$\tilde{\mathbf{T}} = -\frac{(\mathbf{f}\cdot\mathbf{k})(\mathbf{t}\cdot\mathbf{k})}{|\mathbf{k}|^2}\tilde{\mathbf{J}} \tag{15}$$

where $\mathbf{k}$ is the 3-D wave vector, and $\tilde{\mathbf{T}}, \tilde{\mathbf{J}}$ are, respectively, the Fourier transforms of the magnetic field and of the magnetization.

So, the convolution actually maps the source-density distribution complexity into that of the magnetic field, but this mapping is strongly dependent on the altitude, that is on the scale of observation. Obviously, similar considerations also occur for other integral equations, connecting, for instance, the mass-density distribution to the gravity field or the electric conductibility to the electric and magnetic fields.

If one tries to classify physical source distributions in terms of their complexity, we have so far used statistical models of growing complexity, from fractal to multifractal models. On the other hand, we may use other classes of source distributions to deal with a simplified medium and so describe the source distribution at different levels of complexity. These models may be generated solving the integral (14) or Eq. (15) for homogeneous-density distributions with very simple geometrical shapes, such as spheres, infinite cylindrical or planar distributions.

Many of these simple source distributions fall in the class of so-called one-point sources (Fig. 2), which gained in the last two decades a strong popularity since their

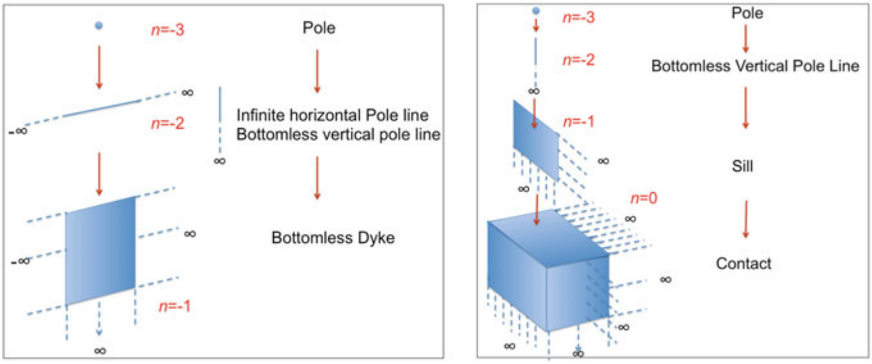

Fig. 2 One-point source models. The magnetic fields of one-point source models obey the homogeneity relation (13) and are each one characterized by a homogeneity degree, n, which may be one of the integer values $\{-3, -2, -1, 0\}$

fields obey the homogeneity relation (13). The one-point sources may be defined as source distribution being entirely characterized by the coordinates of only one special point. For instance, it is well known that the gravity field from a homogeneously dense sphere is equivalent to that of a mass distribution concentrated at its centre, provided the total mass is the same. Hence, the field of such sphere is completely defined by the coordinates of its centre, so that the main interpretative task will be finding a reasonable estimation of them. Other examples of one-point sources are the dipole for magnetic fields, infinitely extended pole and dipole lines, semi-infinitely extended tabular sources for modelling sheet or dykes, and the semi-infinite block model used to simulate the anomalies for contact-like geological structures. All these sources may be approximated by mass (or magnetization) distributions concentrated at their top or at their centre, depending on the source-shape.

Note also that for such homogeneous sources, the estimated n will be one of the integer values $\{-3, -2, -1, 0\}$ and we will be assured of a clear meaning for the estimated depth to the source: it can be referred to the source centre (sphere, horizontal cylinder, sill) or to the top (any other source). This feature makes somewhat different the fractal scaling-law (Eq. 4), in which the Hurst exponent may be any real value $0 < H < 1$(e.g. Turcotte 2011) and the homogeneity law (Eq. 12), in which the homogeneity degree is only integer and within the restricted set: $\{-3, -2, -1, 0\}$. However, it is important to stress that it has been recently shown that homogeneous sources and corresponding fields may exist, whose homogeneity degree may be fractional as well (Fedi et al. 2012; Fedi et al. 2015). They are characterized by having some intermediate properties between those corresponding to two subsequent one-point sources of integer n, as shown in Fig. 3, where the gravity anomalies are drawn for a pole (Fig. 3a), its fractional integration of order $\alpha = -0.5$ (Fig. 3b) and for a bottomless vertical line mass (Fig. 3c). Basing on that, we may so extend the range of allowed homogeneity degrees to any real value within the range: $-3 \leq n \leq 0$.

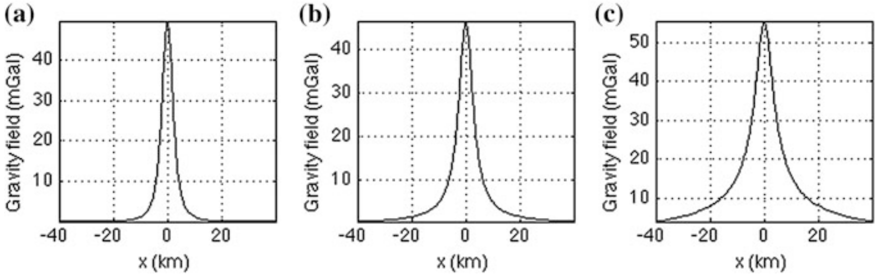

Fig. 3 The gravity anomalies due to a pole source (**a**), to a fractional order $\alpha = -0.5$ integration of a pole source (**b**) and to a bottomless vertical line mass (**c**)

5 Estimation of the Source Properties Using the Homogeneity Scaling-Law

In a previous section, we saw how estimating the source properties (Hurst or Holder exponent, depth to the source) using the scaling law related to the fractal or to the Spector and Grant's model. Similarly, we now here briefly describe methods used in applied geophysics to estimate the homogeneity degree n and the depth to the sources thanks to the homogeneity scaling-law. It may be shown (e.g., Thompson 1982) that the homogeneity relation (13) implies that homogeneous functions satisfy also the Euler differential homogeneity equation:

$$\frac{\partial f}{\partial x}(x - x_0) + \frac{\partial f}{\partial y}(y - y_0) + \frac{\partial f}{\partial z}(z - z_0) = -nf, \tag{16}$$

provided f is a differentiable function. This equation is particularly useful, since, differently than the homogeneity Eq. (13), it expresses the homogeneity properties of the fields with a differential equation or, in other words, in a local way at each point $B(x, y, z)$ in the harmonic region. As such, it has been widely utilized using a local approach, i.e. estimating the unknown source parameters within a moving window centred at any point. This approach is referred to as Euler Deconvolution (Reid et al. 1990). Note that within the window the underlying hypothesis is that the homogeneity degree is assumed not to vary within the window, i.e. it is assumed that any source body giving rise to the sampled magnetic or gravity field in the field is simple enough to be represented by one singular point e.g., point mass or dipole, line source, sheet or dyke, and thick contact.

To face the problem of the Euler differential Eq. (16) or of the homogeneity Eq. (13), different strategies have been adopted. We briefly group there some of the most used, in two categories, that of the monoscale methods and of the multiscale methods.

5.1 Monoscale Methods

For monoscale methods, we mean the technique based on solving the Euler differential homogeneity equation with data only at the single level of the measurements. The first of them, shared by many Euler deconvolution algorithms (e.g. Thompson 1982; Reid et al. 1990; Barbosa et al. 1999; Mushayandebvu et al. 2001; Stavrev and Reid 2007; Fedi et al. 2009), mainly consists in the use of Eq. (4), slightly modified to account for an unknown background effect b:

$$\frac{\partial f}{\partial x}(x - x_0) + \frac{\partial f}{\partial y}(y - y_0) + \frac{\partial f}{\partial z}(z - z_0) = -n(f + b). \tag{17}$$

As we said, Euler deconvolution algorithms are based on solving a linear system of Euler's Eqs. (17) for the unknowns x_0, y_0, z_0, n and b, for a set of observation points covered by a moving window of size W, by assuming that the following approximated equation holds:

$$f(\boldsymbol{r}) \sim F_H(\boldsymbol{r}) \quad \text{for any point in } W, \tag{18}$$

where $F_H(\boldsymbol{r})$ is the best *homogeneous field* of integer degree n approximating the field f at points in the window W. The method allows for a different kind of homogeneous field F_H at each window position, provided it is a good local approximation for f.

5.2 Multiscale Methods

Other methods deal instead with a multiscale analysis of potential fields, which are based on solving Eqs. (13, 16) with data at more altitudes. Within this category we find methods based on the CWT (e.g., Moreau et al. 1997; Sailhac and Gibert 2003; Saracco et al. 2004; Fedi et al. 2010). For potential field analysis, poissonian wavelets are typically used, making the method stable because the coefficients of the CWT are completely determined by the upward continuation of the field to the considered scales. Fedi and Cascone (2011) defined a more general approach, called Composite CWT, which let potential fields to be studied with wavelets other than poissonian, such as Morlet wavelet, Gaussian wavelets and any other. In such case, the coefficients at the different scales will be no longer related to the upward continuation, but the transformation remains very stable with any wavelet order. Other multiscale methods, such as the Depth from EXtreme Points (DEXP), SCALFUN (Florio et al. 2009) or the multiridge analysis (Fedi 2007; Fedi et al. 2009; Quarta 2009; Florio and Fedi 2014), make explicit reference to the upward continuation of any-order derivative of the field to the scales: $l = z > z_m$, where z_m is the altitude of the measurement surface.

For most multiscale methods the scale is equivalent to the altitude of continuation. A convenient tool to study the behavior of potential fields across the scales is the scaling function, defined by Fedi (2007) as:

$$\tau(z) = \frac{\partial \log T}{\partial \log z} = n\frac{z}{z - z_0}. \tag{19}$$

The scaling function is a dimensionless function of the altitude, which characterizes the scaling behavior of a homogeneous field (Fedi 2007). For homogeneous fields, the homogeneity degree n and the depth to the source z_0 may be estimated from τ in a number of ways (Fedi and Florio 2006). For instance, altitudes and depths have an arbitrary zero level, so that they may be rescaled by a guess depth value ζ:

$$\tau(z) = n\frac{z - \zeta}{z - z_0}, \tag{20}$$

and z_0 may be estimated as the value of $\zeta = z_0$ making τ the closest to a straight line with a zero slope. The homogeneity degree n may be instead estimated by the intercept of this line (see Fedi 2007, for further details).

Euler Deconvolution is a local method, i.e. it characterizes the field punctually. As such, it may not only be applied to points on the measurement plane, but also to investigate the homogeneous scaling across scales, as recently proposed by Florio et al. (2014). Among multiscale methods the DEXP theory (Fedi 2007; Fedi and Abbas 2013) involves a nice property of homogeneous functions: considering a multiscale field $f(z)$, i.e. the field at more scales (i.e., altitudes $z_1 \le z \le z_2$), and multiplying the data at each scale by $z^{-n/2}$, the DEXP transformed field

$$\Omega = fz^{n/2} \tag{21}$$

has as its extreme points (i.e. maxima and minima) occurring at the scale corresponding to the opposite of the depth to source z_0, that is at $z = -z_0$.

Besides this, the DEXP transformation also has the property of yielding an image of the source distribution (Fedi and Pilkington 2012), which may be considered as a preliminary step before more accurate inversion. Even though Ω is not given directly in source-density units, it is very easy to it multiply by a physical constant allowing such units. Recent automatic algorithms to provide an automatic DEXP transformation are given in (Abbas and Fedi 2014; Abbas et al. 2014). One of the most striking features of these methods is that they provide an independent estimate of the homogeneity degree and of the depth to the source. The imaging properties of the DEXP transformation are shown in Fig. 4, where the Bouguer gravity anomalies of the Campanian area (a) are transformed in the DEXP 3D image (b), which well describes the source distribution in the underground source volume. The maxima of the DEXP image may be used to find the depth to the source position.

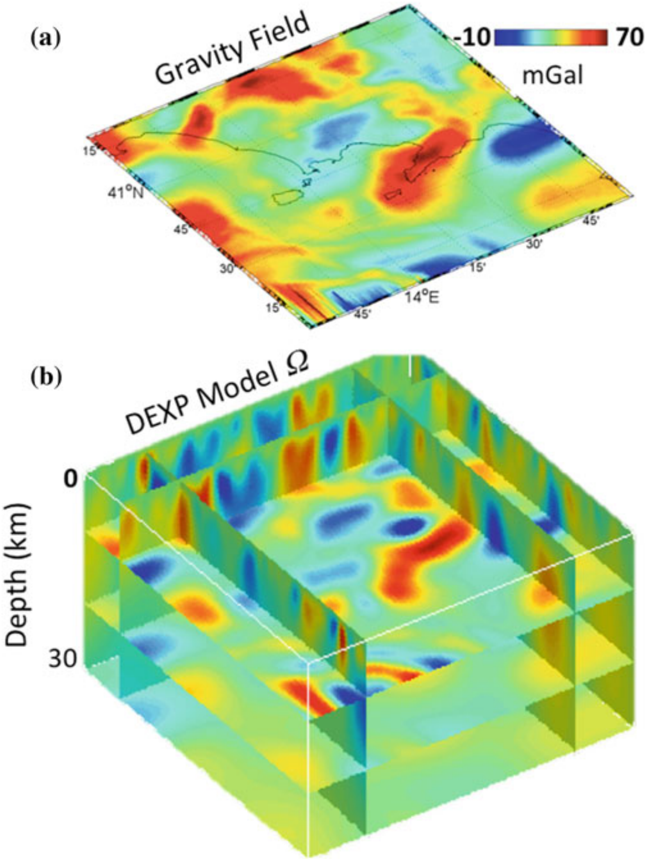

Fig. 4 The DEXP imaging. **a** Bouguer gravity anomalies of the Campanian area; **b** transformed DEXP 3D image. The source distribution in the underground source volume is well represented by the DEXP transformed image. The maxima of the DEXP image may be used to find the depth to the source position

One of the main advantages of multiscale methods is their stability: they use in fact a composite upward continuation-derivative operator (Florio et al. 2009), which is designed to attenuate the noise, including the mutual interference effects from more sources, still maintaining a reasonable signal-to-noise ratio. The analysis is then performed along selected lines L in the 3D space, called ridges, which are built by joining the extreme points of the analysed field at different scales and assuming that the following approximated equation holds:

$$f(\boldsymbol{r}) \sim F_H(\boldsymbol{r}) \quad \text{for points in a moving window } W \text{ sliding along } L \tag{22}$$

where again F_H is the best *homogeneous field* of integer degree n approximating the field in W.

6 Multifractal Random Processes Vs. Inhomogeneous Fields

Multifractal models allow managing random processes more complex than those related to a monofractal model and they so represent a useful generalization of the fractal theory. We will see now that the homogeneity scaling law can also be generalized, in order to deal with more complex source-density distributions than the one-point models.

In fact, real-world source-density distributions are generally far from being well modelled by a single one-point source and n is expected to be a non-constant function of the spatial coordinates, being dependent on both the depth and kind of source distribution. In Euler Deconvolution, the observed scattering of solutions from subsequent windows is mainly due, even if not only, to approximate the measured field data with those from one-point sources.

Steenland (1968) was probably the first to clearly illustrate that, for the most realistic cases of inhomogeneous potential fields, n is varying with the distance to the source, as shown in Fig. 5 for sources such as 3D and 2D thick prisms, thin plate 2D, thin circular disc. Note also that for such sources n not only varies but also assumes fractional values. This is completely different from one-point sources (solid lines: pole and infinite horizontal line) for which n is constant and assumes always an integer value. But this is no longer a problem, as we already said that homogeneous sources of fractional index might be defined in the framework of fractional potential fields (see Fig. 3).

So, similarly to the generalization from monofractals to multifractals (Eqs. 1 and 3), we need now to generalize the concept of homogeneous sources of integer homogeneity degree to that of multi-homogeneous sources of fractional and varying degrees.

In practice, we have to replace the homogeneity Eq. (13) by:

$$f(ax, ay, az) = a^{n(x,y,z)} f(x, y, z), \tag{23}$$

and the differential Euler homogeneity equation (Eq. 16) by:

$$\frac{\partial f}{\partial x}(x - x_0) + \frac{\partial f}{\partial y}(y - y_0) + \frac{\partial f}{\partial z}(z - z_0) = -n(r - r_0) f, \tag{24}$$

Since n is now a varying space function, f is no longer homogeneous. In affinity with multifractals we can call it multi-homogeneous or, simply, inhomogeneous. Similarly, the homogeneity degree may be called multi-homogeneity degree. Fedi et al. (2013) proposed a method to define the source parameters of such inhomogeneous fields analysing the scaling function of a multilevel dataset. They showed that the source parameters of inhomogeneous source distributions, such as the finite cylinder, might be successfully estimated owning to this new concept of generalized homogeneity. They showed that we may have access to the complex characterization

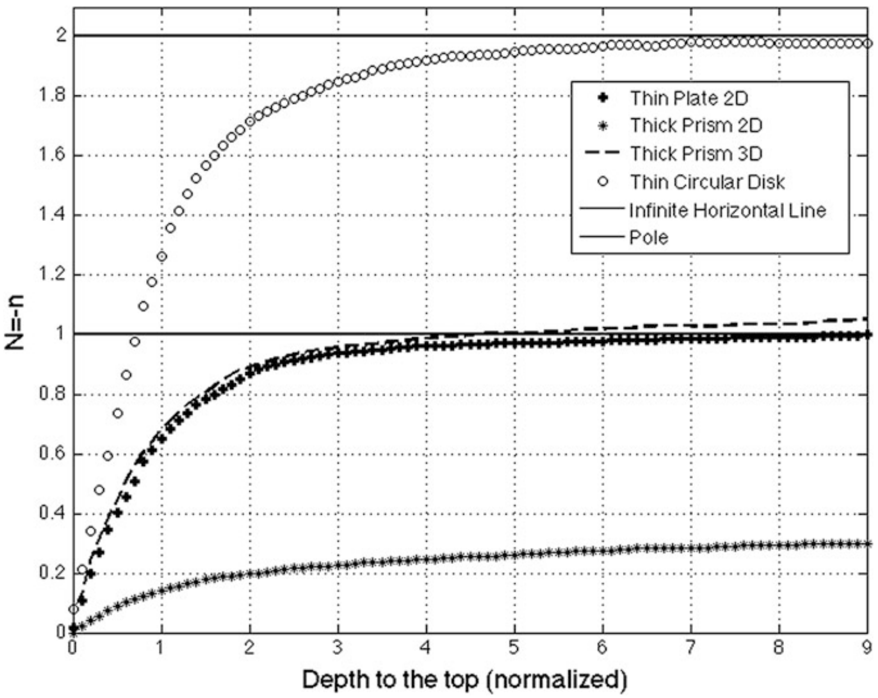

Fig. 5 The homogeneity degree of inhomogeneous fields versus altitude. For inhomogeneous sources, the homogeneity degree changes n versus the altitude and it is fractional. The curves relative to different cases are shown, namely the 3D and 2D thick prisms, the thin plate 2D, the thin circular disc. The only constant curves are related to one-point sources. The depth to the top is normalized in such a way that the half width is equal to 1 (from Steenland 1968, redrawn)

of the sources by studying the inherent scaling properties of their fields across the scales $z_1 \leq z \leq z_2$, where z_1 is the primary level of observation (or the lowest acceptable level of downward continuation) and z_2 is the upper acceptable level of upward continuation.

7 Conclusions

The key role of scaling properties in potential field theory is immediately clear if one considers the field of a complex source, such as a fractal, at different scales. On the other hand, the same may be said when observing the behavior of the fields related to another class of sources: the homogeneous-density or the uniform and homogeneous magnetization models owning to the one-point sources.

In both the cases, as it is well known in potential field theory, potential or its derivatives are convolutions between source density and specific operators and actually map the source-density distribution complexity into that of the field. For fractal source distributions, due to the convolution properties and to the form of the convolution kernel, at increasing altitudes, such field tends to lose the irregular behavior and tends to be much more close to that of a relatively homogeneous-density source distribution, so as to be better interpreted by the models based on the multi-homogeneity theory, i.e. by a behavior similar to the black lines in Fig. (1).

If we consider the asymptotic expansion of the potential field (e.g. Tikhonov and Samarski 2013), multipolar terms will change their role as the scale changes, obviously implying that the field scaling characterization will change accordingly: close to the source the scale invariance typical of the fractal source distribution will be observed, while far from the sources the multipole terms other than pole are very low and the potential will show the scale invariance typical of one-point spherical sources: $n = -2$ for the gravity field of a homogeneous-density sphere and $n = -3$ for the magnetic field of a homogeneous and uniformly magnetized sphere.

We also described a fourth class of source distributions, that is of sources whose complexity is such that we cannot describe it either as that of random source models (monofractals and multifractals) or as that of one-point functions. These fields are inhomogeneous, meaning that the homogeneity degree varies with the scale, and are very common in real world. Some examples are the source distributions due to complex but not yet random source distributions, as the field of a polyhedral or that of any irregular geometry. For these sources, scale invariance could be approximately assessed by methods such as Euler Deconvolution, but only within a very restricted range of scales. One may however find true evidence for scaling in the asymptotic regions, i.e. within only the very large or the very small scales.

Our main conclusion is that new methods are requested for handling with inhomogeneous fields, being the classical homogeneity law (Eq. 13) not applicable, unless than in an approximate way. In fact, similar to what happens for random source models, where the fractal scaling-law (Eq. 1) has been generalized into a multifractal law (Eq. 3), the homogeneity law must be replaced by a multi-homogeneity law (Eq. 23). Along this line, one method was recently proposed by Fedi et al. 2013; Fedi et al. 2015, proving to be successful when the interpretation of a multiscale dataset is developed in the framework of homogeneous field models of fractional-degree.

References

Abbas MA, Fedi M (2014) Automatic DEXP imaging of potential fields independent of the structural index. Geophys J Int 199:1625–1632. doi:10.1093/gji/ggu354

Abbas MA, Fedi M, Florio G (2014) Improving the local wavenumber method by automatic DEXP transformation. J Appl Geophys 111:250–255. doi:10.1016/j.jappgeo.2014.10.004

Arnéodo A, Decoster N, Roux S (2000) A wavelet-based method for multifractal image analysis. I. Methodology and test applications on isotropic and anisotropic random rough surfaces. Eur Phys J B Condens Matter Complex Syst 15(3):567–600

Bansal AR, Gabriel G, Dimri VP (2010) Power law distribution of susceptibility and density and its relation to seismic properties: an example from the German Continental Deep Drilling Program (KTB). J Appl Geophys 72:123–128

Bansal AR, Gabriel G, Dimri VP, Krawczyk CM (2011) Estimation of the depth to the bottom of magnetic sources by a modified centroid method for fractal distribution of sources: an application to aeromagnetic data in Germany, Geophysics (3):L11–L22

Barbosa VCF, Silva JBC, Medeiros WE (1999) Stability analysis and improvement of structural index estimation in Euler deconvolution. Geophysics 64(1):48–60

Bouligand C, Glen JMG, Blakely RJ (2009) Mapping Curie temperature depth in the western United States with a fractal model for crustal magnetization. J Geophys Res 114:B11104. doi:10.1029/2009JB006494

Caratori Tontini F, Cocchi L, Carmisciano C (2009) Rapid 3-D forward model of potential fields with application to the Palinuro Seamount magnetic anomaly (southern Tyrrhenian Sea, Italy). J Geophys Res 114(B02103):2008J. doi:10.1029/B005907

Fedi M. (2003) Global and local multiscale analysis of magnetic susceptibility data. Pure Appl Geophys 160(12):2399–2417

Fedi M (2007) DEXP: a fast method to determine the depth and the structural index of potential fields sources. Geophysics 72:I1–I11

Fedi M, Abbas MA (2013) A fast interpretation of self-potential data using the depth from extreme points method. Geophysics 78:107–116. doi:10.1190/geo2012-0074.1

Fedi M, Cascone L (2011) Composite continuous wavelet transform of potential fields with different choices of analyzing wavelets. J Geophys Res 116(B7). doi:10.1029/2010JB007882

Fedi M, Florio G (2006) SCALFUN: 3D analysis of potential field scaling function to determine independently or simultaneously structural index and depth to source. In: 76° SEG annual meeting, New Orleans, 1–6 Oct 2006, pp 963–967

Fedi M, Pilkington M (2012) Understanding imaging methods for potential field data. Geophysics 77:1–12. doi:10.1190/GEO2011-0078.1

Fedi M, Fiore D, La Manna M (2005) Chapter 4. Regularity analysis applied to well log data. In: Dimri VP (ed) Fractal behaviour of the earth system. ISBN: 3-540-26532-5

Fedi M, Florio G, Quarta T (2009) Multiridge analysis of potential fields: geometrical method and reduced Euler deconvolution. Geophysics 74(4):L53–L65

Fedi M, Cella F, Quarta T, Villani A (2010) 2D continuous wavelet transform of potential fields due to extended source distributions. Appl Comput Harmonic Anal 28(3):320–337

Fedi M, Florio G, Paoletti V (2012) Local homogeneity of potential fields and fractional homogeneous functions: a new theory for improved source parameter estimation. In: 82nd annual meeting of the society of exploration geophysicists, Society of Exploration Geophysicists, Las Vegas (USA), 4–9 Nov 2012, pp 1–5. doi:10.1190/segam2012-1169.1

Fedi M, Florio G, Paoletti V (2015) MHODE: a local-homogeneity theory for improved source-parameter estimation of potential fields. Geophys J Int 202(2):887–900. http://doi.org/10.1093/gji/ggv185

Fedi M, Quarta T, De Santis A (1997) Inherent power-law behavior of magnetic field power spectra from a Spector and Grant ensemble. Geophysics 62(4):1143–1150

Florio G, Fedi M (2014) Multiridge Euler deconvolution. Geophys Prospect 62(2):333–351. doi:10.1111/1365-2478.12078

Florio G, Fedi M, Rapolla A (2009) Interpretation of regional aeromagnetic data by the scaling function method: the case of Southern Apennines (Italy). Geophys Prospect 57:479–489

Gneiting T, Schlather M (2004) Stochastic models that separate fractal dimension and the Hurst effect. SIAM Rev 46:269–282

Gregotski ME, Jensen O, Arkani-Hamed J (1991) Fractal stochastic modelling of aeromagnetic data. Geophysics 56:1706–1715

Hermann FJ (1997) A scaling medium representation, a discussion on well-logs, fractals and wave. PhD thesis, Faculty of Applied Physics, Delft University of Thecnology, Delft, The Netherlands (RUSS)

Mandelbrot Benoît B (1983) The fractal geometry of nature. W.H. Freeman, San Francisco. ISBN 0-7167-1186-9

Marsan D, Bewan CJ (1999) Multiscaling nature of sonic velocities and lithology in the upper crystalline crust: evidence from the main KTB borehole. Geophys Res Lett 26(2):275–278

Maus S, Dimri VP (1994) Scaling properties of potential fields due to scaling sources. Geophys Res Lett 21:891–894

Moreau F, Gibert D, Holschneider M, Saracco G (1997) Wavelet analysis of potential fields. Inverse Prob 13:165

Muniandy SV, Kan CS, Lim SC, Radiman S (2003) Fractal analysis of lyotropic lamellar liquid crystal textures. Phys A Stat Mech and its Appl 323:107–123

Mushayandebvu MF, van Driel P, Reid AB, Fairhead JD (2001) Magnetic source parameters of two-dimensional structures using extended Euler deconvolution. Geophysics 66:814–823

Naidu P (1968) Spectrum of the potential field due to randomly distributed sources. Geophysics 33:337–345

Pilkington M, Todoeschuck JP (1993) Fractal magnetization of continental crust. Geophys Res Lett 20:627–630

Quarta TAM (2009) Euler homogeneity equation along ridges for a rapid estimation of potential field source properties. Geophys Prospect 57:527–542

Quarta T, Fedi M, De Santis A (2000) Source ambiguity from estimation of the scaling exponent of potential field power spectra. Geophys J Int 140:311–323

Ravat D, Pignatelli A, Nicolosi I, Chiappini M (2007) A study of spectral methods of estimating the depth to the bottom of magnetic sources from near-surface magnetic anomaly data. Geophys J Int 169:421–434

Reid AB, Allsop JM, Granser H, Millett AJ, Somerton IW (1990) Magnetic interpretation in three dimensions using Euler deconvolution. Geophysics 55:80–91

Russ J (1994) Fractal surfaces. Plenum Press, New York. 309

Sailhac P, Gibert D (2003) Identification of sources of potential fields with the continuous wavelet transform: Two-dimensional wavelets and multipolar approximations. J Geophys Res 108 (B5):2262

Saracco G, Labazuy P, Moreau F (2004) Localization of self-potential sources in volcano-electric effect with complex continuous wavelet transform and electrical tomography methods for an active volcano. Geophys Res Lett 31:1–5

Spector A, Grant FS (1970) Statistical models for interpreting aeromagnetic data. Geophysics 35:293–302

Stavrev P, Reid AB (2007) Degrees of homogeneity of potential fields and structural indices of Euler deconvolution. Geophysics 72(1):L1–L2

Steenland NC (1968) Discussion on 'The geomagnetic gradiometer' by H. A. Slack, V. M. Lynch and L. Langan (Geophysics, October l967, 877–892). Geophysics, 33:681–684

Thompson D (1982) EULDPH: a new technique for making computer-assisted depth estimates from magnetic data. Geophysics 47:31

Tikhonov AN, Samarskii AA (2013) Equations of mathematical physics. Dover, New York, p 760

Turcotte DL (2011) Fractals and Chaos in geology and geophysics. Cambridge University Press, Cambridge, pp 1–414

Curie Depth Estimation from Aeromagnetic for Fractal Distribution of Sources

A.R. Bansal, V.P. Dimri, Raj Kumar and S.P. Anand

Abstract The earth's magnetic field is used to find the depth of anomalous sources as shallow as few metres to tens of kilometres. The deepest depths found from the magnetic field sometimes correspond to Curie depth, a depth in the crust where magnetic minerals lose their magnetic field due to increase in temperature. Estimation of depth from magnetic/aeromagnetic data generally assumes random and uncorrelated distribution of magnetic sources equivalent to white noise distribution. The white noise distribution is assumed because of mathematical simplicity and non-availability of information about source distribution, whereas from many borehole studies it is found that magnetic sources follow random and fractal distribution. The fractal distribution of sources found many applications in depth estimation from magnetic/aeromagnetic data. In this chapter Curie depth estimation from aeromagnetic data for fractal distribution of sources will be presented.

1 Introduction

Curie depth is a depth in the earth's crust where ferromagnetic mineral changes to paramagnetic due to increase in temperature and generally no detectable magnetic field is observed below this depth in the crust. This depth may be very deep or

---

A.R. Bansal (✉) · V.P. Dimri · R. Kumar
CSIR-National Geophysical Research Institute, Uppal Road,
Hyderabad 500007, India
e-mail: abhey_bansal@ngri.res.in

V.P. Dimri
e-mail: vpdimri@gmail.com

R. Kumar
e-mail: raj.kumar8709@gmail.com

S.P. Anand
Indian Institute of Geomagnetism, Kalamboli Highway, New Panvel(W),
Navi Mumbai 410218, India
e-mail: anand@iigs.iigm.res.in

V.P. Dimri (ed.), *Fractal Solutions for Understanding Complex Systems in Earth Sciences*, Springer Earth System Sciences,
DOI 10.1007/978-3-319-24675-8_2

shallow depending on heat flow in the region and composition of rocks. The Curie depth in a region serves as a proxy for heat flow. Direct measurement of heat flow is carried out from bore holes in land and drilling cores from the ocean. The direct measurement of heat flow is very sparse because of higher costs for drilling, whereas proxy estimation from aeromagnetic/magnetic data provides homogeneous coverage. The magnetic surveys are easy to carry out and cheap in terms of cost involved in field surveys.

The estimation of depth from magnetic data is an ambiguous process and there are many methods for its estimation. None of the methods provide reliable depth estimations. These methods are applied in space and frequency domain. The frequency domain methods are generally preferred as compared to the space domain (Gundmundsson 1966, 1967; Heirtzler and Le Pichon 1965; Neidell 1966; Naidu 1968, 1970; Bhattacharyya 1967; Spector and Grant 1970; Treitel et al. 1971; Negi et al. 1986; Dimri 1992) because convolution operator changes to multiplication. The Fourier domain methods became very popular in depth estimation because of simplicity. The classical methods of depth estimation assume random and uncorrelated distribution of sources which is equivalent to white noise distribution.

From many boreholes it is found that source distribution follows random and fractal distribution of sources which is known as scaling distribution (Pilkington and Todoeschuck 1990, 1993, 2004; Pilkington et al. 1994; Maus and Dimri 1995a, b; Leonardi and Kumpel 1998; Bansal et al. 2010; Bansal and Dimri 2010). The power spectrum of scaling distribution is frequency dependent in contrast of white noise which is frequency independent and mathematically it is defined as:

$$P(k) = Ak^{-\beta} \tag{1}$$

where P is the—power spectrum, k is the wavenumber, β is the scaling factor and A is constant. The values of scaling exponents represent degree of correlation and larger the value stronger is long range correlation.

The values of scaling exponents due to source and field are related and estimated easily if one is known and vice versa (Maus and Dimri 1994). A known value of scaling exponents can be easily represented in different dimensions using simple formula (Maus and Dimri 1994). The β values are found to vary with space (Pilkington and Todoeschuck 1993; Bansal et al. 2010; Bansal and Dimri 2014) but still the exact relation with tectonic and rock formations is not yet established mainly due to limited studies. The use of scaling distribution of sources provides better depth estimation (Pilkington and Todoeschuck 1993; Maus and Dimri 1994, 1996; Fedi et al. 1997; Bansal and Dimri 1999, 2001; Bansal et al. 2006a, b; Dimri 2000; Dimri et al. 2003). The values of scaling exponents can be converted to fractal dimension using a simple formula (Mandelbrot 1982; Turcottee 1997; Bansal and Dimri 2005a). Fedi et al. (1997) have shown inherent power law due to Spector and Grant ensemble.

Curie depth estimations are carried out worldwide from aeromagnetic data using Fourier domain methods mostly assuming random and uncorrelated distribution of sources (Okobu et al. 1985; Tanaka et al. 1999; Chiozzi et al. 2005; Trifonova et al. 2009). Few recent studies have claimed better depth estimation for fractal distribution of sources (Maus et al. 1997; Bouligand et al. 2009; Bansal et al. 2011; Salem et al. 2014).

2 Conventional Centroid Depth Method

In centroid method (Bhattacharyya and Leu 1975; Okobu et al. 1985; Tanaka et al. 1999) Curie depth is estimated in two steps: (1) top depth of anomalous body and (2) centroid depths are computed from the power spectrum of magnetic field data and then these depth values are converted to Curie depths. Spector and Grant (1970) proposed a method to estimate top depth of assemblage of magnetic sources. In this method, power spectrum of total magnetic field is represented in terms of top depth and thickness of magnetic body (Blakely 1995):

$$P\left(k_x, k_y\right) = 4\pi^2 C_m^2 \varphi_{\mathrm{m}}\left(k_x, k_y\right) |\Theta_{\mathrm{m}}|^2 |\Theta_{\mathrm{f}}|^2 \mathrm{e}^{-2|k|z_{\mathrm{t}}} \times \left(1 - \mathrm{e}^{-|k|(z_{\mathrm{b}} - z_{\mathrm{t}})}\right)^2 \tag{2}$$

where k_x and k_y are the wavenumbers in the x- and y-directions; C_m is a constant of proportionality; φ_{m} is the power spectrum of the magnetization; Θ_{m} and Θ_{f} are the directional factors related to the magnetization and geomagnetic field, respectively; Z_{t} and Z_{b} are the top and bottom depths of the magnetic sources.

It is common practice in geophysics for converting 2-D power spectrum to 1-D by taking radial average. In this case terms Θ_{m} and Θ_{f} become constant and φ_{m} is constant for random and uncorrelated distribution of sources. In case of radial averaging of power spectrum, and random and uncorrelated distribution of sources, Eq. 2 can be written as:

$$P(k) = A_1 \mathrm{e}^{-2|k|z_{\mathrm{t}}} \left(1 - \mathrm{e}^{-|k|(z_{\mathrm{b}} - z_{\mathrm{t}})}\right)^2 \tag{3}$$

where A_1 is a constant and for very thick magnetic body the right-hand side of Eq. 3 contains only top depth and Eq. 3 reduces as:

$$P(k) = A_1 \mathrm{e}^{-2|k|z_{\mathrm{t}}} \tag{4}$$

Equation (4) is frequently used for finding the top depth of anomalous magnetic bodies.

The centroid depth of magnetic body is given as (Bhattacharyya and Leu 1975, 1977; Okobo et al. 1985; Tanaka et al. 1999):

$$\ln\left(\frac{P(k)^{\frac{1}{2}}}{k}\right) = A_2 - |k|Z_0 \tag{5}$$

The Curie depth is finally computed from centroid and top depth as:

$$Z_b = 2Z_0 - Z_t \tag{6}$$

The centroid method has become very popular for estimating Curie depth from aeromagnetic data and is applied to aeromagnetic data of many parts of world (Bhattacharyya and Leu 1975; Okubo et al. 1985; Tanaka et al. 1999; Okubo and Matsunaga 1994; Chiozzi et al. 2005; Dolmaz et al. 2005; Trifonova et al. 2009 etc.).

3 Fractal Based Methods of Curie Depth Estimation

Fourier domain methods became very popular in Curie depth estimation from aeromagnetic data because of their simplicity. However, these methods provide overestimation of depth values due to the assumption of random and uncorrelated distribution of sources (Pilkington and Todoechuck 1993; Maus and Dimri 1994, 1996; Fedi et al. 1997; Bansal and Dimri 1999, 2001, 2005b, 2014). These methods are modified for scaling distribution of sources. The scaling distribution of sources is equivalent to fractal distribution of sources and these modified methods are called fractal based methods of depth estimation.

Maus et al. (1997) proposed a method for estimating Curie depth for fractal distribution of sources where scaling exponents, top depth and thickness of magnetic body are estimated simultaneously from power spectrum of magnetic field. Radial average of power spectrum is expressed in terms of scaling exponent and depth component as (Maus et al. 1997):

$$P(k) = C - 2kz_t - tk - \beta\ln(k) + \ln\left[\int_0^\infty [\cos h(tk) - \cos(tw)]\left(1 + \frac{w^2}{k^2}\right)^{-1-\beta/2} \mathrm{d}w\right]. \tag{7}$$

where k is the wavenumber, z_t is the top depth, t is the thickness of slab and β is the scaling exponent due to source distribution, w is the wavenumber in vertical plane. Maus et al. (1997) found a value of β equal to 4 from aeromagnetic data of South Africa and Central Asia and Curie depths vary from 15 to 20 km. Bouligand et al. (2009) derived an analytical solution for solving Eq. 7 and found difficulty in simultaneous estimation of top depth and scaling exponents. Therefore, Bouligand et al. (2009) fixed the value of scaling exponents for estimating top depth based on the shape of power spectrum of aeromagnetic data. Manual checking of estimated parameter is essential for a reliable estimation. Bansal et al. (2011) proposed a modified centroid method for the estimation of Curie depth from aeromagnetic data for scaling distribution of sources. This method computes Curie depth in two steps similar to classical centroid method for scaling distribution of sources. The top and centroid depths are computed by correcting power spectrum for scaling distribution of sources as:

Top depth:

$$\ln\left(k^{\beta}P(k)\right) = A_2 - 2kz_{\mathrm{t}} \tag{8}$$

and Centroid depth:

$$\ln\left(k^{\beta}\frac{P(k)}{k^2}\right) = A_3 - 2kz_0 \tag{9}$$

Bansal et al. (2011) also pointed out the difficulty in estimating scaling exponent and depth values simultaneous from inversion method and they fixed the value of scaling exponent equal to 1 corresponds to 1/f noises found from seismic velocity fluctuations and fault structures (Holliger 1996). Salem et al. (2014) also corrected their power spectrum before computing the top depth from the power spectrum of aeromagnetic data and applied to the magnetic data of central Red Sea. Their values of scaling exponent vary between 0 and 1.7 with an average value of 0.85 very close to 1 used by Bansal et al. (2011) in the estimation of Curie depth. The Curie depths estimated by classical and modified centroid method for fractal dimension sometimes have a large difference (Table 1). This method is successfully applied to the German, Indian and Nigerian aeromagnetic data (Bansal et al. 2011, 2013; Nwankwo 2015).

Table 1 Comparison of depth values computed using fractal (scaling) and non-fractal (conventional) distribution of sources

Block no.	Estimated Curie depths		% Higher
	Scaling	Conventional	
2	33	47	30
3	28	42	33
21	35	51	31
31	37	63	41

The difference in the computed values may be more than 40 % in some of cases (Table 1). The difference in computed values also depends on values of scaling exponents used. Higher the value of scaling exponent used larger is difference in computed values

4 Case Study: Application of Modified Centroid Method for Fractal Distribution of Sources to Central India

Bansal et al. (2013) carried out a detailed study of the Curie depth estimation in central India. The central India is tectonically complex and covers many geological entities, e.g. Deccan volcanic province, central Indian Tectonic zone, Godavari and Mahanadi intracratonic failed rifts, Chhattisgarh basin and the Proterozoic Eastern Ghat Mobile Belt.

Aeromagnetic data over central India is compiled by the Indian Institute of Geomagnetism over a common elevation of 1.5 km (Rajaram and Anand 2003; Rajaram et al. 2009). We selected four blocks of dimension 200 km × 200 km covering Eastern Dharwar, Godavari-Graben and Baster Craton. Centres of selected blocks are lying in Godavari-Graben (Blocks 2, 21) and Baster Craton (Blocks 3 and 31), whereas a large size of block covers surrounding geological entities. The Curie depths are computed using conventional (Figs. 1 and 2) and centroid method

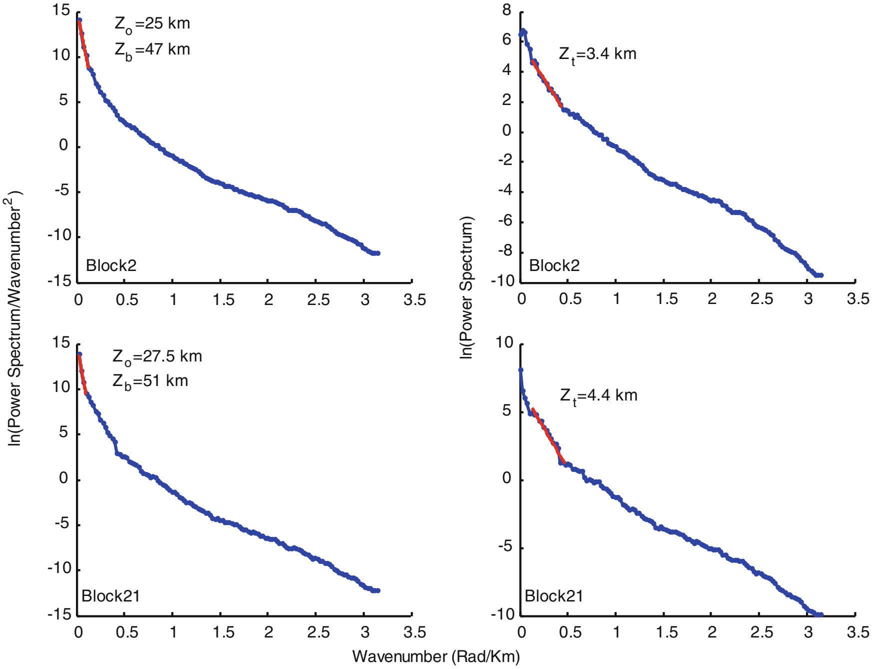

Fig. 1 Estimation of Curie depth for central India using conventional centroid method for block 2 and 21. The *left* and *right* panels indicate the estimation of centroid and top depth, respectively

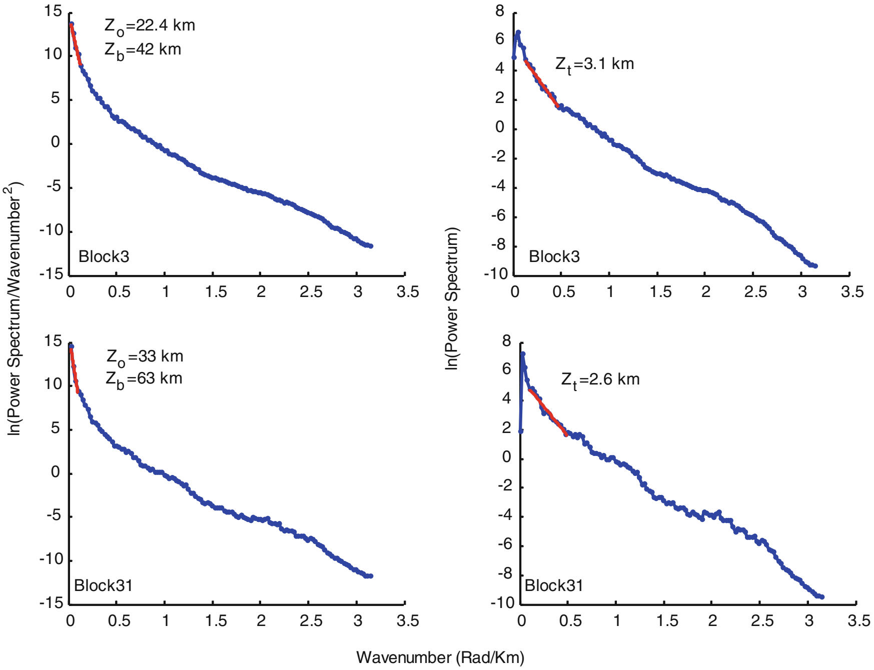

Fig. 2 Estimation of Curie depth for central India using conventional centroid method for block 3 and 31. The *left* and *right* panels indicate estimation of centroid and top depth, respectively

for fractal distribution of sources (Figs. 3 and 4). Godavari-Graben is a passive rift orthogonal to the east cost of India and the Curie depth is found to vary between 33 and 35 km (Fig. 3). Deep seismic study has shown Moho depth of 37 and 42 km in the Eastern Dharwar Craton (Reddy et al. 2005) and Godavari-Grabens (Kaila et al. 1990). Godavari-Graben region is found to have underplating of high density rocks (Behera et al. 2004; Rao 2002) and evolved during permo-carboniferous rifting. The region has undergone a number of volcanism in the past and these thermal episodes have a large effect on the Curie depth in Godavari-Graben. The centres of Blocks 3 and 31 are on the south part of Baster Craton and magnetic data also covers Godavari-Graben and Eastern Ghat mobile belts. The Baster Craton is bounded by Godavari-Graben in the west and Eastern Ghat mobile belt in the east. The Baster Craton contains vast traces of granites and gneisses with basement of

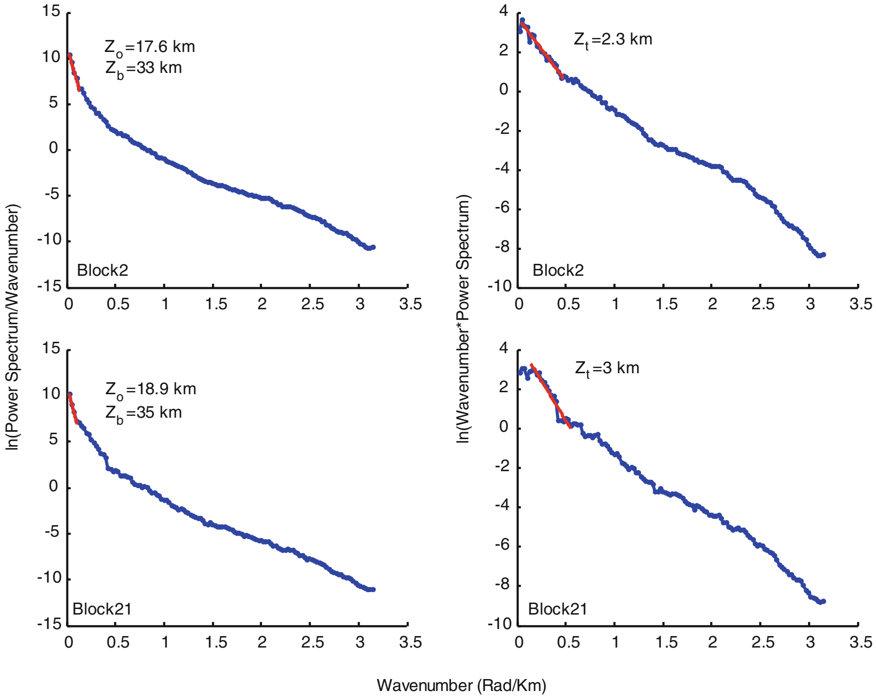

Fig. 3 Estimation of Curie depth for central India using modified centroid method for fractal distribution of sources for block 2 and 21. The *left* and *right* panels indicate estimation of centroid and top depth, respectively

mainly Archean to mid-proterozoic. The Moho depth in the North of Baster Craton is found as 48 km from deep seismic studies (Mandal et al. 2013). In the south of Baster Craton, values of Curie depth are found to vary from 28 to 37 km (Fig. 4). The region of the lowest Curie depth includes Godavari-Graben and Eastern Ghat mobile belt. The south-west part of Eastern Ghat mobile belt is found to have lower values of Curie depth 26–27 km from an earlier study (Bansal et al. 2013). The Curie depths estimated in central India using fractal distribution of sources are found to be lower than the values computed using conventional method (Fig. 5, Table 1) and reasonably well while considering other tectonic and geophysical constraints.

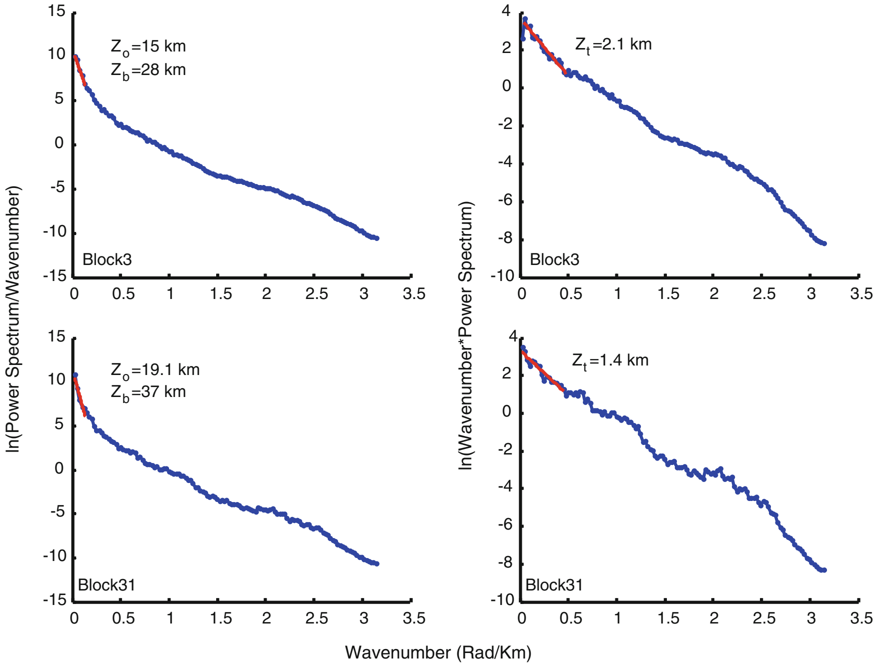

Fig. 4 Estimation of Curie depth for central India using modified centroid method for fractal distribution of sources for block 3 and 31. The *left* and *right* panels indicate estimation of centroid and top depth, respectively

5 Discussion and Conclusion

Depth estimation from magnetic data is ambiguous due to Green's equivalent layer problem. The information about source distribution is limited mainly due to limited information below the surface of earth from deep boreholes. Assumption of random and uncorrelated distribution of sources resulted in a simple relation between power spectrum and depth of magnetic sources. This method is commonly used for finding Curie depth from aeromagnetic data. The magnetic susceptibility distribution is found to follow random and fractal distribution. The fractal distribution of sources is incorporated in estimating depth from magnetic data. Many authors have claimed that methods based on fractal distribution of sources provide better depth estimation as compared to depth estimation based on white noise distribution (Maus et al. 1997; Bouligand et al. 2009; Bansal et al. 2011). Fractal based approach suffers the limitation of simultaneous estimation of depth and scaling exponents. At present, prior fixation of one of the parameters provides a better estimation of the other

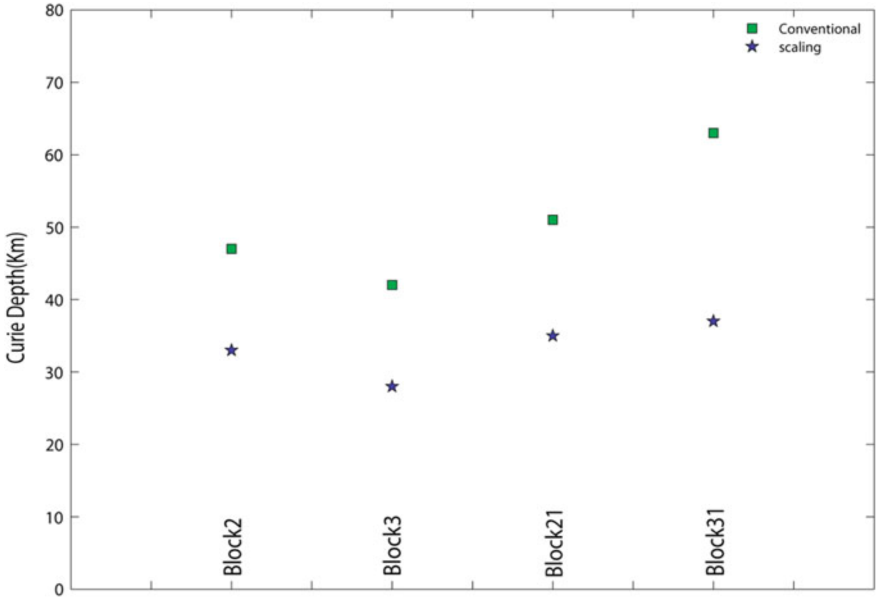

Fig. 5 The comparison of depth values estimated using conventional and modified centroid method

parameter. There is no doubt about better depth estimations using fractal distribution of sources and many researchers are working on simultaneous estimation of scaling exponent and depth values.

Acknowledgements We are thankful to CSIR-NGRI for granting permission to publish this paper. Raj Kumar is grateful to CSIR, New Delhi for the award of CSIR-JRF. ARB is also supported by research grant "SHORE" funded by CSIR, New Delhi. VPD is thankful to INSA for supporting this study.

References

Bansal AR, Dimri VP (2014) Modeling of magnetic data for scaling geology. Geophys Prospect 62:385–396

Bansal AR, Dimri VP (2001) Depth estimation from the scaling power spectral density of nonstationary gravity profile. Pure appl Geophys 158(4):799–812

Bansal AR, Dimri VP (2005a) Self-affine covariance gravity model for the Bay of Bengal. Geophysical J Int 161:21–30

Bansal AR, Dimri VP (2005b) Depth determination from nonstationary magnetic profile for scaling geology. Geophys Prospect 53(3):399–410

Bansal AR, Dimri VP (2010) Scaling spectral analysis: a new tool for interpretation of gravity and magnetic data. Earth Sci India e-J 3(1):54–68

Bansal AR, Dimri VP (1999) Gravity evidence for mid crustal domal structure below Delhi fold belt and Bhilwara super group of western India. Geophys Res Lett 26(18):2793–2795

Bansal AR, Dimri VP, Sagar GV (2006a) Quantitative interpretation of gravity and magnetic data over southern granulite terrain using scaling spectral approach. J Geol Soc India 67:469–474

Bansal AR, Dimri VP, Sagar GV (2006b) Depth estimation from gravity data using the maximum entropy method (MEM) and multi taper method (MTM). Pure Appl Geophys 163:1417–1434

Bansal AR, Gabriel G, Dimri VP (2010) Power law distribution of susceptibility and density and its relation to seismic properties: an example from the German Continental Deep Drilling Program. J Appl Geophys 72(2):123–128

Bansal AR, Gabriel G, Dimri VP, Krawczyk CM (2011) Estimation of the depth to the bottom of magnetic sources by a modified centroid method for fractal distribution of sources: an application to aeromagnetic data in Germany. Geophysics 76(3):L11–L22

Bansal AR, Anand SP, Rajaram Mita, Rao VK, Dimri VP (2013) Depth to the bottom of magnetic sources (DBMS) from aeromagnetic data of central India using modified centroid method for fractal distribution of sources. Tectonophysics 603:155–161

Behera L, Sain K, Reddy PR (2004) Evidence of underplating from seismic and gravity studies in the Mahanadi delta of eastern India and its tectonic significance. J Geophys Res 109:B12311

Bhattacharyya BK (1967) Some general properties of potential fields in space and frequency domain: a review. Geoexploration 5:127–143

Bhattacharyya BK, Leu LK (1977) Spectral analysis of gravity and magnetic anomalies due to rectangular prismatic bodies. Geophysics 42:41–50

Bhattacharyya BK, Leu LK (1975) Analysis of magnetic anomalies over Yellowstone National Park: mapping of Curie point isothermal surface for geothermal reconnaissance. J Geophys Res 80(32):4461–4465

Blakely RJ (1995) Potential theory in gravity and magnetic applications. Cambridge University Press, Cambridge

Bouligand C, Glen JMG, Blakely RJ (2009) Mapping Curie temperature depth in the western United States with a fractal model for crustal magnetization. J Geophys Res 114:B11104

Chiozzi P, Matsushima J, Okubo Y, Pasquale V, Verdoya M (2005) Curie-point depth from spectral analysis of magnetic data in Central-Southern Europe. Phys Earth Planet Inter 152 (4):267–276

Dimri VP (2000) Crustal fractal magnetization. In: Dimri VP (ed) Application of fractals in earth sciences. A. A. Balkema, Oxford, Oxford & IBH Publishing Co., New Delhi, pp 89–95

Dimri VP, Bansal AR, Srivastava RP, Vedanti N (2003) Scaling behaviour of real earth source distribution: Indian case studies. In: Mahadevan TM, Arora BR, Gupta KR (eds) Indian continental lithosphere: emerging research trends: Geological Society of India Memoir vol 53, pp 431–448

Dimri VP (1992) Deconvolution and inverse theory: application to geophysical problems. Elsevier Science Publishers, Amsterdam, p 230

Dolmaz MN, Ustao¨mer T, Hisarli ZM, Orbay N (2005) Curie point depth variations to infer thermal structure of the crust at the African-Eurasian convergence zone SW Turkey. Earth Planet Space 57:373–383

Fedi M, Quarta T, Santis AD (1997) Inherent power-law behavior of magnetic field power spectra from a Spector and Grant ensemble. Geophysics 62:1143–1150

Gundmundsson G (1966) Interpretation of one-dimensional magnetic anomalies by use of the Fourier-transform. Geophys J R Astr Soc 12:87–97

Gundmundsson G (1967) Spectral analysis of magnetic surveys. Geophys J R Astr Soc 13:325–337

Heirtzler JR, Le Pichon X (1965) Crustal structure of the mid-ocean ridges 3, magnetic anomalies over the mid-Atlantic Ridge. J Geophys Res 70(16):4013–4033

Holliger K (1996) Fault scaling and 1/f noise scaling of seismic velocity fluctuations in the upper crystalline crust. Geology 24(12):1103–1106

Kaila KL, Murthy PRK, Rao VK, Venkateswarlu N (1990) Deep seismic sounding in the Godavari Graben and Godavari (coastal) Basin India. Tectonophysics 173:307–317

Leonardi S, Kumpel HJ (1998) Variability of geophysical log data and the signature of crustal heterogeneities at the KTB. Geophys J Int 135:964–974

Mandal B, Sen MK, Vijaya Rao V (2013) New seismic images of the Central Indian Sututre Zone and their tectonic implications. Tectonics 32:908–921

Mandelbrot BB (1982) The fractal geometry of nature. Freeman, San Francisco

Maus S, Dimri VP (1994) Scaling properties of potential fields due to scaling sources. Geophys Res Lett 21(10):891–894

Maus S, Dimri VP (1995) Potential field power spectrum inversion for scaling geology. J Geophys Res 100(B7):12605–12616

Maua S, Dimri VP (1995) Basin depth estimation using scaling properties of potential fields. J Assoc Expl Geophys 16(3):131–139

Maus S, Dimri VP (1996) Depth estimation from the scaling power spectrum of potential fields. Geophys J Int 124:113–120

Maus S, Gordon D, Fairhead JD (1997) Curie temperature depth estimation using a self-similar magnetization model. Geophys J Int 129(1):163–168

Naidu PS (1968) Spectrum of the potential field due to randomly distributed source. Geophysics 33:337–345

Naidu PS (1970) Statistical structure of aeromagnetic field. Geophysics 35(2):279–292

Neidell NS (1966) Spectral studies of marine geophysical profiles. Geophysics 31(1):122–134

Negi JG, Dimri VP, Agarwal PK, Pandey OP (1986) A spectral analysis of the aeromagnetic profiles for thickness estimation of flood basalts of India. Explo Geophys 17:105–111

Nwankwo LI (2015) Estimation of depths to the bottom of magnetic sources and ensuing geothermal parameters from aeromagnetic data of Upper Sokoto Basin Nigeria. Geothermics 54:76–81

Okubo Y, Matsunaga T (1994) Curie point depth in northeast Japan and its correlation with regional thermal structure and seismicity. J Geophys Res 99(B11):22363–22371

Okubo Y, Graf RJ, Hansen RO, Ogawa K, Tsu H (1985) Curie point depths of the island of Kyushu and surrounding area Japan. Geophysics 50(3):481–489

Pilkington M, Todoeschuck JP (1993) Fractal magnetization of continental crust. Geophys Res Lett 20:627–630

Pilkington M, Todoeschuck JP (2004) Power-law scaling behavior of crustal density and gravity. Geophys Res Lett 31(9):L09606

Pilkington M, Todoeschuck JP (1990) Stochastic inversion for scaling geology. Geophys J Int 102 (1):205–217

Pilkington M, Gregotski ME, Todoeschuck JP (1994) Using fractal crustal magnetization models in magnetic interpretation. Geophys Prospect 42(6):677–692

Reddy PR (2005) Crustal velocity structure of western India and its use in understanding intraplate seismicity. Curr Sci 88(10):1652–1657

Rajaram M, Anand SP (2003) Central Indian tectonics revisited using aeromagnetic data. Earth Planets Space 55:e1–e4

Rajaram M, Anand SP, Hemant K, Purucker ME (2009) Curie isotherm map of Indian subcontinent from satellite and aeromagnetic data. Earth Planetary Sci Lett 282 (3–4):147–158

Rao VK (2002) Crustal structure and evolution of Godavari Graben (Chintalpudi sub-basin) and Krishna–Godavari Basin—an integrated approach. Ph.D. thesis, Osmania University, Hyderabad, India

Salem A, Green C, Ravat D, Singh KH, East P, Fairhead JD, Mogren S, Biegert Ed (2014) Depth to Curie temperature across the central Red Sea from magnetic data using the de-fractal method. Techtonophysics 624–625:75–86

Spector A, Grant FS (1970) Statistical model for interpreting aeromagnetic data. Geophysics 35 (2):293–302

Tanaka A, Okubo Y, Matsubayashi O (1999) Curie point depth based on spectrum analysis of the magnetic anomaly data in East and Southeast Asia. Tectonophysics 306(3–4):461–470

Treitel S, Clement WG, Kaul RK (1971) The spectral determination of depths of buried magnetic basement rocks. Geophys J Roy Astr Soc 24:415–428

Trifonova P, Zhelev Z, Petrova T, Bojadgieva K (2009) Curie point depths of Bulgarian territory inferred from geomagnetic observations and its correlation with regional thermal structure and seismicity. Tectonophysics 473(3–4):362–374

Turcotte DL (2011) Fractals and chaos in geology and geophysics. Cambridge University Press, Cambridge

Fractal Faults: Implications in Seismic Interpretation and Geomodelling

Ravi Prakash Srivastava

Abstract Nature is not random as we often assume for the simplicity of mathematical calculations. Scaling or power laws, also known as fractal behavior, are ubiquitous in nature, and the analysis of many physical properties of the earth shows fractal behavior. In this chapter attempt is made to integrate the geological understanding and fractal behavior of the faults to use this knowledge in practice. This understanding could potentially help to reduce the uncertainty and risk in the fault modelling and some of the properties associated with the faults such as transmissibility and shale gauge ratio. The study aims at understanding faults in hydrocarbon reservoirs, however, the concepts are universally valid and could be useful for the readers interested in seismology or mining-related studies as well.

1 Introduction

In this chapter, I am tasked to combine the understanding from two different worlds, one called ‘Fractals’ that follows though simple but a fascinating mathematics of self-similarity and power law observed in many natural phenomena and the other called ‘Faults’ encountered in geological studies. This chapter is by no means a new research finding, rather an account of the most updated use of fractal concept in geological understanding of faults and their significance in geological modelling of hydrocarbon reservoirs.

The study about the mapping and modelling faults in Earth science is one of the most important issues, particularly because of its serious impact on the work process. For example, it can have severe impacts on the mining industry and can lead to fatal consequences if faults are not understood before commencement of the mining work. Unexpected faulting can cause dilution and ore losses in underground metal mines, shutdowns and delays in production in underground coal mines with

---

R.P. Srivastava (✉)
National Geophysical Research Institute, Uppal Road, Hyderabad 500007, Telangana, India
e-mail: ravi.ngri@gmail.com

V.P. Dimri (ed.), *Fractal Solutions for Understanding Complex Systems in Earth Sciences*, Springer Earth System Sciences,
DOI 10.1007/978-3-319-24675-8_3

consequent severe financial losses, geotechnical hazards that impact upon safety, etc. (Dimitrakopoulos and Li 2001).

In oil and gas industry, again faults are very important. In this case both, large and very small scale faults influence the reservoir model. Here, the faults clearly visible in seismic data are considered large, and many faults, which are extracted based on some seismic attributes (spatial correlation techniques, viz. semblance, etc.) but not resolved by the reflection seismic data, are considered small scale faults. The presence of faults does influence the fluid flow properties in a reservoir. The magnitude of influence is mainly dependent on the intensity of faulting and the relative permeability contrast of the fault permeability compared with the permeability of the undeformed reservoir. Many factors control the influence of the faults on fluid flow, some of them are: the degree of faulting and strain localization, the geometry of the faults, the lithologies that have been involved in the faulting, their mechanical properties during faulting and the diagenetic alteration of the fault rock during burial.

Generally, for siliciclastic sediments the fault rocks have lower permeability than the undeformed sediments. It is crucial to model the faults' impact on the fluid flow within the reservoir to achieve realistic fluid flow and drainage patterns within dynamic reservoir models.

The motivation to use fractal theory in understanding the fault geometry comes from the field observations and has also been reported in many studies that the faults show fractal/scaling behavior in terms of fault length and displacement (Spyropoulos et al. 2002; Scholz et al. 1993), fault zone thickness versus fault throw (Childs et al. 2009). Also, it is important to mention that it is often easy to identify and interpret large faults in seismic data, but the interpretation and identification of faults is not very easy when they are small and hence below the resolution limit of seismic data. Thus, an attempt is made to integrate fractal behavior of faults with geological knowledge of the faults to better model the smaller faults in the reservoir model (called geo-model).

Some researchers have used simulation methods for fault populations based on various approaches including fractals which have been developed in the modelling of petroleum reservoirs (e.g. Gauthier and Lake 1993; Munthe et al. 1993; Chilès et al. 2000; Mostad and Gjerde 2000; Holden et al. 2003). The modelling results are often crosschecked with the well data if available.

2 What Is 'Fractal', 'Fault'

Assuming that the readers of this book may be from different disciplines of science, the two main terms used in this chapter 'fractal' and 'faults' are defined below for the sake of completeness.

3 Fractal

The main theme of this volume deals with the fractal; hence, instead of repeating the definitions of fractals, an attempt is made to describe what does fractal mean when we talk about the faults in geology. Traditionally fractal is defined as a geometrical shape having self-similarity independent of scale. Often, we see that faults do show self-similar pattern, though not on all the scales. In addition, it is known fact that none of the natural fractals exhibit self-similarity on all scales except synthetic fractals. In this context, we are more interested in statistical definition of fractal behavior of faults. Statistically, if certain property (measured quantity) of an object follows power-law relation or long-term dependence on another property of the same object, then we say that it is fractal. For example, it is known that there is a long-term relation between magnitude and frequency of the earthquakes (Dimri 2000, 2005a, b; Scholz 1997; Turcottee 1992). Here, both magnitude and frequency are the properties related to earthquake. Similarly, an attempt is made to explore which properties of the faults are fractal. Once, we succeed in establishing a fractal behavior, we can use it in statistical analysis e.g. in forecasting the number of faults, or interpolation or extrapolation of one property of the fault based on another observed property.

4 Fault

A fault is the result of shear failure within a rock mass causing a displacement of subplanar zone due to sliding motion. There are many types of faults, but a common and easy-to-understand fault is normal fault. The geometry of normal fault is shown in Fig. 1, with the annotation of commonly used terms to describe a fault. In a normal fault, the hanging wall moves downwards, while the footwall moves upwards. In a reverse or thrust fault, the hanging wall moves upwards, while the footwall moves downwards (Fig. 2). In a strike slip fault, the sense of motion on the fault plane is horizontal. Frictional processes within the fault zone produce sheared material known as fault rock, which is characterized by the different petrophysical properties than the surrounding rocks.

Note that in case of normal fault, it is extension of the rock mass, whereas in case of reverse fault it is shrinking of rock mass. To be mathematical, one can say heave (h) is positive in case of normal fault and it is negative in case of reverse fault. However, geologists do not define it in this way.

In Fig. 3 a schematic fault is shown to describe some common terms used in fault geometry and Fig. 4 shows natural fault found in nature. The principal stresses involved in different kind of faults are shown in Fig. 5.

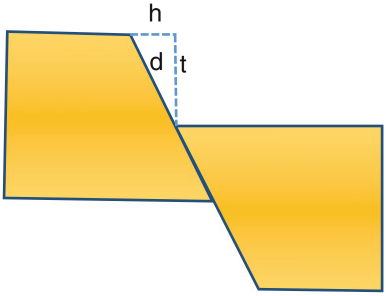

Fig. 1 Normal fault, *h* heave, *t* throw, *d* displacement

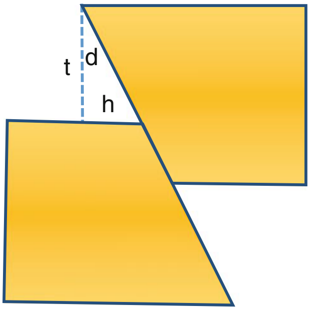

Fig. 2 Reverse fault, *h* heave, *t* throw, *d* displacement

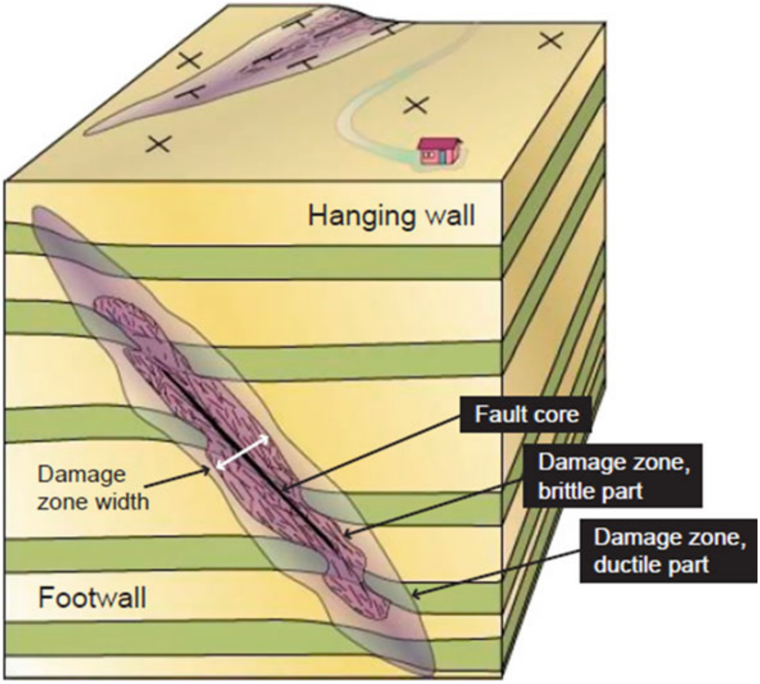

Fig. 3 Figure explains the common terms used to describe a fault geometry, modified from Fossen and Gabrielsen (2005)

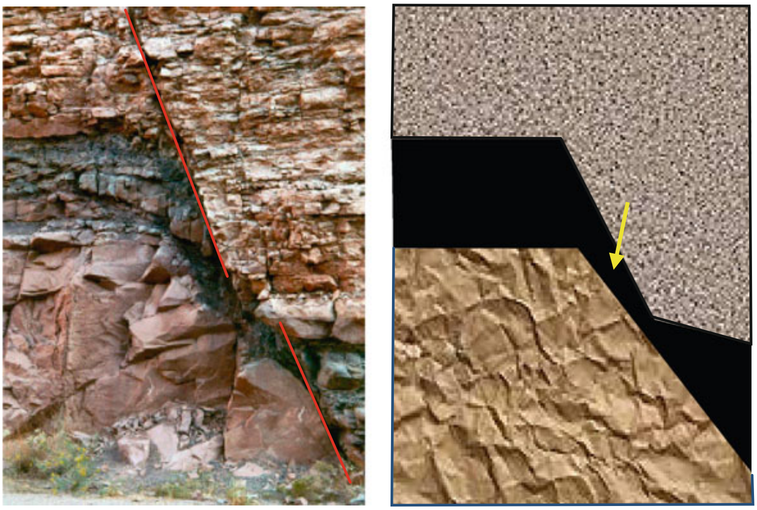

Fig. 4 Natural fault, notice the *brown shale* smeared along the fault plane. *Thin red line* highlights fault plane. A simplified interpretation of the natural fault is shown in (**b**) which usually geologists produce and that goes into geo-model. Important is to notice the smear of the shale material along the fault plane (shown by *arrow*), which makes this fault sealing, and fluid flow is not possible across the fault in such cases

5 Fractures

Fractures are often associated with the faults, however, they occur independent of fault presence. Fractures also show similar characteristic as faults, and they have high significance in reservoir modelling.

Fractures can be defined as mechanical breaks in rocks involving discontinuities or displacement across surfaces or narrow zones’. A conceptual model of fracture formation is shown in Fig. 6.

There are three major types of fractures (Fig. 7) such as:

1. Dilatant fracture including joints
2. Shear fractures/faults
3. Closing fractures/stylolite

As the state of stress in the earth’s crust is compressive, dilatant fractures usually require elevated pore pressure in order to form in the sub-surface. Closing fractures tend to form more easily in carbonates than in siliciclastic rocks and become more prevalent at depth. Whereas faults can occur at any depth in the brittle crust. Most faults initiate and propagate as dilatant fractures, but not all fractures will become faults. Those interested in more details about the fractures may refer to (Gillespie et al. 1993).

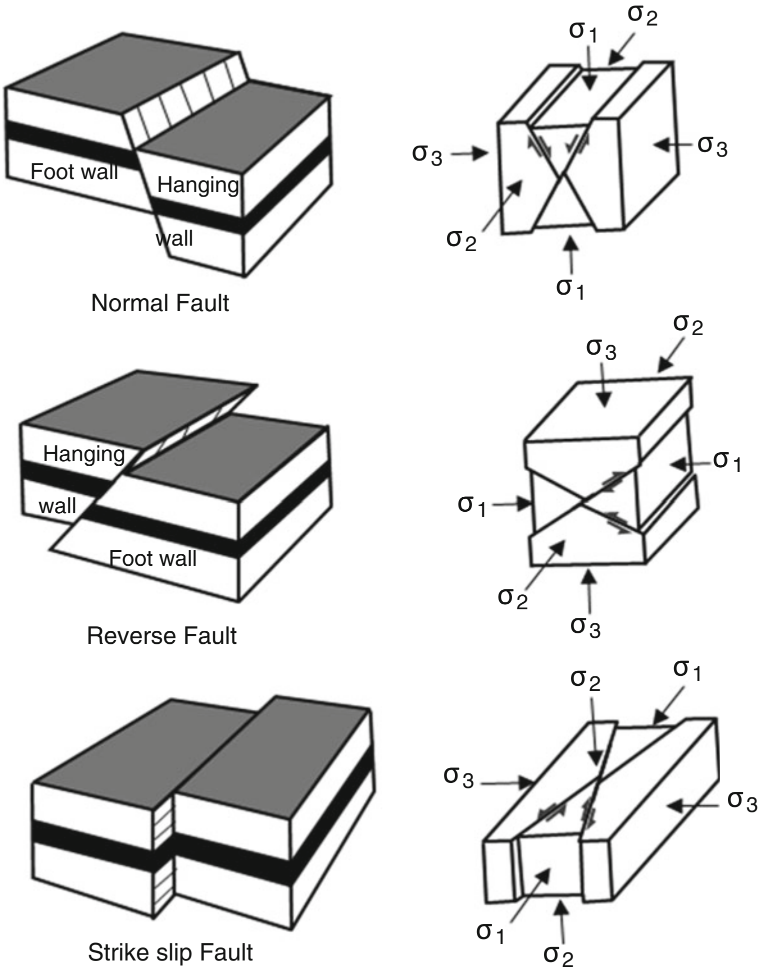

Fig. 5 Fault types and governing stresses involved in the faulting process (modified from Ramsay and Huber 1987). *Sigma 1* is maximum principal stress direction, *sigma 2* is intermediate principal stress and *sigma 3* is minimum principal stress direction

In reservoir modelling (mostly in case of oil and gas reservoirs, with high economics involved), the term ‘fractured reservoir’ is used to describe the reservoirs in which fractures enhance permeability (Dimri et al. 2012). This permeability enhancement is most important in formations with low permeability rocks, such as carbonates and tight sands. Fractured reservoirs often contain all the three kinds of fractures as described above, but dilatant fractures and faults are most important for the fluid flow in the reservoir. In most fractured reservoirs, although the fractures provide essential additional permeability to the reservoir, their contribution to

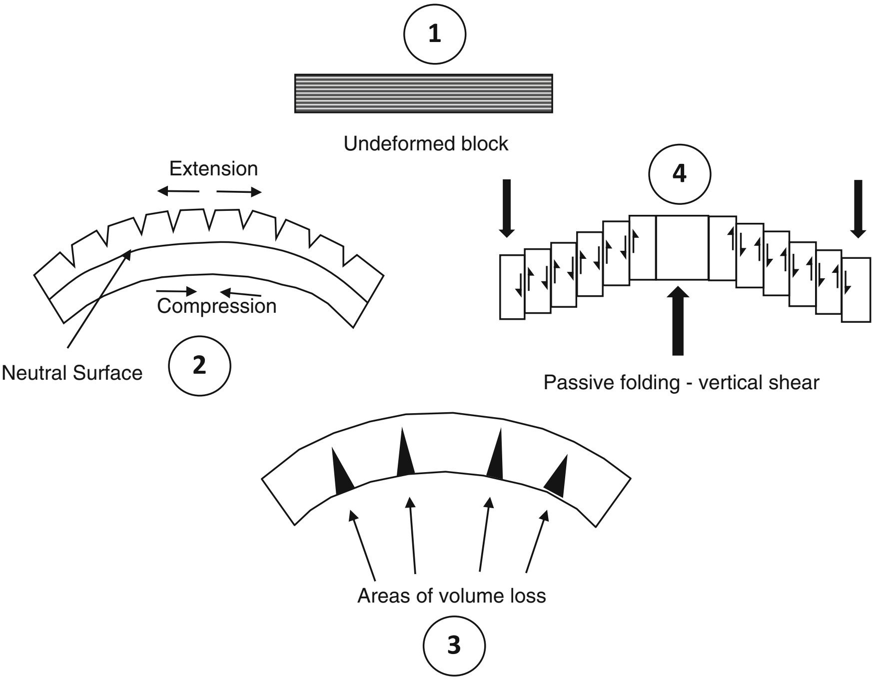

Fig. 6 Fracture formation process (*1*) undeformed rock mass, (*2*) fracture development due to extension of upper surface, simultaneously compression takes place in lower surface as shown in (*3*), later depending on the rigidity of the rock mass, fractured parts may fail and create several small faults due to vertical shear as shown in step (*4*)

fracture porosity is small. Typically, in a producing reservoir, the fluids are drawn from rock matrix into the high permeability pathways provided by the fracture system.

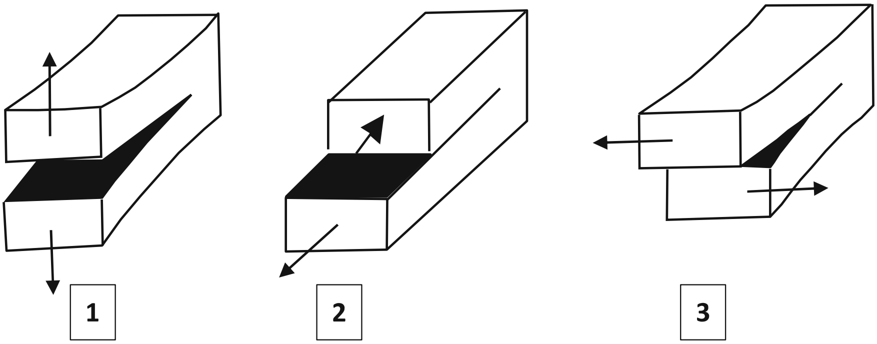

Fig. 7 Types of fractures (*1*) Dilating fracture (*2*) and (*3*) are shear fractures or faults

6 Are Faults Fractal?

There is fairly good amount of published research work which dwells on the fractal geometry of faults particularly in light of seismological studies (Sunmonu and Dimri 2000; Sengupta et al. 2011 and references therein). It has been shown that the faults and lineaments show fractal behavior. A closer look at the earthquake foreshock and aftershock analysis reveals that earthquake's magnitude and frequency follow fractal behavior (Dimri et al. 2005).Extending the notion of earthquake analysis to the faults, it is likely that the faults should show a power-law size distribution and a linear scaling of the strain with the length of the fault.

In some instances, besides power-law distribution of the faults, some fault populations exhibit exponential laws for the distribution of the fault size. Spyropoulos et al. (2002) suggest that the power-law distribution and exponential distribution of the faults are the transition regimes between the two end member stages. These end member stages are an initial uncracked state and the saturated state in which the cracks are evenly spaced. According to the experimental and numerical modelling done by Spyropoulus et al. (2002) the power-law distribution appears only in the process of the undisturbed growth. In the processes of nucleation and of coalescence and saturation they observed an exponential law. Readers are encouraged to look at the paper by Spyropoulus et al. (2002) for the definition of nucleation, coalescence and saturation of the cracks in their experiment.

Davy et al. (1990) based on the laboratory experiment mimicking India–Asia collision concluded that the continental faults are fractal in nature and explained the occurrence of large stable basins based on this assumption. Further, Endres et al. (2008) analysed several fracture attributes such as orientation, density or spatial distribution and the fracture length in greater detail. They proposed that, if the ratio of 'long' and 'short' fractures is constant over different scales, then it follows the law of scale invariance, implying that the relationship is fractal. This means that there is a power-law relation between those 'long' and 'short' fractures. In general, the theory suggests that various fault parameters are invariant with respect to scale or are 'self-similar', providing a model that can be used for predictive purposes. Based on empirical data analysis, fault size distributions (throw or length) can be described by a power-law model over a wide range of fault sizes such that:

$$\log(N) = k - \beta \log(L) \tag{1}$$

where:

N is the cumulative number of faults of size greater than or equal to fault size 'L'.
L is either length or throw of the fault.
k is a function of the fault density and when k is high, the fault density is also high.
β is the fractal dimension of the fault population that defines the relative number of large and small faults; when β is high, the number of small faults is high relative to the number of large faults.

Fig. 8 Cumulative number of faults versus fault length, plotted on log–linear scale (modified from Gupta and Scholz 2000)

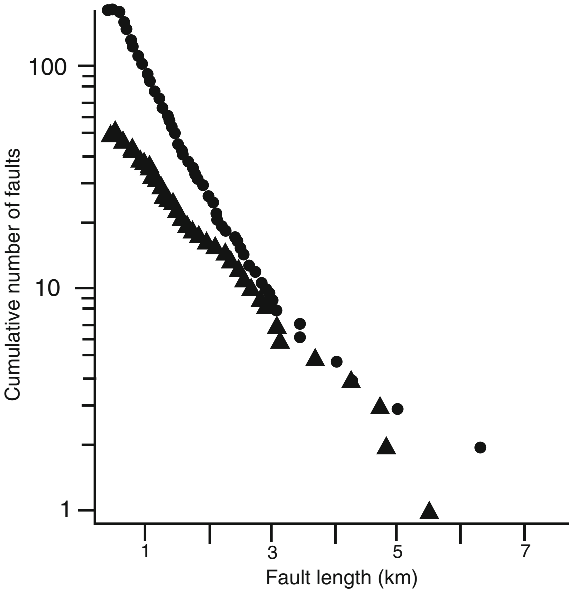

Apart from the data obtained from the experimental study, many authors attempted to find scaling laws for natural faults. It is interesting to note that the researchers, who used data from only one set of fractures, reached distributions very similar to the results of Spyropoulos' (2002) experimental study. The closest agreement seems to occur with the results of Gupta and Scholz (2000), who examined data from the natural faults in the Afar depression. They observed a strain regime transition from a power law to an exponential law for the frequency-size distribution (Fig. 8), when faults reach a certain density. For the faults of the Afar depression, this density equals 0.6 km of fault length per square kilometre. This corresponds with a strain of 6–8 %. Above this density, faults grow mostly by coalescence until the area is saturated.

Thus, we believe that for all practical purposes it is safe to go with the assumption that the properties of the faults are fractal.

7 Data Sampling

As defined earlier, fractals are a statistical behavior of the data that follows power law. The problem in analysing the scaling laws of faults is spare sampling of the data to establish a reliable distribution law. Often, to overcome inadequate data, many researchers used data from different geological and tectonic settings, the distribution and scaling laws established with such data may depend on different material properties. For a confident analysis, it is important to acquire a data set over several orders of magnitude but in a single tectonic environment and rock type is necessary.

Other problems arise if the size of the sampled domain is very small or if the domain is so small that it is below resolution limit of the measurement. These effects are termed as truncation and censoring after Bonnet et al. (2001). Truncation is the underestimation of small fractures due to resolution limitations. These effects can be seen in the density distribution. The slope of the power-law curve then goes through zero and becomes positive for the smallest fractures. Censoring occurs when a limited size of the area is examined compared to the extent of the target object. For example, if a large fault being investigated is sampled in a limited area, then it can be completely missed or erroneously interpreted.

8 Some Examples

Figure 9 is based on the observed data from the faults in one location during a field work. It shows the linear relationship between fault zone thickness (fault core) and fault throw in a log–log plot. However, if plotted in a log–linear scale it will show

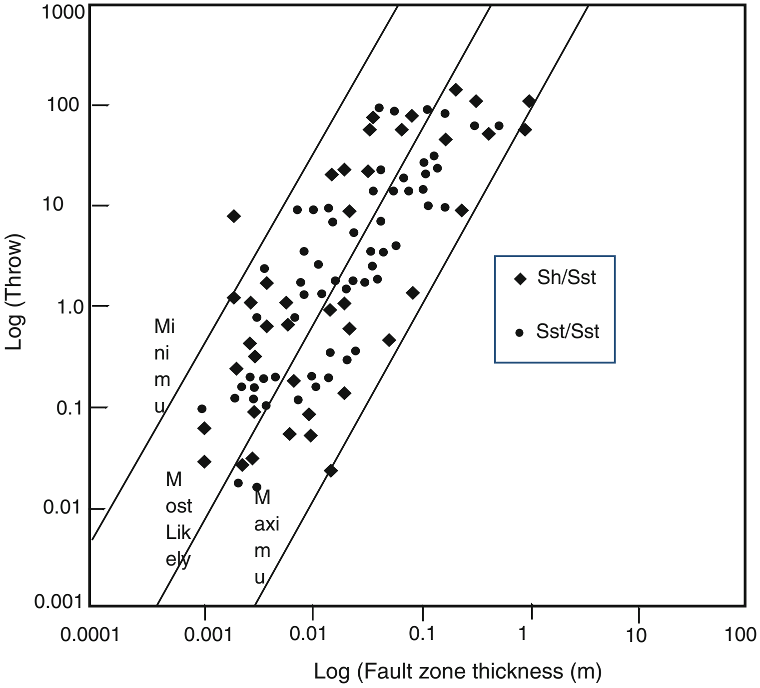

Fig. 9 Relation between fault core thickness and fault throw. In a log–log plot this is a linear relationship. The data is from outcrop study in a faulted sandstone

power-law behavior. Though the observation points are scattered and it is difficult to fit a unique line, this kind of observation gives an opportunity to find minimum, maximum and most likely cases which are an important input in the fault seal modelling. The plot shows that the wider fault zone (fault core) implies larger fault throw and vice versa.

Mathematically, the above observation can be modelled using fractal model of the fault throw versus fault thickness relationship given by the following equation:

$$\log(T) = N\log(L) - c \tag{2}$$

where T is the fault throw; N is the model slope, also known as the scaling exponent, which is often a characteristic value in a given region, or location, L is fault length and c is the model intercept. Constant c can be determined by fitting a line through the observed points.

The above relationship becomes even more important when there is less data available, and we need to rely on some kind of model. To calculate transmissibility multipliers of the fault, fault zone thickness (fault core) information is needed, which can be computed using above empirical relationship.

The example shown in Fig. 10 illustrates fault termination and displacement profile. Often such instances are visible when you walk on an area with faults, and you only see a planer view of the area. In such cases faults can be traced and as shown in Fig. 11 a profile of displacement along the fault length can be drawn. This information helps to understand the growth history of the faults and helps to understand the continuation of the fault when fault through is below seismic resolution.

For instance, in Fig. 10 it may happen that the maximum displacement in the centre of the fault is visible in seismic, but as we approach the tip of the fault, the throw of the fault gets smaller and smaller, and in most of the cases it is not possible to observe the tip of the fault in seismic data. However, during seismic

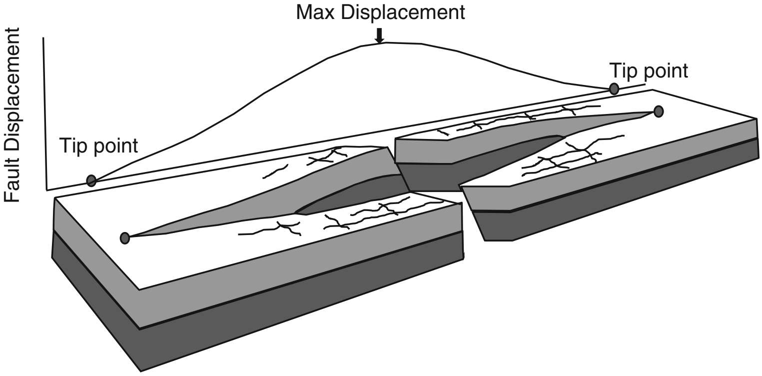

Fig. 10 Model for the fault displacement (slip) distribution. Slip decreases towards the fault tip, and maximum in the central part

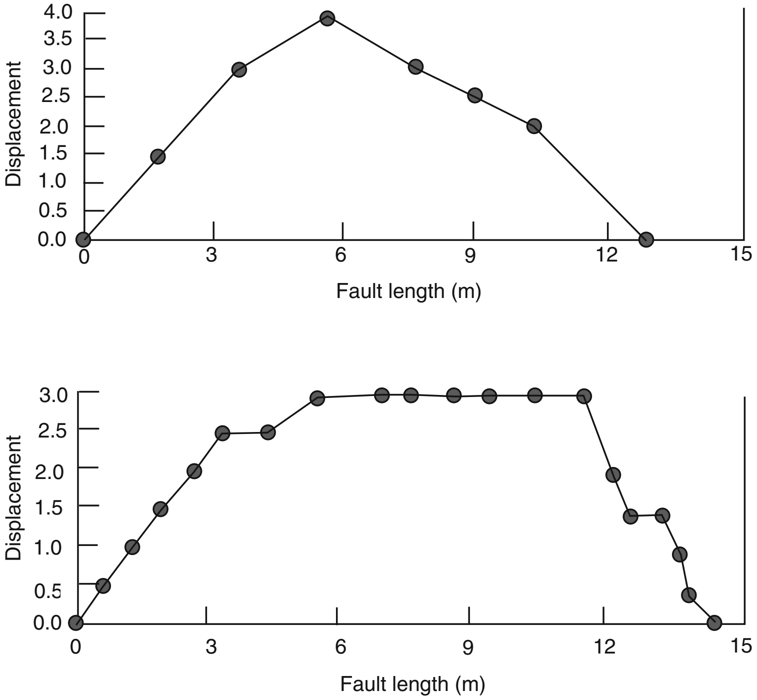

Fig. 11 Displacement (slip) distribution along length profiles in a normal fault

interpretation, geophysicist may terminate the fault interpretation much before than they really exist in nature. This is where such observations in the field help to aid the geophysical interpretation of the seismic data, where things are below seismic resolution and a geological concept is needed to extend the interpretation. The profiles drawn in Fig. 11 give a mathematical estimate of the throw away from the maximum observed through, which is a linear relationship.

9 Conclusions

Several data- based and experimental studies show that properties of faults follow fractal behavior. However, most of the studies on natural faults lack adequate collection of data. A better and detailed data collection could help to improve the understanding of the fractal behavior of the faults. Given the current status of the knowledge available, it is best to use the fractal properties of a fully known fault population as an analogue of the properties of an undiscovered fault population. Also, with the fractal model of the fault prediction it is important to incorporate spatial patterns of available ‘well’ and ‘seismic’ information. The fractal modelling is not a unique modelling, so the results are not deterministic, however, they can be converted into a fault probability map. Spatial correlation of fractal based fault models can be confirmed from the density of fault-intersecting drill holes mapped in the study area. Also, spatial patterns of the fractal based predicted faults can be modelled using variograms and checked with the continuity in the spatial patterns of known faults.

Acknowledgements I am highly indebted to Prof. V.P. Dimri for his kind invitation to contribute a chapter in this volume. He has been a constant inspiration for this chapter, and has been very patient even after my never-ending delays in writing this chapter.

References

Bonnet E, Bour O, Odling NE, Davy P, Main I, Cowie P, Berkowitz B (2001) Scaling of fracture systems in geological media. Rev Geophys 39:347–383

Childs C, Manzocchi T, Walsh JJ, Bonson G, Nicol A, Schopfer MPJ (2009) A geometric model of fault zone and fault rock thickness variations. J Struct Geol 31:117–127

Chilès J-P, Bourgine B, Castaing C, Genter A (2000) Stochastic modelling and simulation of fracture populations in petroleum and geothermal reservoirs. In: Kleingeld WJ, Krige DG (eds) Geostatistics 2000, Cape Town, South Africa, vol 1, pp 413–423

Davy Ph, Sornette A, Sornette D (1990) Some consequences of a proposed fractal nature of continental faulting. Lett Nat 348:56–58

Dimitrakopoulos R, Li S (2001) Quantification of fault uncertainty and risk management in longwall coal mining: back-analysis study at North Goonyella Mine, Queensland. In: Doyle R, Moloney J (eds) Geological hazards—the impact to mining, pp 175–182

Dimri VP (2000) Application of fractal in Earth sciences. A.A. Balkema, Oxford; IBH Pub. Co., New Delhi, p 238

Dimri VP (2005a) Fractal behaviour of the Earth system. Springer, New York, p 207

Dimri VP (2005b) Fractals in geophysics and seismology: an introduction, fractal behaviour of the Earth system. Springer, New York, pp 1–22

Dimri VP, Vedanti N, Chattopadhyay S (2005) Fractal analysis of aftershock sequence of Bhuj earthquake—a wavelet based approach. Curr Sci 88(10):1617–1620

Dimri VP, Srivastava RP, Nimisha Vedanti (2012) Fractal models in exploration geophysics. Elsevier Science Publishers, Amsterdam

Endres H, Samiee R, Lohr T, Krawczyk CM, Tanner DC, Trappe H, Thierer PO, Oncken O, Kukla PA (2008) Quantitative fracture prediction from seismic data. Pet Geosci 14(4):369–377

Fossen H, Gabrielsen RH (2005) Strukturgeologi. Fagbokforlaget, 369 pp

Gauthier BDM, Lake SD (1993) Probabilistic modelling of faults below the limit of seismic resolution in Pelican Field, North Sea, offshore United Kingdom. AAPG Bull 77(5):761–777

Gillespie PA, Howard CB, Walsh JJ, Waterson J (1993) Measurement and characterization of spatial distributions of fractures. Tectonophysics 226:113–141

Gupta A, Scholz CH (2000) Brittle strain regime transition in the Afar depression: implications for fault growth and seafloor spreading. Geology 28:1087–1090

Holden L, Mostad P, Nielsen BF, Gjerde J, Townsend C, Ottesen S (2003) Stochastic structural modeling. Math Geol 35(8):899–914

Mostad P, Gjerde J (2000) Multifractal fault simulation. In: Kleingeld WJ, Krige DG (eds) Proceedings of the geostatistics 2000, Cape Town, South Africa, pp 358–368

Munthe KL, More H, Holden L (1993) Sub-seismic faults in reservoir description and simulation. SPE paper no 26500

Ramsay JG, Huber MI (1987) The techniques of modern structural geology. Academic Press, San Diego, 700 p

Scholz CH (1997) Size distribution for large and small earthquakes. Bull Seismol Soc Am 87: 1074–1077

Scholz CH, Dawers NH, Yu J-Z, Anders MH, Cowie PA (1993) Fault growth and fault scaling laws: preliminary results. J Geophys Res 98:21951–21961

Sengupta P, Nath SK, Thingbaijam KKS, Mistri S (2011) Fractal analysis of major faults in India on a regional scale. JGSI 78:226–232

Spyropoulos C, Scholz CH, Shaw BE (2002) Transition regimes for growing crack populations. Phys Rev 65:056105

Sunmonu LA, Dimri VP (2000) Fractal geometry of faults and seismicity of Koyna-Warna region west India using landsat images. Pure Appl Geophys 157:1393–1405

Turcotte DL (2011) Fractals and Chaos in geology and geophysics. Cambridge University Press, Cambridge, New York, 221 p

Detrended Fluctuation Analysis of Geophysical Well-Log Data

D. Subhakar and E. Chandrasekhar

Abstract Geophysical well-log data provide a unique description of the subsurface lithology, as they represent the depositional history of the subsurface formations, vis-à-vis the variation of their physical properties as a function of depth. However, a correct identification of depths to different lithostratigraphic units is possible only by using effective data analysis tools. In the present study, detrended fluctuation analysis (DFA) technique has been applied to gamma-ray log, sonic log and neutron porosity log of three different wells, A, B and C, located off the west-coast of India (i) to discuss the statistical characterization of different subsurface formation properties based on their fractal behavior and (ii) to identify the depths to the tops of formations by comparing the results of DFA with those of wavelet analysis. The DFA technique primarily facilitates to understand the intrinsic self-similarities in non-stationary signals like well-logs by determining the scaling exponent in a modified least-squares sense. In the present study, DFA was carried out in two ways using (i) non-overlapping window method to determine the global scaling exponent and (ii) overlapping window method to determine the local scaling exponent. In the non-overlapping window method, data segments of different windows, each having equal length, were first used to estimate the average fluctuations. The linear least-squares regression between the logarithm of average fluctuations and the logarithm of window lengths then defines the global scaling exponent. For gamma-ray logs of all the three wells, the non-overlapping window method shows two distinct ranges of global scaling exponents, in the ranges 0.5–1.0 and 1.0–1.6. While the former signifies the presence of persistent long-range power-law correlations, indicating the stochastic nature of the sedimentation pattern in the data, the latter indicates the existence of short-range correlations of non-stochastic nature but cease to be of power-law form. On the other hand, the sonic and neutron porosity logs of wells A and C show a single global scaling exponent value of greater than 1.0, signifying the non-stochastic nature of the interval transit time (primary porosity) and neutron porosity, respectively, in the entire data sequence as a function

---

D. Subhakar · E. Chandrasekhar (✉)
Department of Earth Sciences, Indian Institute of Technology Bombay,
Powai, Mumbai 400076, India
e-mail: esekhar@iitb.ac.in

V.P. Dimri (ed.), *Fractal Solutions for Understanding Complex Systems in Earth Sciences*, Springer Earth System Sciences,
DOI 10.1007/978-3-319-24675-8_4

of depth. However, in case of well B, the sonic and neutron porosity logs show two distinct ranges of global scaling exponents, one in the range 0.5–1.0 and the other between 1.0 and 1.5, probably suggesting the effect of different diagenetic conditions in well B, compared to those in wells A and C. Choosing a particular window length and sliding it with unit shifts over the entire length of data for estimating the continuous variation of local scaling exponents as a function of depth defines the overlapping window method. This has been applied on all the log data sets of all the wells to generate the plots of variation of local scaling exponents as a function of depth. Comparison of such plots of variation of local scaling exponents of all the logs with the wavelet scalograms of respective logs revealed that the obtained depth estimates agree well with the known lithostratigraphy of the study region.

1 Introduction

There has been a steady progress in the geophysical well-log data analyses for the past three decades, right from the early visual inspection methods to the development of new and fast data analysis techniques to analyse and interpret geophysical well-log data for a better understanding of the subsurface formations they offer, in a broader perspective (Chandrasekhar and Rao 2012). Principal component analysis (Wolff and Pelissier-Combescure 1982), multivariate analysis and non-parametric regression (Lee and Datta-Gupta 1999), artificial intelligence (Lim et al. 1999) and cluster analysis (Antelo et al. 2001) techniques were used to analyse well-log data for detection of electrofacies.[1] Anxionnaz et al. (1990) carried out cluster analysis for the identification of lithofacies. Later, Fourier analysis (Tiwari 1987) and semivariogram analysis (Jennings et al. 2000) were also employed to study periodicities and cyclicities in the data and assess the degree of similarity between sample pairs as a function of separation distance within the subsurface formations. Kumar and Kishore (2006) studied the classification of electrofacies, by joint application of neural networks and cluster analysis.

Another novel technique, known as wavelet analysis (WA), has been proven to be one of the most efficient ones for providing the space localization of different subsurface formations. WA has found its wide applications in effectively describing the inter-well relationship (Jansen and Kelkar 1997), determining the sedimentary cycles (Prokoph and Agterberg 2000), reservoir characterization studies (Panda et al. 2000; Vega 2003) and determining the space localization and identifying the

---

[1] A set of log responses that characterizes a bed and distinguishes it from others (Serra and Abbot 1980).

depths to the tops of formations (Chandrasekhar and Rao 2012). Of late, it has been recognized that well-log data display multifractal behavior and thus can be studied using fractal analysis to determine scaling exponents, which in turn are related to the physical properties of the subsurface formations. Khue et al. (2002) applied a generalized multifractal analysis to study the classification of sediment formations. Later, Lopez and Aldana (2007) made a wavelet-based fractal analysis of well-log data for facies recognition and classified different formations based on their fractal dimension. More recently, Hernandez-Martinez et al. (2013) applied detrended fluctuation analysis (DFA) to well-log data for identification of facies associations. Chandrasekhar and Dimri (2013) described a methodology for wavelet-based fractal analysis.

In the present study, we employ the DFA technique to gamma-ray log, sonic log and neutron porosity log data sets of three different wells located off the west-coast of India, to (i) statistically characterize different properties of subsurface formations based on the fractal behavior of well-log data and (ii) identify the depths to the tops of formations by comparing the results of DFA and wavelet analysis. The organization of the chapter is as follows. Section 2 briefly discusses the geology of the study area. Section 3 details the data used in the present study. Section 4 discusses the basic theory of DFA technique and sequential steps to be followed to determine the scaling exponents by DFA. Section 5 describes the methodology employed in the present work, wherein we have separately used non-overlapping window method and overlapping window method to determine the global and local scaling exponents, respectively. Section 6 provides the results and discussion of the interpretation of the results. Section 7 provides the conclusions of the present study.

2 Geology of the Study Area

The Bombay High is the largest hydrocarbon field in India, covering an area of about 1500 km^2, located in the western offshore basin (Fig. 1a). The oil and gas reservoirs are mostly located in the Cenozoic sediments and are also found in the fractured basement, with the most important among the accumulations being those in the Miocene carbonate section (Bhandari and Jain 1984). The main oil and gas reserves (pay zones) are L-I, L-II, L-III (limestone) and S-I (sandstone). The deepest L-III pay zone (located at about 1300 m) of early Miocene is the largest and the most important of all the pay zones, having a thick oil column with a considerably thick gas cap over the crest. The L-II zone (located at about 990 m) of the Middle Miocene is the next important pay zone. Both L-I and S-I are gas reservoirs of middle Miocene. Figure 1b provides the geological and lithostratigraphic details of the study region.

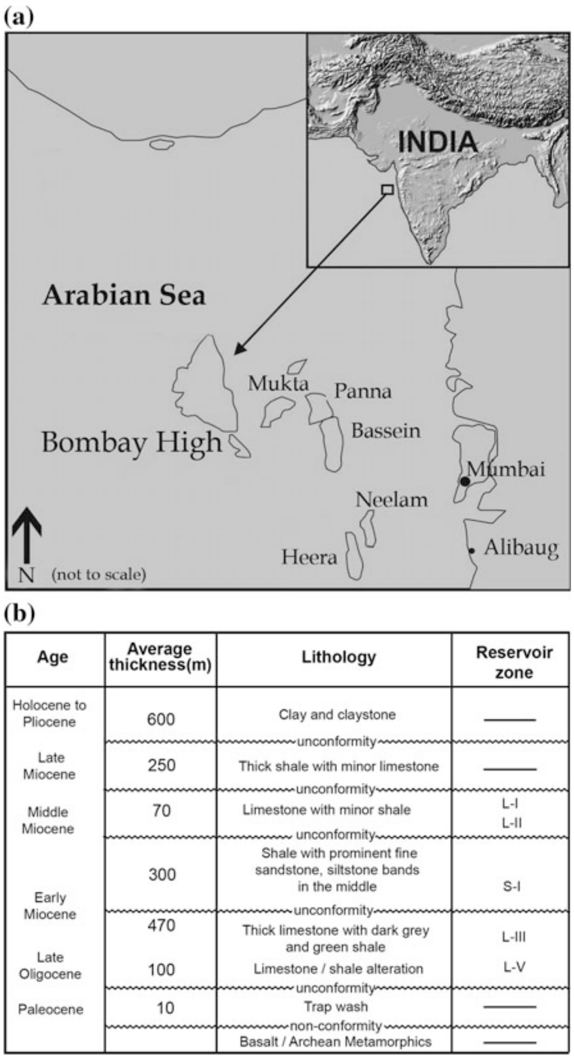

Age	Average thickness(m)	Lithology	Reservoir zone
Holocene to Pliocene	600	Clay and claystone	———
		unconformity	
Late Miocene	250	Thick shale with minor limestone	———
		unconformity	
Middle Miocene	70	Limestone with minor shale	L-I L-II
		unconformity	
Early Miocene	300	Shale with prominent fine sandstone, siltstone bands in the middle	S-I
		unconformity	
	470	Thick limestone with dark grey and green shale	L-III
Late Oligocene	100	Limestone / shale alteration	L-V
		unconformity	
Paleocene	10	Trap wash	———
		non-conformity	
		Basalt / Archean Metamorphics	———

Fig. 1 **a** Geographical location of the study region (Bombay High) and its contiguous regions in Western India (after Chandrasekhar and Rao 2012). **b** Lithostratigraphic units of Bombay High region (not to scale) (after Bhandari and Jain 1984)

3 The Database

For the present study three logs: gamma-ray (GR) log, sonic (DT) log and neutron porosity log were used from three wells: well-A, well-B and well-C, located in Mumbai offshore (Fig. 1a), which is one of the largest oil and gas producing basins of India. The data were procured from Oil and Natural Gas Corporation (ONGC), India. The wells are separated roughly by a distance of about 10 km from each other and each represents a vertical section of approximately 500 m below the sea floor. The data of all the wells were sampled at an interval of 15 cm. Prior to further

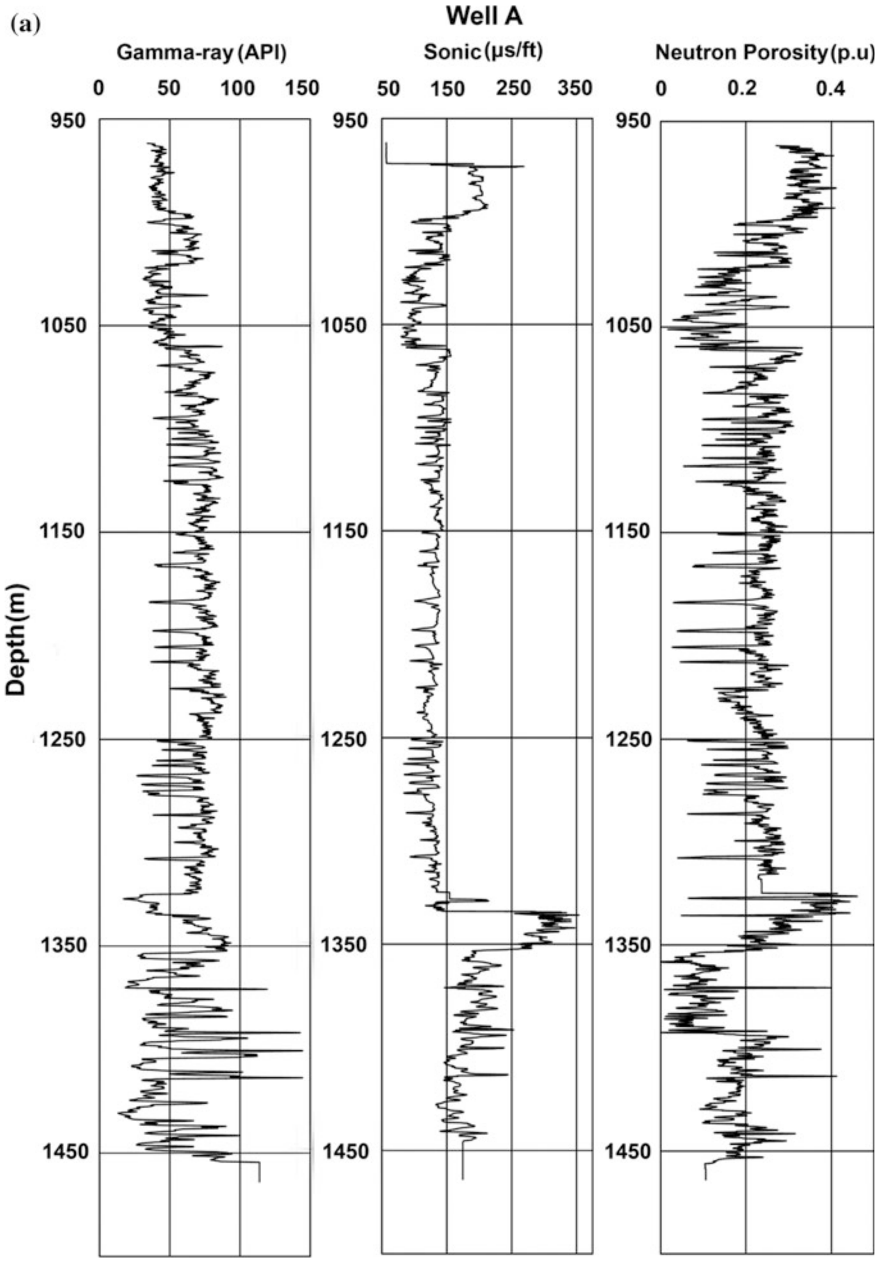

Fig. 2 Raw data sets of gamma-ray log, sonic log and neutron porosity log of **a** Well-A, **b** Well-B and **c** Well-C of Bombay-High region

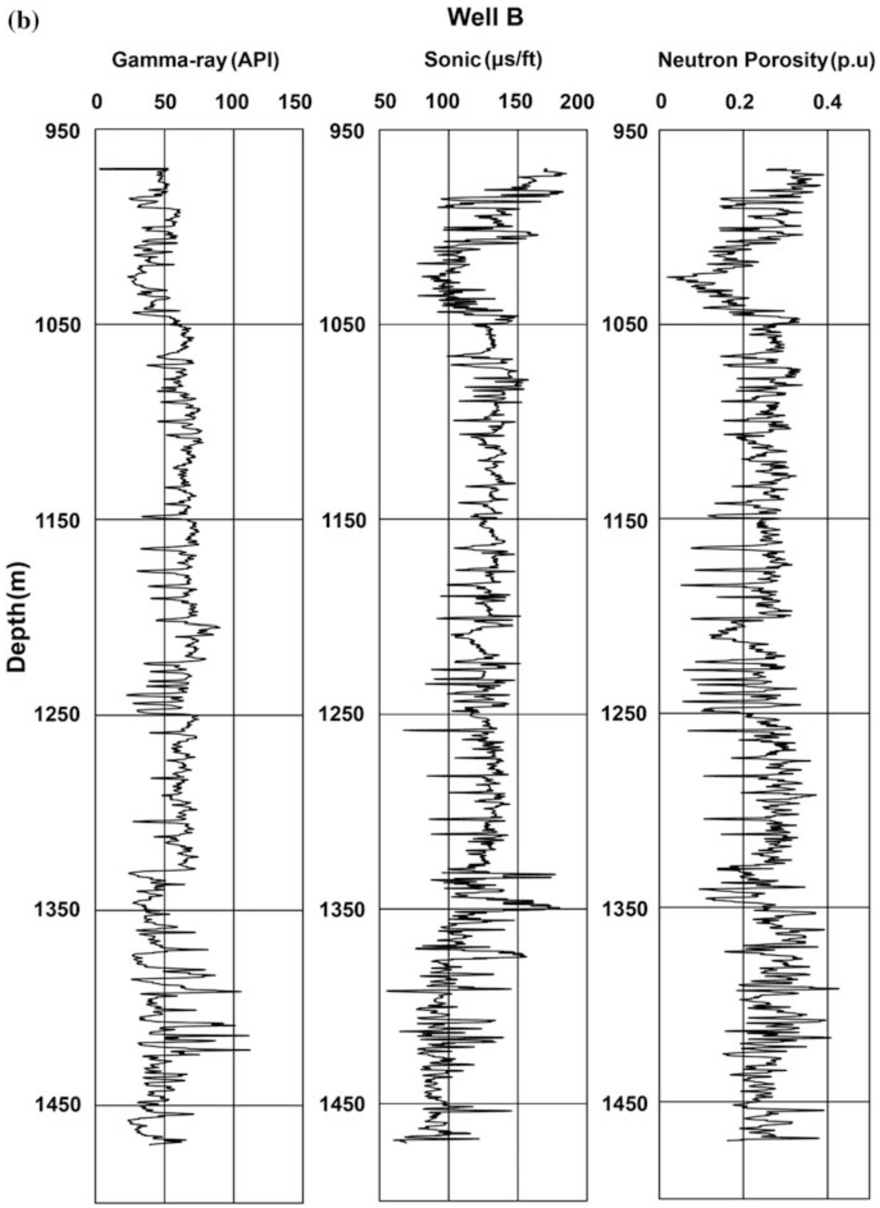

Fig. 2 (continued)

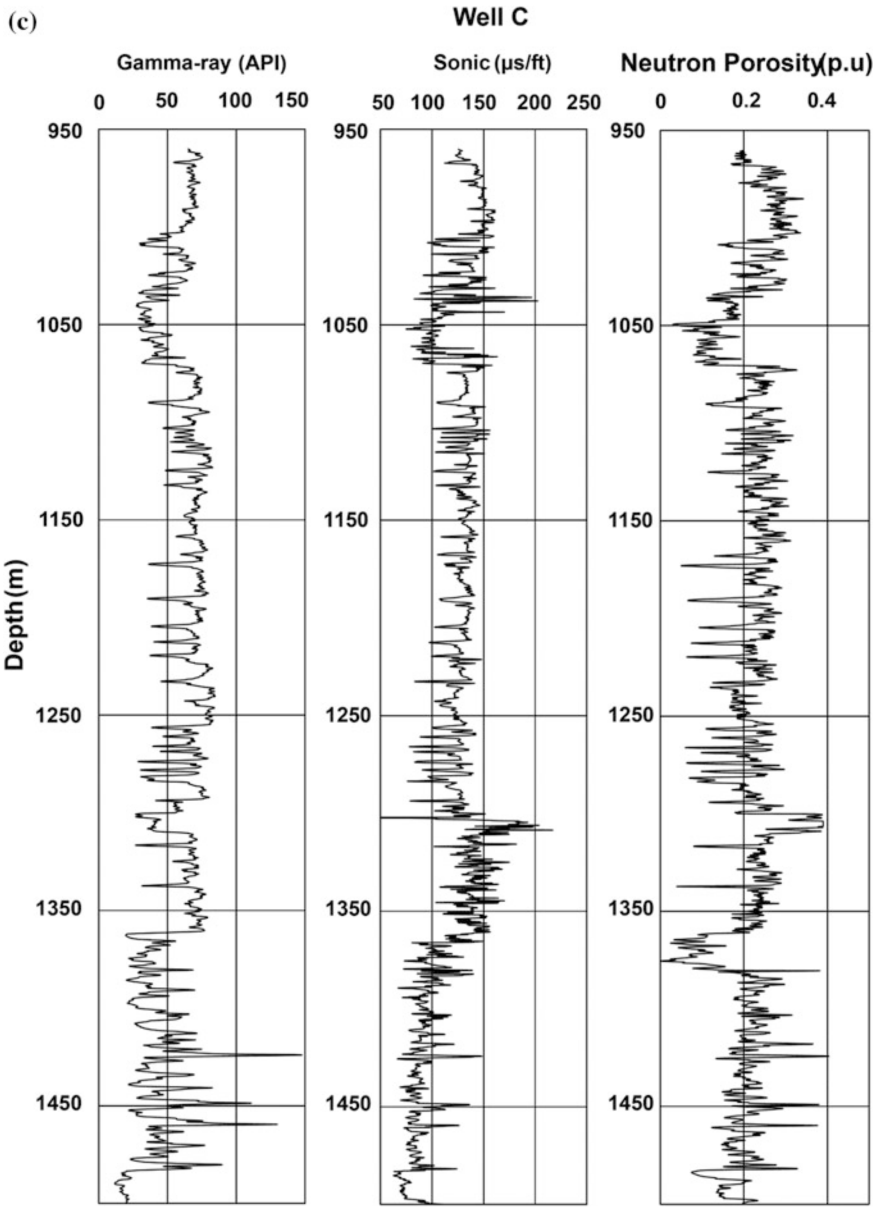

Fig. 2 (continued)

analysis, the amplitudes of neutron porosity logs of all the wells were magnified by a factor of 100 to obtain better statistical inferences. Figure 2 shows different log data sets as a function of depth (with depth increasing from top (sea floor) to bottom), corresponding to well-A (Fig. 2a), well-B (Fig. 2b) and well-C (Fig. 2c).

4 Basic Theory and Estimation of Scaling Exponents by Detrended Fluctuation Analysis

The DFA technique primarily facilitates to study the intrinsic self-similarities in non-stationary signals in a modified least-squares sense. By self-similarity we mean, the fractal nature of the signal under study. The self-similar nature of a signal is mathematically expressed by (Goldberger et al. 2000; Peng et al. 2000)

$$x(t) \overset{d}{\equiv} s^{\gamma} x(t/s) \tag{1}$$

where '$\overset{d}{\equiv}$' implies that the statistical properties on both sides of Eq. (1) are equal. In other words, a time sequence, $x(t)$, rescaled on one axis, by a factor, s, $(t \rightarrow t/s)$ and on the other axis by a factor of $s^{\gamma}\,(x \rightarrow s^{\gamma}x)$, bears identical statistical properties, with γ being the self-similarity parameter (see Goldberger et al. 2000 for more details).

Generally, the DFA describes a procedure to determine the fractal behavior in the form of scaling exponents of signals generated from stochastic and non-stochastic processes. For estimation of scaling exponents through DFA, the signal under investigation must be unbounded, which can be converted to a self-similar process by integration (Goldberger et al. 2000). The thus generated integrated series is divided into short windows (of equal length) and the average fluctuation associated with each window of data is obtained by calculating the trend (linear least-squares fit) of the selected window and removing it from each data point of the corresponding window. This is repeated for various window lengths of data. The scaling exponents are then determined from the least-squares linear regression between the logarithm of average fluctuation and the logarithm of length of the corresponding window. Mathematically, the sequential procedure to be adopted in the DFA technique is as follows.

1. First generate an integrated series $y(m)$ of the N-point spatial data sequence, say, $x(s)$, by estimating

$$y(m) = \sum_{i=1}^{m} [x(i) - \bar{x}] \quad m = 1, 2, 3 \ldots N \tag{2}$$

   $\bar{x}$ being the average of N data points. As one can easily observe, the integrated series thus obtained (Eq. 2) is similar to a random walk and the outcome of each value is based on its previous value.
2. Next, divide the m-length integrated series into various m/k non-overlapping windows of equal length, each consisting of k number of samples.
3. Compute the least-square fit to the data points of each window. This represents the local trend $y_k(m)$.
4. Detrend the integrated series, $y(m)$, by subtracting the local trend $y_k(m)$ from corresponding window. For a window of length k, the average fluctuation, $F(k)$, of the detrended signal is calculated by

$$F(k) = \sqrt{\frac{1}{m}\sum_{i=1}^{m}\left[y(i) - y_k(i)\right]^2} \tag{3}$$

5. Repeat steps 3 and 4 for various window lengths (k) to provide a power-law relationship between k and $F(k)$, given by $F(k) \approx k^{\gamma}$. Where γ denotes the scaling exponent, determined by linear least-squares regression between $\log(F(k))$ and $\log(k)$, signifying the fractal nature of the data.

Different window sizes (as in step # 2) can be chosen, following the procedure described in Peng et al. (1994). Different values of scaling exponents designate different physical processes responsible for the generation of the signal under study. For example, if a signal is an uncorrelated random noise, then $\gamma = 0.5$. For stochastic processes, γ varies in the range 0.5–1.0 and for non-stochastic processes $\gamma > 1.0$ (Peng et al. 1994; Hernandez-Martinez et al. 2013). Generally, the scaling exponents varying between 0.5 and 1.0 indicate definite power-law correlations present in the data. Whereas, the scaling exponent values greater than 1.0 indicate the existence of persistent positive correlations in the data but cease to be of power-law nature. For more theoretical details and applications of DFA technique, the reader is referred to Goldberger et al. (2000).

5 Methodology

Figure 3 depicts an example plot of integrated series of gamma-ray log of well-A generated using Eq. (2) (see step # 1 in Sect. 4) for a window length of 53 m. The linear trend shown in each window depicts the linear least-squares fit corresponding to the data segment of that window. To determine the global and local scaling

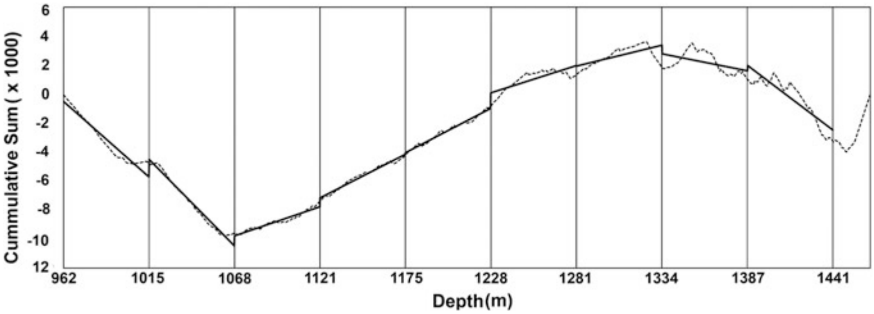

Fig. 3 An example of integrated series (*dotted line*) generated from gamma-ray log of Well-A using Eq. (1). A first-order least-squares fit (*solid lines*) corresponding to each window of length 53 m is also shown

exponents for well-log data sets of three wells, we have applied two methods, viz., (i) non-overlapping window method and (ii) overlapping window method, respectively, to the integrated series (Eq. 3). The procedure to estimate the scaling exponents by non-overlapping and overlapping window methods is rather different. It is described below.

5.1 Non-overlapping Window Method to Determine Global Scaling Exponent

In this approach, first the data segments of different windows, each having equal length, varying in the range 0.75–125 m were considered, following the criteria prescribed by Peng et al. (1994) for choosing the window lengths. A first-order least-squares fit was fit to the data of each window. The local trend (least-squares fit) was removed from each point of the integrated series of the respective windows to calculate the average fluctuations, $F(k)$, corresponding to each window (see step # 4 in Sect. 4). The estimated average fluctuations of all the windows are averaged out to determine the average fluctuation corresponding to that window length. This procedure is repeated for various window lengths, till the window length becomes equal to N/4, where N is the total number of data points (Peng et al. 1994). Figure 4 shows such plots of linear least-squares regression fit between $\log(F(k))$ and $\log(k)$, corresponding to all the well-log data sets of all the wells. The data sets show two distinct global scaling exponents, γ_1 and γ_2, for gamma-ray logs of all the wells and sonic and neutron porosity logs of well-B, indicating short-range and long-range autocorrelations in the data respectively. They signify two statistically different processes associated with the subsurface formations. Interestingly, the boundary depicting the distinction between these two processes is clearly seen in the $F(k)$ values between the window lengths, 4.0–4.5 m, for all the wells. The presence of correlations in the data could be tested by shuffling the original data and comparing the scaling exponents obtained for the original and shuffled data.[2] If $\gamma = 0.5$ for the shuffled data (i.e. uncorrelated random noise), then the observed correlations are due to serial auto-correlations present in the original data. If $\gamma \neq 0.5$, then the observed correlations are due to the broad probability distribution in the data (Kantelhardt et al. 2002). This is tested in the present study. Figure 5a shows an example plot of $\log(F(k))$ and $\log(k)$ drawn for shuffled gamma-ray log data, for which the obtained global scaling exponent, $\gamma = 0.5$. Figure 5b describes the probability distribution of the data, which clearly shows the absence of any data beyond the 98 % confidence level of the Gaussian distribution curve. Both these tests clearly confirm the occurrence of distinct global scaling exponents and the associated correlations are mainly due to the presence of serial auto-correlations present in the original data and not due to the broad probability distribution.

---

[2] Original data when shuffled, becomes uncorrelated random noise.

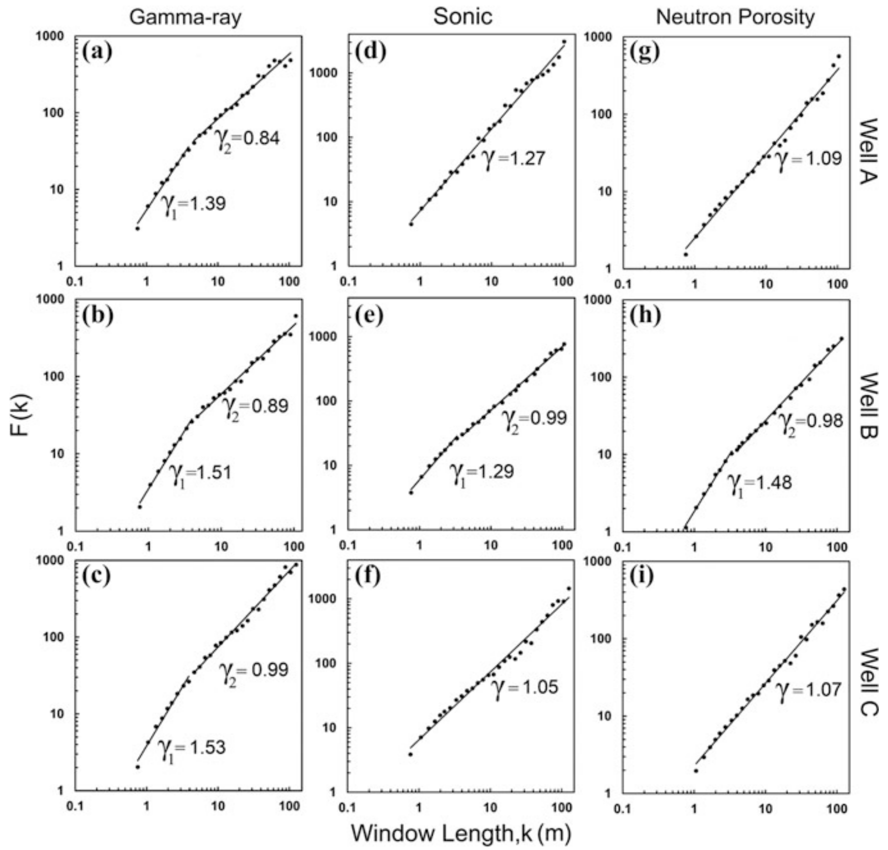

Fig. 4 Double logarithmic plot depicting the linear correlation between the average fluctuations, $F(k)$ (see Eq. 3) and the corresponding window length, k, for all the log data sets of all the wells. γ_1 and γ_2 in **a**, **b**, **c**, **e** and **h** respectively designate global scaling exponents corresponding to the short-range and long-range correlations in the respective log data sets. γ in **d**, **f**, **g** and **i** represent the single global scaling exponent of sonic and neutron porosity logs of wells A and C

5.2 Overlapping Window Method to Determine Local Scaling Exponent

This approach is used to understand the variation of local scaling exponents as a function of depth. This helps to identify the depths to the tops of formations in the study area, by comparing with those obtained earlier by other techniques. In this approach, first a particular window size was considered and the calculated scaling exponent corresponding to that window was attributed to the centre of that window. Next the window was shifted by a unit step and the above procedure was repeated to determine the scaling exponent and attributed it to the centre of that window. This is continued till the end of the data is reached. We call the scaling exponent

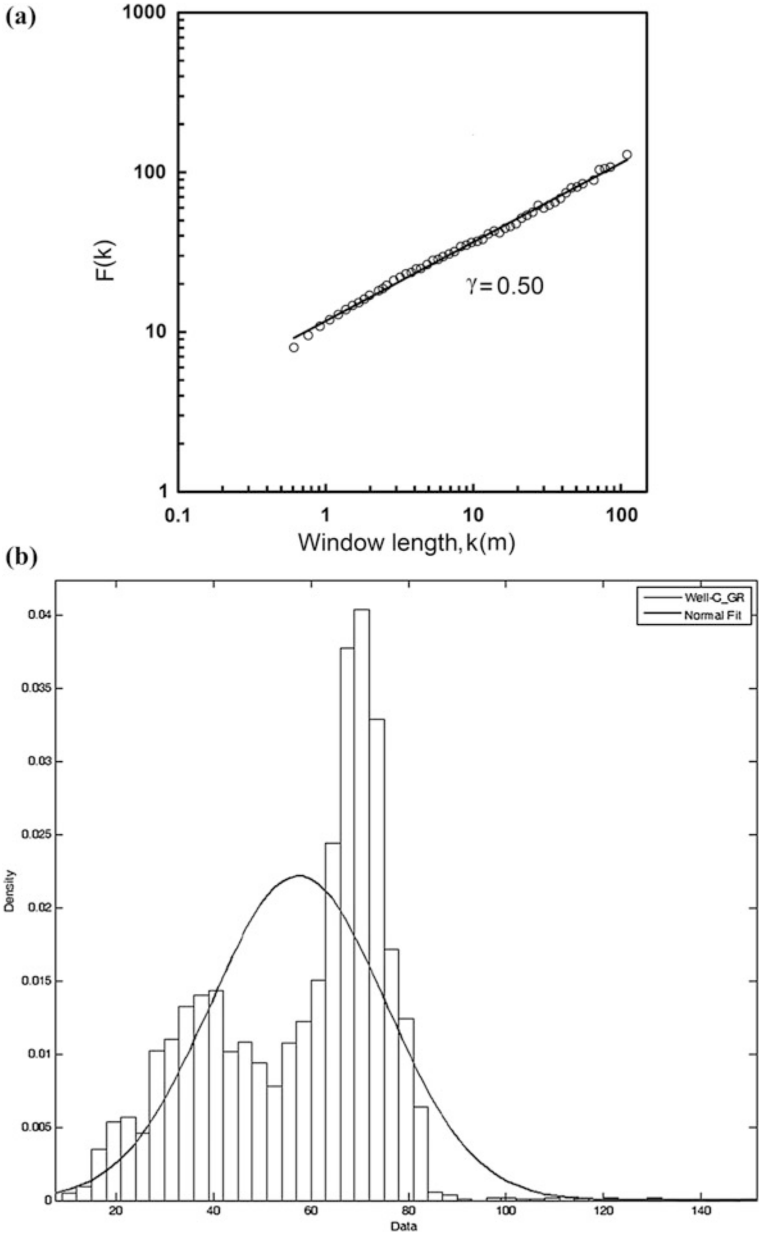

Fig. 5 **a** Global scaling exponent (γ) value determined for the shuffled gamma-ray log data of well-C. The shuffled sequence has resulted in an uncorrelated random noise, whose scaling exponent value is 0.5. **b** Probability density function and the Gaussian normal fit to the gamma-ray log of well-C. Note the absence of fat tail distribution in the data

Table 1 Comparison of the depths to the tops of formations delineated from the plots of variation of local scaling exponents as a function of depth (Figs. 6, 7 and 8) with those obtained from wavelet analysis using Gauss1 wavelet for different well-logs (Chandrasekhar and Rao 2012) Known depth estimates provided by ONGC Ltd. are also given. Note the good agreement between the observed and estimated values

Well	Reservoir top	ONGC Ltd.	Wavelet analysis (Gauss1)		DFA (present study)		
			GR	NPHI	GR	DT	NPHI
Well A	L-I	998.5	998	997	1000	996	999
	L-II	1020	1021	1022	1020	1020	1021
	S-I	1226	1225	1225	–	1228	1226
	L-III	1350	1352	1351	1352	1350	1350
Well B	L-I	980.5	983	980.2	–	980	980.5
	L-II	1006	1006	1008	1005	1008	1006
	S-I	1202	1200	1201	–	1202	1202
	L-III	1329	1329	1328	1328	–	1325
Well C	L-I	1004	1003	1004	1002	1001	1004
	L-II	1032	1031	1032	1029	1042	1032
	S-I	1195	1200	1189	–	1196	–
	L-III	1361	1361	1361	1360.3	1365	1360

thus obtained as a local scaling exponent. The entire procedure described above is repeated for different window lengths, varying in the range 16–36 m (Hernandez-Martinez et al. 2013), which corresponds to 4 to 8 times the cross-over window length of 4.0–4.5 m (cf. Sect. 5.1), depicting the boundary between short-range and long-range correlations in the signal. Figures 6, 7 and 8 show the plots of variation of local scaling exponents as a function of depth determined for all the logs of wells A, B and C, respectively, corresponding to a window length of 23 m. This window length was found to be optimum for clear identification of depths to different subsurface litho units, when compared with those of the wavelet analysis results of same data sets (Chandrasekhar and Rao 2012). Table 1 provides a comparative description of the depths to the tops of formations obtained from wavelet analysis, from ONGC Ltd. and the present study.

6 Results and Discussion

Figure 4 shows the global scaling exponents derived for gamma-ray log, sonic log and neutron porosity log of all the wells using non-overlapping windows of various sizes. The two global scaling exponents, γ_1 and γ_2, shown in Fig. 4 correspond to two different groups of window lengths varying in the ranges 0.75–4 m and 4.5–125 m, indicating short-range and long-range correlations, respectively, in the signal. Gamma-ray logs of all the wells (Fig. 4a–c) and sonic and neutron porosity

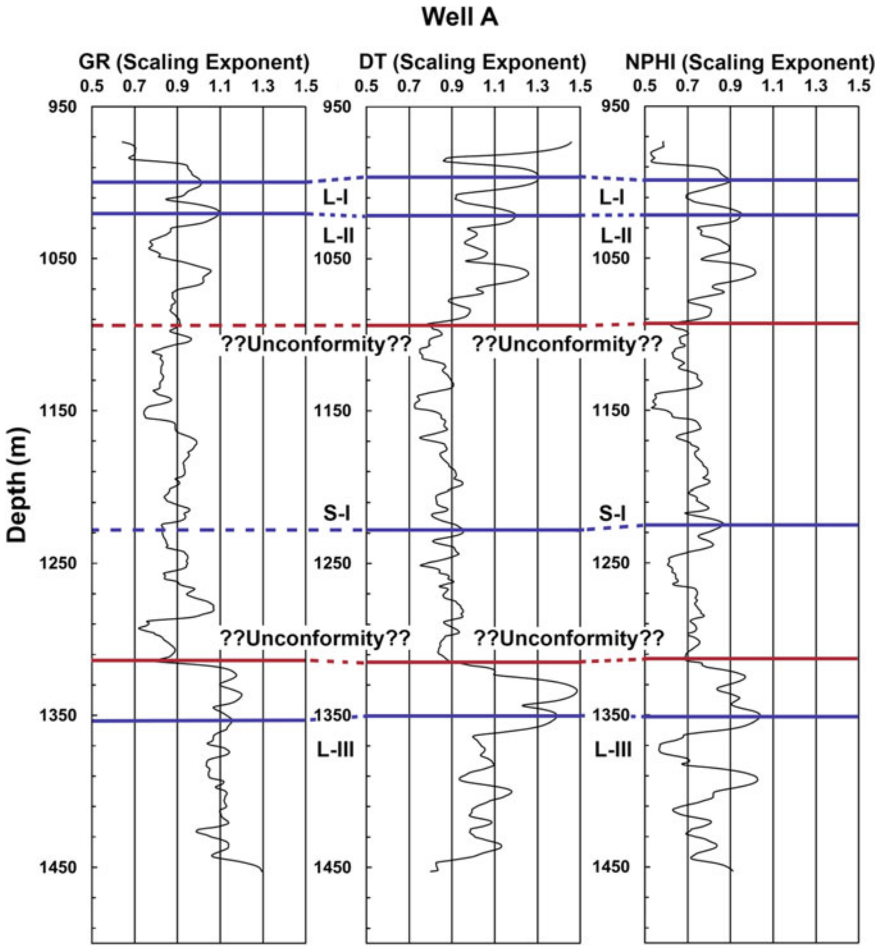

Fig. 6 Variation of local scaling exponent as a function of depth, calculated for all the data sets of Well-A using an optimum window length of 23 m. Note the clear demarcation of depths to the tops of L-I, L-II, L-III and S-I zones, identified by the DFA technique

logs of well-B (Fig. 4e, h) show two distinct global scaling exponents, γ_1 and γ_2, being greater than 1 and less than 1, respectively, indicating the presence of non-stochastic and stochastic processes in the subsurface formations (cf. Sect. 4). However, the sonic and neutron porosity logs of wells A and C (Fig. 4d, f, g, i) show a single global scaling exponent value of greater than 1, signifying the non-stochastic nature of the interval transit time (primary porosity) and porosity, respectively, in the entire data sequence.

As is well known, gamma-ray logs facilitate to understand the subsurface sedimentation patterns due to the large differences in the natural radioactivity of shaly and non-shaly formations. Thus the two distinct global scaling exponents determined for gamma-ray logs of all the wells (Fig. 4a–c) clearly demonstrate the distinct

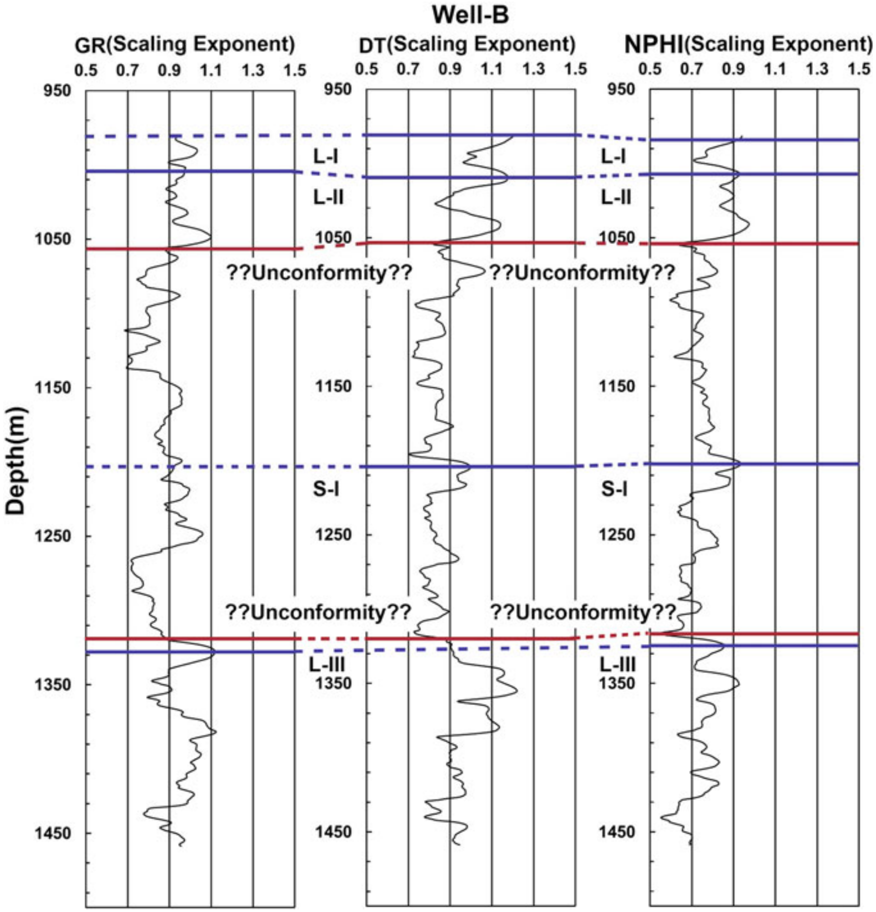

Fig. 7 Same as Fig. 6, but for Well-B

fractal behavior of sedimentation pattern, such that it appears to be non-stochastic when window lengths are small and stochastic when window lengths are large.

Sonic logs, which record the interval transit times, are mainly used to estimate the primary porosity of the formations and neutron porosity logs, which measure the hydrogen index of the formations, provide true porosity in case of limestones (Serra 1984). The single global scaling exponent values of greater than 1.0 derived for sonic and neutron porosity logs of wells A and C (Fig. 4d, f, g, i) indicate the nature of the primary porosity and the true porosity in the entire formation sequence to be non-stochastic. It is interesting to observe that the fractal behavior of both these logs does not show any significant differences in the global scaling exponents although they are obtained with different window sizes (see Fig. 4d, f, g, i). This suggests that the differences in the successive $F(k)$ values are very small and thus there is a steady increase in them with increase in window length. Usually, this

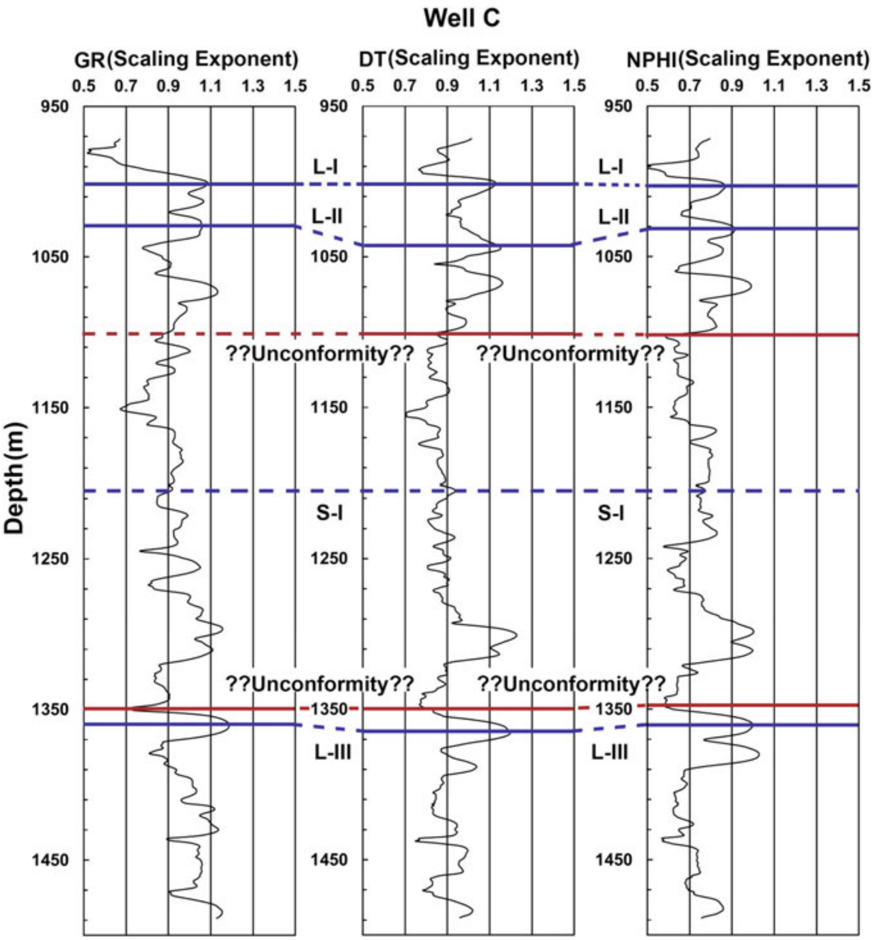

Fig. 8 Same as Fig. 6, but for Well-C

happens when there are no significant changes in the petrophysical properties of the formations within the considered depth range. Thus, the estimated global scaling exponents for both the logs of wells A and C confirm the non-stochastic trends in the primary as well as true porosity. Since the primary porosity generally decreases with depth due to compaction and diagenesis (Medina 2009), its non-stochastic trends seen in the data corroborate this observation.

In case of well-B, both sonic and neutron porosity logs, unlike in the cases of wells A and C, show two distinct trends with respect to window lengths, resulting in two distinct global scaling exponents (Fig. 4e, h). Also, in case of gamma-ray log of Well-B, the difference between γ_1 and γ_2 values of Well-B (Fig. 4b) is slightly higher than those observed for the same logs of well-A and well-C. Thus the overall subsurface nature of well-B appears to be quite different from that of wells A and C.

Perhaps, this could be due to the effect of different diagenetic conditions in well-B. However, more log data sets need to be studied from this area to further confirm this observation.

Figure 4a–c, e, h, show a change in global scaling exponents in the cross-over window length of 4.0–4.5 m, signifying the boundary between non-stochastic and stochastic behavior in the data of respective logs of all the wells. Hernandez-Martinez et al. (2013) suggest that for calculating the local scaling exponents as a function of depth using overlapping window method, the window length should be four times that of the cross-over window length. They opine that the local scaling exponents thus calculated, facilitate to demarcate the subsurface lithounits. Accordingly, various window lengths starting from 16 to 36[3] m were chosen to calculate the local scaling exponents as a function of depth for all logs of all the wells. A comparison of all such plots generated using various window sizes with the wavelet analysis results of well-log data sets of the same region (see Figs. 5–7 and Table 1 of Chandrasekhar and Rao 2012) clearly showed that the window length of 23 m is optimum to identify the depths to the tops of reservoir zones in all the wells (Figs. 6, 7 and 8). Beyond the window length of 23 m, the local scaling exponents are largely averaged out and did not provide proper resolution to identify the depths to the tops of the reservoir zones.

A careful examination of the plots of local scaling exponents obtained as a function of depth for all logs of all the wells (Figs. 6, 7 and 8) and Table 1 clearly identifies not only the depths to the tops of L-I, L-II, S-I and L-III reservoir zones, but also the probable locations of unconfirmities between L-II and L-III zones (see Fig. 1b). A careful observation of Fig. 6 shows the sudden changes in local scaling exponent values in the range 0.8–1 (between 1090 and 1320 m) to 1–1.3 (1320 m and below). These boundaries at 1090 and 1320 m clearly depict the plausible depth location of unconfirmities (see also Fig. 1b). The likely depth locations of unconfirmities in wells B and C are also shown in Figs. 7 and 8.

Limestones show low gamma-ray counts due to the absence of radioactivity. However, since L-I, L-II and L-III zones depict the limestone-shale boundaries, the variation of local scaling exponents of gamma-ray log with depth corresponding to these boundaries indicates positive high (Figs. 6, 7 and 8), due to increase in the $F(k)$ values as the window approaches the shale boundary. Similarly, in case of sonic log since the interval transit time is low in limestone reservoirs and is high in shales, the limestone–shale boundaries marked by positive high local scaling exponents could be easily identified (Figs. 6, 7 and 8). In case of neutron porosity log, the hydrogen index is high in shales due to the presence of bound water compared to hydrocarbon-bearing limestones. Accordingly, the local scaling exponents show positive high value at the limestone-shale boundaries as a function of depth (Figs. 6, 7 and 8).

In case of S-I (the boundary depicting the sand and shale) gas-bearing zone, since the gamma-ray log shows gradational changes due to mixture of sand and shale, the identification of such boundary became difficult by the DFA method, as

---

[3] This maximum window length corresponds to 8 times the cross-over window length of 4.5 m.

has been the case for gamma-ray log of all the wells. In gas-bearing zones while the interval transit time as seen in sonic logs will in general be higher compared to that of non-hydrocarbon zones, the hydrogen index as measured in neutron porosity logs is generally low compared to that of non-hydrocarbon zones. Accordingly, the S-I zone could be clearly identified in wells A and B (Figs. 6 and 7). However, the S-I zone could not be clearly delineated in well-C (Fig. 8) and the reasons for this could not be ascertained in the present study.

7 Conclusions

DFA is proven to be one of the efficient mathematical techniques for studying the fractal nature of non-stationary signals like well-logs. Among the non-overlapping window method and overlapping window method employed to determine the global and local scaling exponents, the former has proven to be an efficient method to clearly distinguish the non-stochastic and stochastic trends in the physical properties of the formations and the latter to identify the depths to the tops of reservoir zones. Particularly, the distinct stochastic and non-stochastic behaviors observed in the analysed data sets could confirm the nature of the subsurface formations in well-B to be quite different from those of wells A and C. However, we feel that a study on more data sets from this region might strongly support our observation. For the first time, through this study, we have made a comparative study of wavelet analysis results with those of the present study and identified a window length of about 23 m to be optimum to demarcate the depths to the tops of reservoir zones and showed that the results obtained from the DFA technique and wavelet analysis match quite well. Further studies using wavelet-based fractal analysis and multifractal DFA, applied to various well-log data sets of diverse regions, would be worthwhile for a comprehensive understanding of the nature of the subsurface formation properties in a broader perspective.

Acknowledgements The authors express their sincere thanks to Prof. V.P. Dimri, for inviting them to write this chapter. Thanks are also due to an anonymous referee for providing meticulous review, which has improved the quality of the chapter. The authors thank ONGC for providing the requisite data used in the present study.

References

Antelo R, Andina SA, Aguirre O (2001) Permeability calculations from clustering electrofacies technique for the petrophysical evaluation in La Pena and Tundy Oil Fields. SPE 69400, SPE Latin American and Caribbean Petroleum Engineering Conference, Buenos Aires, Argentina

Anxionnaz H, Delfiner P, Delhomme JP (1990) Computer-generated core-like descriptions from open-hole logs. Am Assoc Pet Geol Bull 74:375–393

Bhandari LL, Jain SK (1984) Reservoir geology and its role in the development of the L-III reservoir, Bombay high field. Indian J Pet Geol 7:27–46

Chandrasekhar E, Dimri VP (2013) Introduction to wavelets and fractals. In: Chandrasekhar E, Dimri VP, Gadre VM (eds) Wavelets and fractals in Earth system sciences. CRC Press, Taylor and Francis Group, UK, pp 1–27

Chandrasekhar E, Rao VE (2012) Wavelet analysis of geophysical well-log data of Bombay offshore basin, India. Math Geosci 44(8):901–928

Hernandez-Martinez E, Velasco-Hernandez JX, Perez-Muñoza T, Alvarez-Ramirez J (2013) A DFA approach in well-logs for the identification of facies associations. Phys A 392:6015–6024

Goldberger AL, Amaral LAN, Glass L, Hausdorff JM, Ivanov PCh, Mark RG, Mietus JE, Moody GB, Peng C-K, Stanley HE (2000) PhysioBank, PhysioToolkit, and PhysioNet: components of a new research resource for complex physiologic signals. Circulation 101(23):e215–e220 [Circulation Electronic Pages, http://circ.ahajournals.org/cgi/content/full/101/23/e215]

Jansen FE, Kelkar M (1997) Application of wavelets to production data in describing inter-well relationships. Society of Petroleum Engineers # 38876: annual technical conference and exhibition, San Antonio, TX, Oct 5–8

Jennings JW, Ruppel SC, Ward WB (2000) Geostatistical analysis of permeability data and modeling of fluid-flow effects in carbonate outcrops. SPE Reserv Eval Eng 3:292–303

Kantelhardt JW, Zschiegner SA, Koscielny-Bunde E, Bunde A, Havlin S, Stanley HE (2002) Multifractal detrended fluctuation analysis of nonstationary time series. arXiv: physics/0202070v1, pp 1–9 (preprint)

Khue PN, Housby O, Saucier A, Muller J (2002) Application of generalized multifractal analysis for characterization of geological formations. J Phys: Condens Matter 14(9):2347–2352. doi:10.1088/0953-8984/14/9/323

Kumar B, Kishore M (2006) Electrofacies classification—a critical approach. In: Proceedings of the 6th international conference and exposition on petroleum geophysics, Society of Petroleum Geophysicists (SPG), Kolkata, India, pp 822–825

Lee SH, Datta-Gupta A (1999) Electrofacies characterization and permeability predictions in carbonate reservoirs: role of multivariate analysis and nonparametric regression. SPE 56658, annual technical conference and exhibition held in Houston, Texas

Lim J, Kang JM, Kim J (1999) Inter-well log correlation using artificial intelligence approach and multivariate statistical analysis. SPE 54362, SPE Asia Pacific oil and gas conference and exhibition, Jakarta, Indonesia

Lopez M, Aldana M (2007) Facies recognition using wavelet based fractal analysis and waveform classifier at the Oritupano-A field, Venezuela. Nonlinear Processes Geophys 14:325–335

Medina CR (2009) Carbon dioxide storage capacity in the Upper Cambrian basal sandstone of the Midwest Region: a county-based analysis. In: Proceedings of the AAPG Eastern section meeting, Evansville, Indiana, 20–22 Sept 2009

Panda MN, Mosher CC, Chopra AK (2000) Application of wavelet transforms to reservoir—data analysis and scaling. SPE J 5:92–101

Peng C-K, Buldyrev SV, Simons M, Stanley HE, Goldberger AL (1994) Mosaic organization of DNA nucleotides. Phys Rev E 49:1685–1689

Peng C-K, Hausdorff JM, Goldberger AL (2000) Fractal mechanisms in neural control: human heartbeat and gait dynamics in health and disease. In: Walleczek J (ed) Self-organized biological dynamics and nonlinear control. Cambridge University Press, Cambridge

Prokoph A, Agterberg FP (2000) Wavelet analysis of well-logging data from oil source rock, Egret Member offshore eastern Canada. Am Assoc Pet Geol Bull 84:1617–1632

Serra O (1984) Fundamentals of well log interpretation. Elsevier, Amsterdam

Serra O, Abbott HT (1980) The contribution of logging data to sedimentology and stratigraphy. In: SPE 9270, 55th annual fall technical conference and exhibition, Dallas, Texas, 19 p

Tiwari RK (1987) Higher order eccentricity cycles of the late and mid Miocene climatic variations. Nature, 327:219–221

Vega NR (2003) Reservoir characterization using wavelet transforms. PhD dissertation, Texas A&M University, USA

Wolff M, Pelissier-Combescure J (1982) FACI-OLOG—automatic electrofacies determination. Transactions of the SPWLA 23rd annual logging symposium, paper FF, 22 p

Fractal Characters of Porous Media and Flow Analysis

Pallavi Banerjee Chattopadhyay and Nimisha Vedanti

Abstract Porosity is a complex multivariate function which controls fluid flow through porous media. The variables essentially are the characteristics of pore structures such as type, size, shape and arrangement of pores; pore space connections; area of pores that is open for flow; tortuosity of the flow paths and composition of pores, etc. Predicting the rate of flow and the flow patterns of fluid in bulk geological formation is very important for many environmental problems and oil industry. Fracture networks are secondary porosity that is known to exist within the subsurface geology that is expected to influence the flow through geological heterogeneous irregular porous media. Many of them are relevant to the migration and entrapment of fluids within the reservoir. It shows the nature of symmetry in geological formation. However, no general framework exists to systematically study the fluid flow through the fractured subsurface geometry which is complex in nature. Since direct measurements of flow through complex permeable media are time consuming and require experiments that are not always feasible, an analytical model could be more useful. Therefore, the focus of this chapter is on the development of simple analytical models based on medium structural characteristics to explain the flow in natural fractures. The pattern of fracture heterogeneity in reservoir scale of natural geological formations can be viewed as spatially distributed self-similar tree structures. Application of fractal geometry is useful to define the porous structure, where fractal geometry is the study of mathematical shapes which display self-similar, meandering and tortuous porous media details. Based on the above understanding, a fractal model of continuum percolation is presented here, which quantitatively reproduces the flow path geometry by applying Poiseuille's equation, where flow in fractures is driven by the pressure differences at the two ends of the path.

P.B. Chattopadhyay (✉)
Department of Earth Sciences, Indian Institute of Technology Roorkee,
Roorkee 247667, Uttarakhand, India
e-mail: vns_pal@yahoo.co.in

N. Vedanti
CSIR-National Geophysical Research Institute, Hyderabad,
Telangana 500007, India
e-mail: nimisha@ngri.res.in

V.P. Dimri (ed.), *Fractal Solutions for Understanding Complex Systems in Earth Sciences*, Springer Earth System Sciences,
DOI 10.1007/978-3-319-24675-8_5

1 Introduction

Interaction between fluids and pore structures delineates the fluid motion in porous media. Therefore, structure of fractures within the geological formations and its role in fluid flow is an important topic of research. Naturally fractured porous media are frequently encountered in subsurface geological formations that include groundwater, hydrocarbon and geothermal reservoirs (Moench 1984; Chang 1993). Matrix (primary porous formation) usually has low permeability and high storability, while fractures have high permeability but low storability. This implies that flow through the formations is highly dependent on the distribution pattern of fractures and their interaction. Many researchers (Barenblatt et al. 1960; Warren and Root 1963) have used double porosity concept in reservoir simulation where two different partial differential equations define matrix and fractures flow. Various researchers (Ueda et al. 1989; Lim and Aziz 1995; Sarma and Aziz 2006) have attempted to improve the basic flow equation by using various approaches that account for fracture flow with practical importance. Predicting flow through a fractured rock is one of the most challenging and difficult problems. In large systems such as reservoirs, it is challenging to obtain sufficient geometric and hydraulic information which constrain the connectivity of fracture networks and define fluid flow trajectories.

Subsurface fracture distribution is a non-linear system in nature where magnitude and direction vary in the wildest way. During the 1980s, physicists and some hydrogeologists had put in considerable amount of effort to understand the physical properties of fluid flow in fractured porous media (Sen et al. 1981; Krohn and Thompson 1986). Petroleum engineers and hydrologists generally deal with consolidated fractured rocks where the conceptual structure of the medium is critical for estimation. Probably the most striking aspect of naturally fractured porous media is the complexity in texture. Fracture sets typically occur as groups of tens to thousands of individual fractures in reservoirs and obtaining a useful and valid description of the media is the fundamental difficulty in estimating flow and transport properties. It is a common practice to narrow down the complexity by largely ignoring the geometrical complications and many researchers (Sudicky and McLaren 1992; Bogdanov et al. 2003; Helmke et al. 2005) have represented such matrix as a discrete fractured network to focus on the core problem at hand. The most important reason for modelling fractures discretely is to represent the connectivity of flow paths in the subsurface using a geologically realistic and simple heterogeneous representation. The study of discrete fracture networks is more important in systems where fractures are large and sparse compared to the scale of reservoir and in locations where fracture geometry can be characterized. However, such characterization may be limited to the large spatial extent of a reservoir. Commonly fractures are developed in consolidated rocks, where the fractured medium forms a preferential flow path over the primary porous path. Fractures control fluid flow in the geological settings which are anisotropic and heterogeneous systems, characterized by a network of fractures spread over various regions of porous matrix in a large-scale reservoir.

Katz and Thompson (1985) noticed that most of the porous media are fractals, where steady-state crystal growth during rock formation is a plausible cause for the self-similar geometry. Jacquin and Adler (1987) performed an extensive series of numerical simulations and the results show that the permeability of the porous media can be approximated by a power-law function of the porosity. Prediction of fluid flow through complex fractured systems as fractures spread over a wide range of scales is very complicated (Barton et al. 1983; Brown 1989) and a traditional approach cannot demonstrate quantitative characteristics at reservoir scale. Many conventional models of fracture networks have been developed as a planar system, whereas natural fractures are not generally planar (Gertsch 1995). Many researchers (Mandelbrot 1982) have represented fractures as a finite line segment. However, the effect of internal surface roughness of the fractures is not considered in most of the fracture flow models. Snow (1969) proposed the simplest model of planar fracture that is the space between two parallel and infinite flat planes. First, Wang et al. (1988) used fractal geometry to overcome this difficulty. He proposed a fractal model of fractures which considered the aperture corrections. Reservoir scale fracture distributions commonly exhibit similar features at different resolutions (Fig. 1).

Most of the porous media models are based on single pores, however averages are performed over a pore-size distribution without considering the effects of connectivity (Kozeny 1927; Carman 1956; Mualem 1976). More complicated averaging schemes, such as Burdine's (1953), which uses a joint probability distribution rather than a single probability, diminish the connectivity of the large and wide pores in an area.

Thus, interest of the present study is to explore the fluid flow behavior within a fractured geo-fluid reservoir. Multiscale fault and fracture networks represent the most relevant features allowing geo-fluid migration within reservoir scale subsurface structures. In fractured reservoirs, the largest faults are usually detected by seismic survey and smaller faults are captured by well logging. However, field survey can only provide very limited information about fracture clustering and connectivity, which are all together responsible for flow properties. Therefore, reservoir scale study demands realistic flow models.

Fig. 1 Fractal geometry can relate the fracture distribution at one scale to other (Martin et al. 1998)

Dimri et al. (2012) provide the fundamentals of fractal applications in reservoir geophysics and reservoir simulation study. Reservoir scale fracture distribution is a self-organized process on geological time scale (Bak et al. 1987; Cowie et al. 1993). Natural fracture networks show a power-law distribution (Walsh and Watterson 1992; Cowie et al. 1995). Natural display of fracture distribution within a reservoir shows fractal-like property. In the general sense, fractal objects show the properties of being nearly the same at every progressive scale. However, in mathematical definition, no natural object is purely a fractal, instead it can be called as an 'approximate fractal' or 'statistical fractal' that displays 'self-similarity' and 'self-affinity' over extended but finite scale of ranges (Bovill 1996). Fracture distribution in reservoir scale is a fractal geometry that is self-similar in pattern and highly irregular that can be compared with trees with their branches (Fig. 2).

While proper attention is drawn towards the fractal geometry and fractal dimension, analysis of flow through the geometry is neglected. Fractal model, substituting a complex fractured porous media with a network of interconnected pores, is a powerful numerical method for flow modelling in porous materials. The model is accepted because fractal geometry is developed to describe irregular natural shapes and to quantify the scaling properties of fracture networks.

Fig. 2 Fluid flow through saturated pore throats

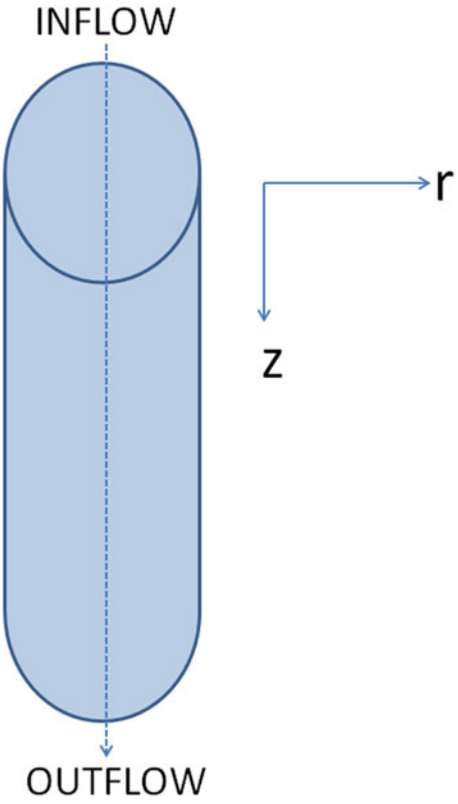

2 Fluid Flow Through Fractal Geometry

The fluid flow equations for fractured system are very complicated as the flow depends on viscosity of the fluid and the diameter of the fractured path. The assumption of constant fluid viscosity in the fractured geometry is necessary to simplify the flow as a near Newtonian fluid. However, walls in a naturally fractured system are irregular and can change their diameter, which can affect fluid flow in the media. It is assumed that the fractures have constant diameter for small segment, which is necessary for application of hydrodynamic equations and analytical calculation of the model.

Turbulent flow is possible in large diameter fractures. When the fluid moves slowly, without much mixing between the layers the flow estimation then assumes laminar flow for the entire system. Assumption of laminar flow is valid for small diameter fractures, distributed in a large area. Such flows are mainly quantified by Darcy’s formula. However, Darcy’s equation has serious limitations for fractured laminar flow, but it gives the correct result for creeping filter flow through relatively long, uniform and isotropic porous media of sand or unconsolidated formations. Therefore, Darcy’s law is not suitable for fractured media flow, which has complicated topology embedded in three dimensions. Three dimensions of fractured media are obtained through stereo projection, which may not be always simple.

Similar to Darcy’s law, Poiseuille’s law is based on the experiment of flow, but flows are through small diameter pipes. The proposed flow equations by Darcy (Hagen 1839) and (Poiseuille 1840) are based on geometric differences between a sand column and small diameter pipes, respectively, for laminar flow. The fracture flow is assumed to be laminar through entire capillary size fractal geometry. The most important feature of a fractal object is its “degree of irregularity”. The degree of irregularity (*D*) in fractal geometry allows us to quantify the roughness and irregularity of a shape in numerical value. Researchers (e.g. Katz and Thompson 1985; Turcotte 1970; Bayles et al. 1989) suggest that, in a given length scale range, natural porous media can be described as a fractal of dimension *D*.

2.1 Porosity and Fractal Media

The fractal fragmentation model of Turcotte (1986) added legitimacy to the study of fractal models of porous media, particularly soils, because it developed a mechanism by which scale-independent fracture properties could form a fractal distribution of particles. As an extension, Rieu and Sposito (1991) then developed a model, named as the Rieu and Sposito (RS) model, based on fractal pore space to predict pressure–saturation curves from particle-size data. In the model, d_m and r_m denote the maximum pore diameter and radius, and d_0 and r_0 the smallest diameter and radius. The reason for their choice is that they can use an index i, representing the iteration from ‘m’ number to 0 of the fractal process.

For simplicity, V_i represents the total volume in all pore sizes greater than d_m and less than or equal to d_i. There is a constant ratio N of the number of pores of diameter $d_{i+1} = qd_i$ to the number of pores of diameter d_i. Here, q is the ratio of pore diameters in successive classes and is less than 1. Define the partial volume $P_i \equiv V_i - V_{i+1}$, the total volume as V_0 and the volume of the solid material as V_m.

$$V_{0=} \sum_{i=0}^{m} NV_{i+1} + P_i \tag{2.1.1.1}$$

Here, pores smaller than d_m can be ignored; that is, if we could resolve smaller pores, the iteration would proceed further. The total pore volume, V_p, can be written as:

$$V_\mathrm{p} = P_0 \frac{1 - (Nq^3)^m}{1 - Nq^3} \tag{2.1.1.2}$$

One can express the porosity and substituting the P_0 value ($P_0 = V_0\,(1 - Nq^3)$) to find:

$$\phi = 1 - (Nq^3)^m \tag{2.1.1.3}$$

The numerical factor q_m, however, is nothing more than the ratio of the smallest pore diameter to the largest, d_m/d_0, so that fractal dimensionality:

$$D = \frac{\log N}{\log \frac{1}{q}} = 3 - \frac{\log(1 - \phi)}{\log\left(\frac{d_\mathrm{m}}{d_0}\right)} = 1 - \left(\frac{d_\mathrm{m}}{d_0}\right)^{3-D} \tag{2.1.1.4}$$

The above equation relation establishes the RS result for the porosity. The power-law distribution of pore sizes is bound by a maximum radius r_m and truncated at the minimum radius r_0. Knowledge of φ, r_0 and r_m is sufficient to explain dimension (D) explicitly.

2.2 Poiseuille's Equation: Simplified Navier–Stokes Equations

The scaling behaviors are generally attributed to medium heterogeneity (Schulze-Makuch and Cherkauer 1997; Carrera 1993). The parameters for fracture geometry are functions of the scale, where different scales could be considered according to the specific problem (i.e. commonly oil fields are regional scale problems). The regional scale fracture distribution supports self-similar assumption, very similar to the tree shape fractal model (Rovey 1994). In fractured framework, the porosity, which could be considered as the small diameter tube with tortuosity, plays a fundamental role with regard to the water flow in the porous medium. Flow occurs from locations with high potential energy to locations of lower potential energy in pursuit of equilibrium state. The driving force for flow is called potential gradient, the difference in potentials between two points in a system separated by a certain distance '*L*'. In Eq. 1, *i* is the potential gradient and Ψ_1 and Ψ_2 are potential energies at inlet and outlet, respectively.

$$i = -\left(\frac{\Psi_1 - \Psi_2}{L}\right) \tag{2.1.2.1}$$

The gradient is developed due to differences in pressure, position in gravity field, chemical concentration, temperature and position in electrical field, which leads to spontaneous flow of mass or energy.

A Newtonian viscous fluid of constant density is shown to be in steady motion down a cylindrical tube of radius of *R* (Fig. 2). The pressure gradient should be down the tube and velocity profile is parabolic, because of viscous stresses at the walls of the tube. The flow is considered to be steady and laminar of Newtonian fluid with constant viscosity through a small diameter of cylindrical tube similar to fractured segment. For such a model Navier–Stokes equations are simplified to Poiseuille's equation:

The Navier–Stokes equation in the coordinate is given as:

$$\frac{\partial u_z}{\partial t} + u \cdot \nabla u_z + \frac{1}{\rho}\frac{\partial p}{\partial z} = v\nabla^2 u_z, \tag{2.1.2.2}$$

$$\frac{\partial u_r}{\partial t} + u \cdot \nabla u_r - \frac{u_\theta^2}{r} + \frac{1}{\rho}\frac{\partial p}{\partial r} = v\left(Ku_r - \frac{2}{r^2}\frac{\partial u_\theta}{\partial \theta}\right) \tag{2.1.2.3}$$

$$\frac{\partial u_\theta}{\partial t} + u \cdot \nabla u_\theta - \frac{u_r u_\theta}{r} + \frac{1}{r\rho}\frac{\partial p}{\partial \theta} = v\left(Ku_\theta - \frac{2}{r^2}\frac{\partial u_r}{\partial \theta}\right) \tag{2.1.2.4}$$

$$\frac{\partial u_z}{\partial z} + \frac{1}{r}\frac{\partial r u_r}{\partial r} + \frac{1}{r}\frac{\partial u_\theta}{\partial \theta} = 0 \tag{2.1.2.5}$$

Here, in Eqs. (2.1.2.3) and (2.1.2.4), $K = \nabla^2 - \frac{1}{r^2}$ and $u \cdot \nabla = u_z \frac{\partial}{\partial z} + u_r \frac{\partial}{\partial r} + \frac{u_\theta}{r}\frac{\partial}{\partial \theta}$. It is assumed that the axis of the tube is the *z*-axis, *r* is the radial variable and $u = (u_z, u_r, u_\Theta) = (u_z(r), 0, 0)$ is the velocity field in cylindrical polar coordinates.

Consider a steady laminar flow of Newtonian fluid with constant viscosity through a horizontal cylindrical rigid tube (fracture segment). For such a model, Navier–Stokes equations are simplified to Poiseuille's equation.

$$Q = \frac{\pi r^4 \Delta p}{8\mu L} \tag{2.1.2.6}$$

Poiseuille's law relates to the fluid flow Q [ml/s] through a fracture segment with the difference in fluid pressure Δp at the two ends of segment. Segment radius is represented by r, length is L and viscosity is μ of the fluid.

The most effective factor controlling flow is radius of the segment. High pressure can be caused by narrowing segment and is reduced by increasing the fracture radius. During laminar fluid flow, cylindrical liquid in segment is exposed to internal friction, which represents the resistance of flow R.

$$R = \frac{8\mu L}{\pi r^4} \tag{2.1.2.7}$$

The resistance of fluid motion through fractured segment is most strongly dependent on radius, with the fourth power relationship. Because of fluid friction, the velocity of fluid within the fractured segment varies from none in wall proximity to maximum value in the centre of the vessel creating a parabolic velocity profile. Average velocity (V_a) with respect to cross-section is determined by (Fig. 3)

$$V_a = \frac{\Delta p \times r^2}{8\mu \times L} \tag{2.1.2.8}$$

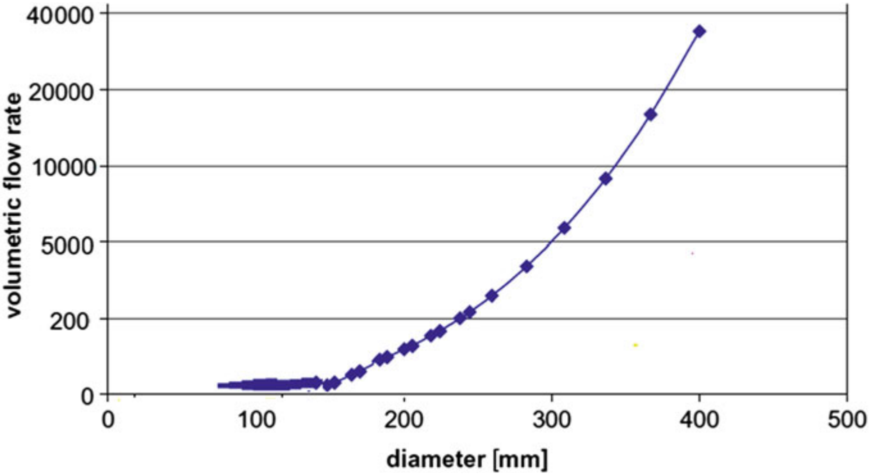

Fig. 3 Flow rates, derived by power law for geological fractured media, are plotted against average diameter of the fractures segment

3 Concluding Remarks

It is essential to be able to predict the rates of flow and the flow patterns of fluids in bulk rock during recovery of oil, or for the isolation of nuclear or toxic wastes. However, it is challenging to define average flow properties of fractured networks. In this chapter, multiscale nature of fracture networks distribution and the consequences of flow property are discussed. The fracture length distribution could reasonably be modelled by a power law whose exponent quantifies the scaling nature of fracture networks. The fact that fractures exist at all scales, from microcracks to pluri-kilometric faults, is a challenging issue for defining average flow properties of fracture networks. The fracture distribution in reservoir scale is reasonably modelled by a power law whose exponent quantifies the scaling nature of fracture networks. It has been measured that three-dimensional fracture outcrops with values ranging from 2 to 3. The transmissivity distribution is much lesser known because of the difficulty in measuring transmissivity in complex hydrogeological sites. Log-normal functions or power laws are classically used as transmissivity distribution models, but this has to be taken as a conjecture. The flow model is highly dependent on the scaling property of fracture networks and more specifically on the power-law length exponent. The two end-member models are the percolation-like model, where all fractures have a length much smaller than the system size. The probability of occurrence of large fractures (i.e. larger than the studied system) increases with scale, as such systems are always connected above a critical connecting scale that is ignored in this chapter. Permeability, as well as other flow properties, is closely related to the flow structure, which can be characterized by length scales, which depend on the fracture distribution and on the transmissivity distribution per fracture. Here, in the proposed models of fractal, tree-shaped distribution of fractures is accepted for large reservoir scale distribution. It has been scaled in such a way that the principal statistical characteristics are quantitatively comparable with measurements of real fractures. Possible simplification and generalizations assumed for a flow model for defined asymmetrical tree-like distribution have been discussed. Proposed approach enables straightforward analytical evaluation of flow parameters, which usually involves very sophisticated numerical computational methods especially for such complicated phenomena and fracture flow in general.

Acknowledgements The authors express their sincere thanks to Prof. V.P. Dimri, for his kind guidance, motivation and encouragement throughout the work. He is our mentor who taught us about this field and application of fractals in earth sciences. We are thankful to our respective institutes for all kind of research supports.

References

Bak P, Tang C, Wiesenfeld K (1987) Self-organized criticality: an explanation of I/*f* noise. Phys Rev Lett 59: 381

Barenblatt GI, Zeltov IP, Kochina IN (1960) Basic concepts in the theory of seepage of homogeneous liquids in fissured rocks. J Appl Math Mech 24:1286–1303

Barton N, Bandis S, Bakhtar K (1983) Strength, deformation and conductivity coupling of rock joints. Int J Rock Mech Min Sci Geomech Abstr 22(3):121–140

Bayles G, Klinzing G, Chiang S (1989) Fractal mathematics applied to flow in porous systems. Part Part Syst Charact 6:168–175

Bogdanov II, Mourzenko VV, Thovert JF, Adler PM (2003) Effective permeability of fractured porous media in steady state flow. Water Resour Res 39(1):1023. doi:10.1029/2001WR000756

Bovill C (1996) Fractal geometry in architecture and design Birkhauser. Nexus Netw J 1:145–146

Brown SR (1989) Transport of fluid and electric current through a single fracture. J. Geophys Res 94(B7):9429–9438

Burdine NT (1953) Relative permeability calculations from pore-size distribution data. J Petrol Technol 5(03). SPE-225-G, http://dx.doi.org/10.2118/225-G

Carman, PC (1956) Flow of gases through porous media. Butterworths, London 58, 85

Carrera J (1993) An overview of uncertainties in modelling groundwater solute transport. J Contam Hydrol 13(1–4):23–48

Chang MM (1993) Deriving the shape factor of a fractured rock matrix. Technical report NIPER-696, (DE93000170), National Institute for Petroleum and Energy Research, Bartlesville, Oklahoma, USA. pp: 40

Cowie P, Sornette D, Vanneste C (1993) Statistical physics model of complex fault pattern organization and earthquake dynamics. J Geophys Res 98:21809–21821

Cowie PA, Sornette D, Vanneste C (1995) Multifractal scaling properties of a growing fault population. Geophys J Int 122:457–469

Dimri VP, Srivastava RP, Vedanti N (2012) Fractal models in exploration geophysics, 1st edn. Elsevier Science

Gertsch LS (1995) Three dimensional fracture network models from laboratory scale rock samples. Int J Rock Mech Min Sci Geomech Abstr 32:85–91

Hagen GHL (1839) Ueber die Bewegung des Wassers in engencylindrischenRohren. PoggendorfsAnnalen der Physik und, Chemie 16

Helmke MF, Simpkins WW, Horton R (2005) Simulating conservative tracers in fractured till under realistic timescales. Ground Water 43(6):877–889

Jacquin CG, Adler PM (1987) Fractal porous media II: geometry of porous geological structure. Transp Porous Media 2:571–596

Katz AJ, Thompson AH (1985) Fractal sandstone pores: implications for conductivity and pore formation. Phys Rev Lett 54(12):1325–1328

Kozeny J (1927) UeberKapillareLeitung des Wasssersim Boden, Sitzungsber. Adak Wiss Wien 136: 271–306 (58, 85)

Krohn CE, Thompson AH (1986) Fractal sandstone pores: automated measurements using scanning-electron-microscope images. Phys Rev B 33:6366–6374

Lim KT, Aziz K (1995) Matrix-fracture transfer shape factors for dual-porosity simulators. J Petrol Sci Eng 13:169–178

Mandelbrot BB (1982) The fractal geometry of nature. W.H. Freeman and company. New York. pp 468

Martin JT, Jonathan MBE, Patrick RA (1998) Fractal geometry in digital imaging. Academic Press, California

Moench AF (1984) Double-porosity models for a fissured groundwater reservoir with fracture skin. Water Resour Res 20(7):831–846

Mualem Y (1976) A new model for predicting the hydraulic conductivity of unsaturated porous media. Water Resour Res 12(3):513–522

Poiseuille JLM (1840) Researches experimentalessur le movement des liquids dans les tubes de trespetits diameters. ComptesRendus 11:961–967

Rieu M, Sposito G (1991) Fractal fragmentation, soil porosity, and soil water properties I. Theory Soil Sci Soc Am J 55, 58, 69, 73, 77: 1231

Rovey CW (1994) Assessing flow systems in carbonate aquifers using scale effects in hydraulic conductivity. Environ Geol 24(4):244–253

Sarma P, Aziz K (2006) New transfer functions for simulation of naturally fractured reservoirs with dual-porosity models. SPE J 11:328–340

Schulze-Makuch D, Cherkauer DS (1997) Method developed for extrapolating scale behavior. Eos, Trans Am Geophys Union 78(3):3–7

Sen PN, Scala C, Cohen MH (1981) A self-similar model for sedimentary rockswith application to the dielectric constant of fused glass beads. Geophysics 46:781–795

Snow DT (1969) Anisotropic permeability of fractured media. Water Resour Res 5:1273–1289

Sudicky EA, McLaren RG (1992) The Laplace transform Galerkin technique for large-scale simulation of mass-transport in discretely fractured porous formations. Water Resour Res 28 (2):499–514

Turcotte DL (1970) Fractals in geology and geophysics. Pure appl Geophys 131:171–196

Turcotte D (1986) Fractals and fragmentation. J Geophys Res 91:1921–1926

Ueda Y, Murata S, Watanabe Y, Funatsu K (1989) Investigation of the shape factor used in the dual-porosity reservoir simulator. In: Proceedings of the society of petroleum engineers Asia-Pacific conference, 13–15 September 1989, Sydney, Australia

Walsh JJ, Watterson J (1992) Populations of faults and fault displacements and their effects on estimates of fault related regional extension. J Struct Geol 14:701–712

Wang JSY, Narasimhan TN, Scholz CH (1988) Aperture correction of a fractal fracture. J Geophys Res 93:2216–2224

Warren JE, Root PJ (1963) The behaviour of naturally fractured reservoirs. SPE J. 3:245–255

Estimation and Application of Fractal Differential Adjacency Segregation (F-DAS) Scores in Analysis of Scanning Electron Micrograph (SEM) Imageries Towards Understanding the Adsorption unto Porous Solids

**Ashutosh Das, K. Ravikumar, B. Subramanyam, Mukesh Goel,
V. Sri Hari and G.V. Rajamanickam**

Abstract The conventional approach for fractal dimension (FD) estimation using box count method has been widely used in the analysis of imageries especially in the domain of earth systems modelling and has been known to provide insight into the complexities of the system as well as the dynamics of the processes involved. However, for heterogeneous imageries such as micrographs, etc., the information provided by estimated FD seems to be limited. The present work establishes this limitation in the use of FD (using HarFA 5.5 software) and extends the concept of fractal dimensioning into lower scale segregation levels and evaluating their differential scores. In this approach, fractal differential adjacency segregation (F-DAS) scores are estimated using MATLAB 14.0 for each of the image pixels (of SEM imageries) using the arithmetic means of the grey levels of the adjacency pixels enclosed by the box (used for counting in the conventional methods). The present analysis provides a better understanding of the variability of the system (in this case, adsorbents–adsorbate interactions), unexplored by qualitative analysis of SEM

A. Das (✉) · M. Goel
Centre for Sustainable Development, PRIST University, Thanjavur 613403,
Tamil Nadu, India
e-mail: prist.cee@gmail.com

K. Ravikumar
Department of Civil Engineering, VNR Vignana Jyothi Institute of Engineering and
Technology, Bachupally, Hyderabad 90, Telangana, India

B. Subramanyam
School of Civil Engineering, SASTRA University, Thanjavur 613402, Tamil Nadu, India

V. Sri Hari
National Institute of Construction Management and Research (NICMAR)-CISC,
Hyderabad, India

G.V. Rajamanickam
CARD, VELS University, Pallavaram, Chennai 117, Tamil Nadu, India

V.P. Dimri (ed.), *Fractal Solutions for Understanding Complex Systems in Earth Sciences*, Springer Earth System Sciences,
DOI 10.1007/978-3-319-24675-8_6

imageries as well as the functional groups using FTIR. This work provides systematic steps of estimation of F-DAS scores of any imagery, the assumptions underlying the approach as well as the scopes of its applications in analysis of various earth systems.

1 Introduction

Scanning electron microscope (SEM) has been widely used for characterization of solid materials at micro-scale and hence has been widely used to detect and analyse surface fractures, provide information on microstructures, examine surface contaminations, reveal spatial variations in chemical compositions, provide qualitative chemical analyses and identify crystalline structures and so forth. SEM is a microscope that uses electrons rather than light to form an image. There are many advantages to using the SEM instead of an ordinary microscope. The SEM has a large depth of field, which allows a large amount of the sample to be in focus at one time and produces an image that is a good representation of the three-dimensional sample. The SEM also produces images of high resolution, which means that close features can be examined at a high magnification.

The combination of higher magnification, larger depth of field, greater resolution and compositional and crystallographic information makes the SEM one of the most heavily used instruments in research areas and industries, especially in the semiconductor industry. Since the development of SEM (by Dr. Charles Oatlev in the 1950s), its area of application has been increased extensively, especially because of its ability for detailed three-dimensional and topographical imaging, ease of operation, fast analysis and availability of imageries in digital form (Joseph 2003).

However, one of the major disadvantages associated with SEM-analysis is that it provides more or less a qualitative understanding of the system, rather than a quantitative estimation. Hence, the interpretation of SEM imageries is mostly left unto the skill and experience of the interpreter. In fact, there has been a growing need for the objective and quantitative estimation assessment of SEM imageries, especially with its increasing diversity of application (Price 2005).

1.1 *Fractal Dimensions from SEM Imageries*

Of late, fractal conception of matter developed and explained by B.B. Mandelbrot in his book “Fractals Geometry of Nature” (Mandelbrot 1983) has been increasingly used to understand the self-similar and scale-independent geometry of natural structures, where fractal dimension (FD) strictly exceeds topographical dimensions.

Because of partial correlation existing among a wide range of natural systems, FDs have been used to define a wide range of biological and geological systems.

The concept of 'self-similarity of surface at different scales' is mostly used in the fractal analysis of earth sciences data (Dimri 1992). Basically the structure is characterized by single descriptor, the FD 'D'. The FD lies within the range $2 \le D \le 3$, where $D = 2$ represents a smooth surface and an increasing value of D represents an increasing surface roughness/porosity (Othman et al. 2006; Maus and Dimri 1994, 1995, 1996). The concept has been used by Dimri (2000) for studying the flow media. In fact, FD can also be correlated with various surface roughness parameters (Chauvy et al. 1998; Fang et al. 2003; Seitavuopio 2006 and Dimri 2000). Bigerelle and Iost (2003) have revealed in their studies that statistical comparison of relevant roughness parameters of FD is the most relevant parameter to describe the surface topography. The FD of a certain surface can be in principle inferred in different ways. These include, but are not limited to: scattering, adsorption of gases, impedance spectroscopy and surface image analysis. The latter two methods are especially widespread and used in different areas of research (Lasia et al. 1999 and Li et al. 2003).

Among the many methods available for analysis and description of surface topographies, the SEM and the atomic force microscopy (AFM) are widely used for surface imaging and characterization. Due to its high depth of focus, the SEM can provide detailed topographical information about the surface, but cannot provide quantitative topographical information. Such information can be obtained by fractal analysis of the images revealing the characteristic FDs (Risovic et al. 2008).

Since the surface dynamics of a solid object, caused by physico-chemical stresses, can be captured by the variability of their surface topography in SEM imageries, and such effects are largely guided by the surface characteristics of the object concerned (porosity, texture, micro-fractures, etc.), which are mostly natural, it is legitimate to explore fractal signature of surface dynamics of different materials, effected by the subjected stresses (such as sorption, reaction, activation, and so forth). In aqueous adsorbents (the solid/liquid that adsorbs the adsorbates, i.e., the liquid/gases on their surfaces) is characteristic of the microstructure of the adsorbent, which is non-homogenous and self-similar, FD may be a useful tool for characterization of the SEM imageries of the adsorbents. There have been few reports with regard to fractal applications in adsorption systems, however, the present work is taken up to access the scope of developing a characterization tool for various adsorbents, using SEM imageries (Brouers and Sotolongo 2006).

Of the various methods used in estimating the FD of an imagery, one of the most common methods is box-counting method, wherein the grey levels of the image have been computed, based on BW (black to white) boundary, B–BW (Black to BW) boundary and W–BW (White to BW) boundary. These analyses throw picture unto the fractal nature of associated phases (bright/dark) as well as their blends. The present work also carries out these analyses to estimate fractal characteristics of the imageries, using random samples to account for wide textural inhomogeneity in the original imageries itself (details in experimental). However, the FD of the images does not capture the regional variation in complexity, for studying which a novel approach has been proposed herewith, namely—fractal differential adjacency segregation (F-DAS) Scores.

2 Fractal Differential Adjacency Segregation (F-DAS) Scores—Concept and the Approach

F-DAS scores derive their basis on the estimation of FD, similar to box-counting method, but here, instead of counting the boxes, the average of the scores of the boxes is used to replace the box values. Thus, with increase in the box sizes, the scores of the boxes show changes, based on the relationship of the adjacent scores. For example, if a white pixel is surrounded by all black pixels, the average grey level of the box containing this white pixel and its adjacent pixels would be close to the score of the black pixels. In fact, the change in the value of the particular pixel, for any fixed box size, would depend on the grey levels of the pixels constituting the box, under consideration. Then, with increasing box size, the value would further be affected by the grey levels of newly added adjacent pixels. Thus, the underlying principle of box-counting strategy of conventional FD estimation would be replaced by a harmonic aggregation (to account for adjacency effect), instead of the arithmetic summation.

The standard power law for FD estimation for box-counting method, i.e. the negative of the slope between logarithm of the estimated area versus logarithm of the box dimensions used to estimate the area, was also used in this study where the slope was calculated for each pixel with regard to its change in values over the change in box sizes. Hence, the estimated negatives of the slopes form a matrix, instead of a single number, as in the case of conventional FD, thus providing a spatial understanding of the complexities associated with the image (on account of associated adjacency). Now, for an understanding of the change in the slope, the difference between slopes with first two boxes and that between second and third boxes was computed, thereby giving scope for enhanced understanding of the adjacency effect with regard to persistency of fractal estimates. The resultant matrix is named as F-DAS scores, which can be used to evaluate the estimate of persistency against the adjacency effect.

However, it is important to note that, since this approach deals with moderation of the scores based on the adjacent scores, which is non-cumulative (unlike the approach used in conventional FD estimation), these values do not obey the characteristics of FDs (i.e., non-negativity and limitation to maximum allowable dimension, i.e., less than 3 in this case, as expected to be in case of two-dimensional features like images).

In the present study, the F-DAS scores matrices were estimated using the grey levels of the various SEM-images and used for understanding the characteristics of the adsorbents (i.e., the porous solids acting as the base for adsorption in aqueous media).

3 Fundamentals of Adsorption and Relevance of Fractal Studies

Adsorption is the process of concentration of one or more contaminants (of either a gas or a liquid) on the surface of a micro-porous solid. The solid substance, which attracts pollutants, is called Adsorbent, and the pollutant concentrated at the surface of the solid is Adsorbate. Adsorption phenomena can be physical, chemical and/or biological in nature. Physical adsorption (also called, physisorption) is mainly due to van der waals forces and electrostatic forces between adsorbate molecules and atoms of adsorbent and is directly proportional to the amount of available solid surface. It takes place in one or more molecular layers, often accompanied by capillary condensation within the pores (Srihari and Das 2004). This process is relatively rapid and reversible. In fact, by lowering pressure and raising the temperature the adsorbed pollutant can be desorbed (or recovered) in many cases. The chemical adsorption (also called, chemisorption), on the other hand, involves a chemical bond between the adsorbent and the pollutant molecules (or adsorbate), held strongly to the surface of the adsorbent by vacancy forces. This process is much slower than physical adsorption because of the displacement of atoms that must occur in the molecules. Chemisorption is an irreversible and endothermic process and is usually confined to single layer of adsorbent (Srihari 2007).

Since most of the natural processes involve surface interaction between solid/liquid phase (such as mineralization of magma, formation of fogs and mists, cloud condensation, and so forth), and so also the anthropogenic processes (such as filtration, separation, coagulation, and so forth), the fractal analysis of concerned interaction is fairly justified on account of the self-similarity of these processes as well scale independence. In fact, the tagging of surface roughness has been one of the important predicaments for both, basic and applied sciences as an effect of the fact that many physical and chemical processes take place in porous environments. The conventional description of surface irregularity of porous media is based on the idea that the chaotic systems come into extensive physical and chemical properties of the ordered systems. The deviations in the perfectly ordered systems are very small. The researchers have put substantial amount of effort to study the surface phenomena analysis in the light of the fractal theory. The main aim of this hypothesis is the study of strongly disordered systems or fractal systems, because as we go to smaller or larger scales the disorder is more predominant. These systems have room for arrangement within structure and occupy inherently more space than non-disordered systems. The disorder can be described in terms of a non-integral dimension, D, which is a measure of the space-filling ability of the system (Zarzycki 1987). The fractal theory has established very successfully, both in its application to a wide variety of complex surface geometries and in advancing the understanding of how the geometry affects the physical and chemical properties of systems (Pfeifer and Avnir 1983; Pfeifer 1988). In view of the fact that the first investigation of the fractal surface properties of solids at molecular scales (Pfeifer and Avnir 1983), experimental investigations have covered a wide variety of materials with a well-defined fractal surface characteristic as determined by different techniques (Peleg et al. 1984). Among the properties sensitive to surface characteristics, the absorption of gases and vapours can be mentioned. To study the effect of the fractal surface on physical adsorption has been grouped into two: one has a topological character (Cole et al. 1986) whereas the other, according to Fripiat et al. (1986), is based on a molecular approach. Fripiat et al. (1986) and Pfeifer et al. (1989) developed a fractal isotherm equation and compared results with the isotherm derived by Cole et al. (1986). They found certain discrepancies particularly at high relative pressures. Such a discrepancy has been attributed by Pfeifer et al. (1989) to 'multiple-wall' effects, neglected in the development of the model. As Pfeifer et al. (1989) pointed out; they treat the filling of pores without considering that as a pore is being filled, the film grows from two opposite walls and stops growing when the two films meet.

However, conventional approach for estimation of FD does not show the distinctiveness of the adsorption process, nor the adsorbents (as established in this paper), rather a need for differential adjacency-based fractal analysis would be more useful to capture the signature of the regional interactions.

4 Experimental

Two distinct agro-based adsorbents, namely, black gram husk (BGH) and green gram husk (GGH), were dried, crushed, sieved and desiccated. Phenol, which is a toxic chemical, commonly found in many industrial effluents (coke-oven, leather, textile, pharmaceutical, etc.), was used as a simulated aqueous adsorbate for the study. The study was carried out at 100 ppm phenol concentration for 24 h for various adsorption dosages, and different operational conditions (pH, contact time, particle size, etc.). Only the cases with 100 % adsorption were used for SEM-analysis, with respect to both the adsorbents (i.e., before and after adsorption).

The samples collected before (BHG-B; GGH-B) and after adsorption (BGH-A; GGH-A) were used for SEM imageries. SEM-images consist of pixels where the intensity (colour) of each pixel is proportional to the number of back-scattered electrons, emitted from the corresponding point at the surface of a material. Some of them represent the corresponding points of the micro-particles (foreground pixels), others represent background. In the present study, images with 256 grey levels were used. For the extraction of the shape of particles only foreground pixels are of interest. Two distinct approaches have been adopted to study the FD of the SEM imageries.

4.1 Evaluation of Total Fractal Dimension of the Imageries

Using the SEM imageries as population, six systematic samplings were taken (equal size) so as to have better representative analysis (Figs. 1 and 2). Then, using HarFA 5.5 software (Harmonic and Fractal Image Analysis), the range analysis was carried out for each image to evaluate the threshold resolution, and then using this threshold resolution as base, the fractal analysis using box-counting method was carried out (logarithmic spectrum, mesh size: 0–35, with num steps 30). The FDs obtained for respective sub-images were studied for their normality using Shapiro–Wilk test as followed in Sect. 4.2 (and suitable comparison tests were adopted).

The Shapiro–Wilk Test (Shapiro and Wilk 1965) is a test performed to estimate the normality of a data set where the test statistics is '*W*' and null hypothesis may not be accepted, for the predefined level of significance, if *W* is less than the corresponding threshold. The test statistics *W* may defined as follows:

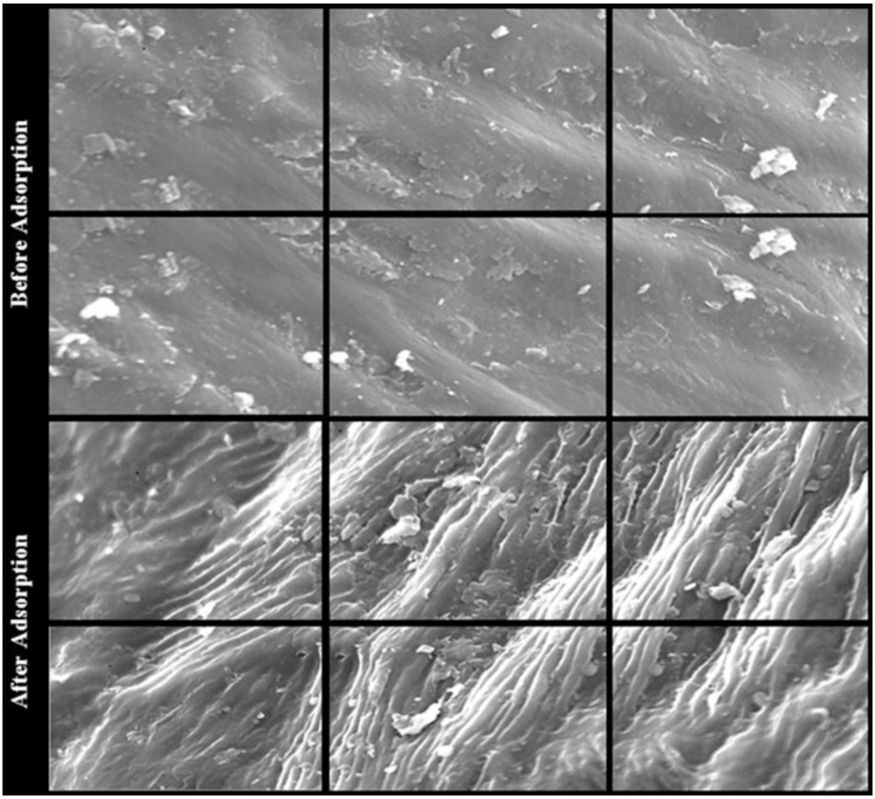

Fig. 1 Sub-images of the original SEM imageries of BGH adsorbent

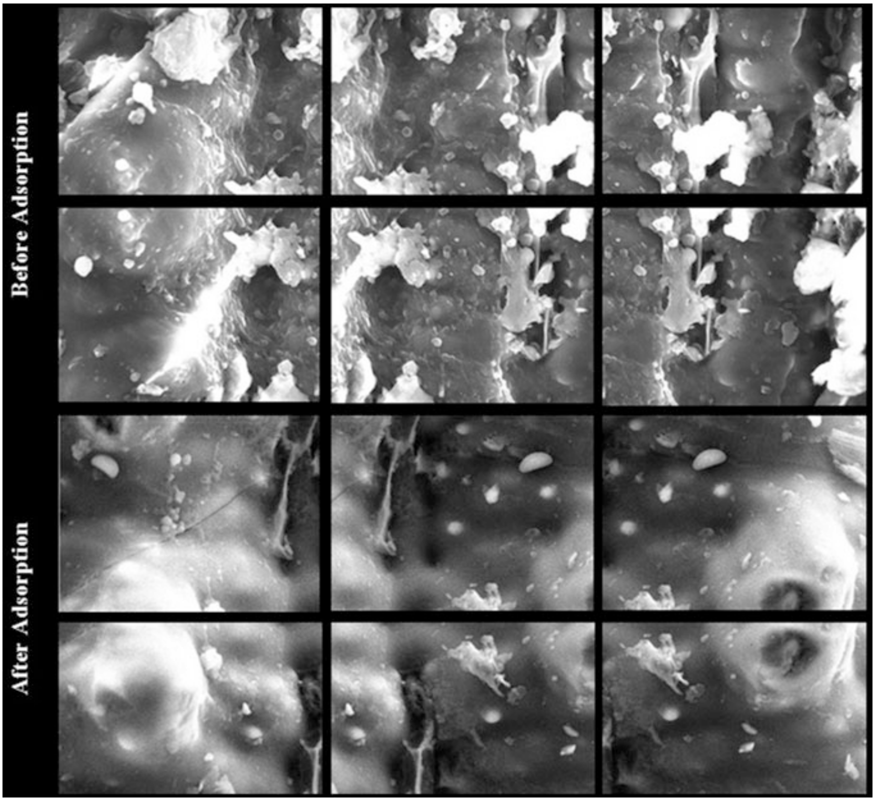

Fig. 2 Sub-images of the original SEM imageries of GGH adsorbent

$$W = \frac{\left(\sum_{i=1}^{n} a_i x_{(i)}\right)^2}{\sum_{i=1}^{n} (x_i - \bar{x})^2}$$

where the sample values (total number of samples being '*n*') are ordered from smallest to biggest with $x_{(i)}$ as the smallest value. Here, $a_{(i)}$ is defined from means and variances as follows:

$$(a_1, \ldots a_n) = \frac{m^T V^{-1}}{\left(m^T V^{-1} V^{-1} m\right)^{1/2}}$$

where $m = (m_1, \ldots m_n)^T$ and $m_1, m_2, \ldots m_n$ are means of the order statistics of sampled from the standard normal distribution and V is the covariance matrix of those order statistics.

Alpha (i.e., the level of significance) for normality has been taken to be 0.05 (i.e. the confidence interval being 95 %) and hence when the p-value (the probability for the test statistics) is less than 0.05, the null hypothesis has to be rejected (which means the data set is not normal). This test was carried out to estimate normality so that the suitable tests for the comparison of the means could be ascertained. In case, any one of the data sets used in ‘test for comparison’ is non-normal, Mann–Whitney test for two independent samples was carried out, instead of *t*-test which is restricted to only to data sets which are normally distributed. Even while carrying out *t*-test, the quality of variance of the data sets was estimated to use suitable type of the *t*-test.

4.2 Evaluation of F-DAS Scores of the Imagery

The original image was used to estimate the grey levels of the pixels, using MATLAB. For each of the original image, these matrices were computed and then used to simulate box-counting approach, wherein every 2 × 2 sub-matrices were replaced by the averages of the values of the contributing elements of the sub-matrices. The same approach was taken again by using 3 × 3 sub-matrices and 4 × 4 sub-matrices. Now using the corresponding elemental values of these matrices thus generated, the negative slope of their logarithms versus the dimensions of replaced cells, by least count method so as to evaluate the fractal adjacency scores among 2 × 2 and 3 × 3 replaced matrices as well as 3 × 3 and 4 × 4 replaced matrices. The difference between these two matrices forms the F-DAS scores. The original SEM imageries and the F-DAS scores are presented in Figs. 3 and 4.

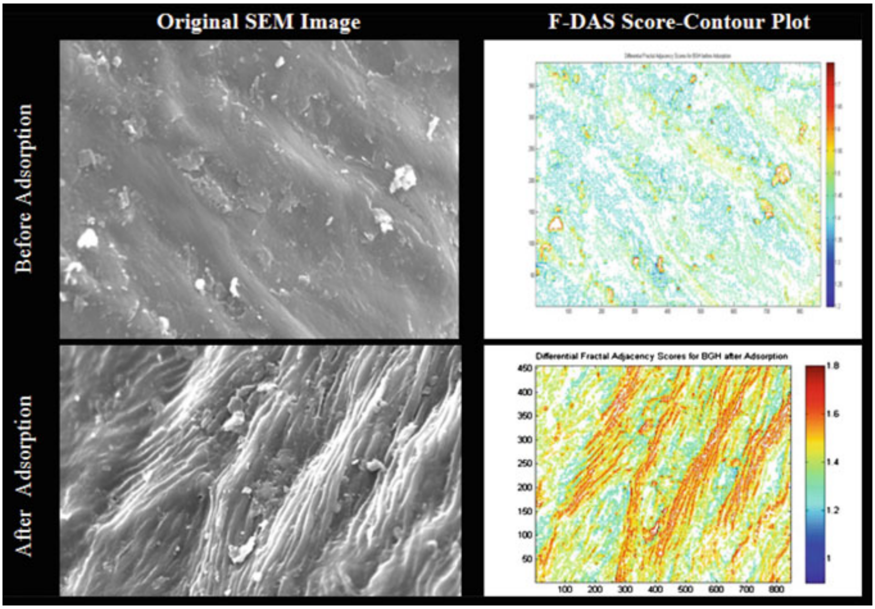

Fig. 3 F-DAS score contours plots for BGH before and after adsorption

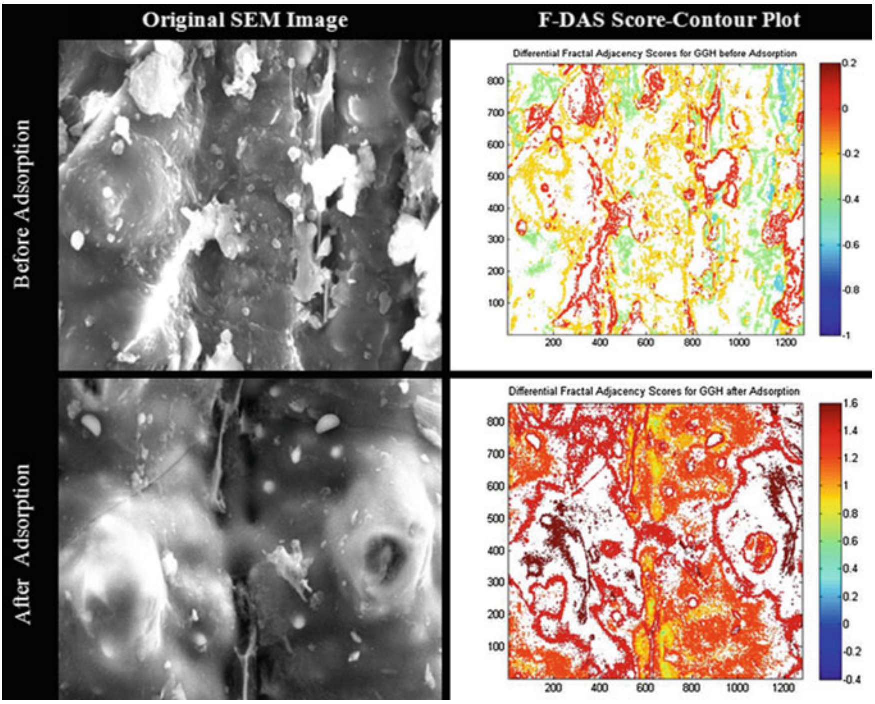

Fig. 4 F-DAS score contours plots for GGH before and after adsorption

4.3 Statistical Analysis of Fractal Dimension (FD) and F-DAS Scores

The FD scores for each of the populations (which include six sampling sub-images) were studied for their normality. Accordingly, a comparative test was carried out for each of the population types, i.e. BGH before adsorption, BGH after adsorption, GGH before adsorption and GGH after adsorption to evaluate the significant differences due to adsorption (Tables 1 and 2). With regard to F-DAS scores, summary statistics was analysed to evaluate the variation of these scores due to adsorption (Table 3).

4.4 FTIR Analysis of the Adsorbents

In order to confirm the homogeneity of the adsorbents used with regard to their functional groups and compare the changes caused by adsorptions with respect to the original adsorbents, Fourier Transform Infrared Spectroscopy (FTIR) was carried out. In fact, direct information on the presence of surface functional groups can

Table 1 Test for normality of fractal dimensions of samples of the adsorbent studied

	BGH-B	BGH-A	GGH-B	GGH-A
Shapiro–Wilk normality test (D–BW)				
W	0.965478	0.916347	0.898424	0.902966116
p-value	0.860794	0.47945	0.364696	0.391759229
Alpha	0.05	0.05	0.05	0.05
Normal	Yes	Yes	Yes	Yes
Shapiro–Wilk normality test (D–BBW)				
W	0.560907	0.884109	0.83834	0.880033791
p-value	0.00015	0.288461	0.126294	0.269212334
Alpha	0.05	0.05	0.05	0.05
Normal	No	Yes	Yes	Yes
Shapiro–Wilk normality test (D–WBW)				
W	0.911343	0.919642	0.918197	0.912255497
p-value	0.445289	0.502789	0.492473	0.45140039
Alpha	0.05	0.05	0.05	0.05
Normal	Yes	Yes	Yes	Yes

Table 2 Test for comparison between the fractal dimensions before and after adsorption for the samples

	BGH-B and BGH-A	GGH-B and GGH-A
Tests for comparison of samples (D–BW)		
Test	*t*-test (equal variance)-two-tailed	
t-critical	2.228138852	2.228138852
p-value	0.001776997	0.715393366
Significance	Yes	No
Tests for comparison of samples (D–BBW)		
Test	Mann-Whitney test for two independent samples	
U-critical	5.26002884	5.281446128
p-value	0.054663936	0.377642391
Significance	No	No
Tests for comparison of samples (D–WBW)		
Test	*t*-test (unequal variance)-two-tailed	
t-critical	2.228138852	2.364624252
p-value	0.287974327	0.056797659
Significance	No	No

be obtained from IR studies. IR spectra of adsorbents indicate the possible presence of oxygen containing groups, such as carbocyclic, quinone, ether, phenolic, and lactone, C = C of aromatic rings, and nitrogen containing groups like pyridine, nitrile, cyclic amide.

Table 3 Comparison of F-DAS scores before and after adsorption

	BGH-A	BGH-B	GGH-A	GGH-B	BGH-B > GGH-B	GGH-A > GGH-B	BGH-A > BGH-B
Mean	10	10	3.333333	3.333333	Yes	No	No
Standard error	6.896426	7.46696	1.214343	1.419497	Yes	No	No
Median	0.552263	0.071577	0.009781	0.000137	Yes	Yes	Yes
Standard deviation	21.80841	23.6126	6.651231	7.774905	Yes	No	No
Kurtosis	7.846197	8.741346	1.78292	4.074758	Yes	No	No
Skewness	2.752525	2.91509	1.845972	2.320316	Yes	No	No
Range	69.53232	75.64067	20.17078	27.73676	Yes	No	No
IQR	6.573893	6.050743	1.453284	0.352758	Yes	Yes	Yes

5 Results and Discussions

5.1 Understanding of the Adsorbents Using F-DAS Scores

The range of F-DAS for pre-adsorbed BGH is 1.2–1.75 and that of GGH is −1.1 to 0.2. The post-adsorbed range has shown a distinct increase in both the cases, i.e. 0.8–1.8 and −0.4 to 1.6, respectively, for BGH and GGH. Although it is interesting to note that the FTIR spectra of pre-adsorbed BGH and GGH are very much similar (Figs. 5, 6 and 7) with all the functional groups lower in case of BGH than GGH, yet the ranges of F-DAS Scores do show the differences, the former being entirely positive range and the latter extending over both positive and negative ranges. On observation of the plots (% counts vs. F-DAS scores range) of total counts as well

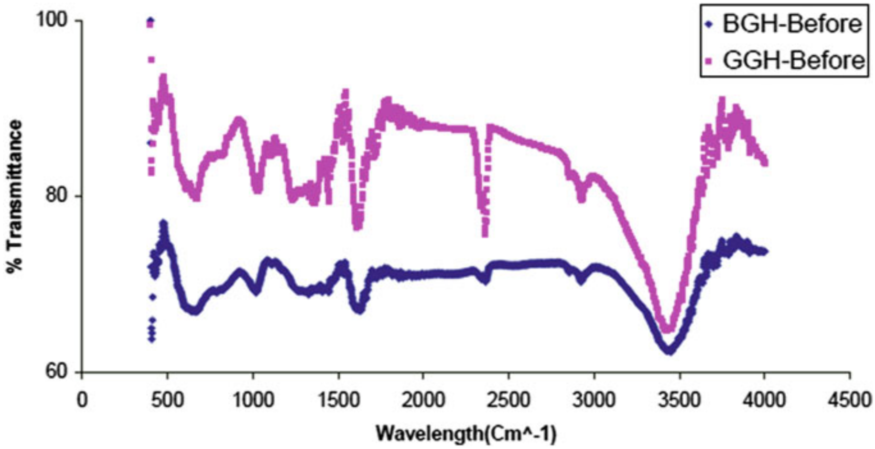

Fig. 5 FTIR spectra of BGH and GGH before adsorption

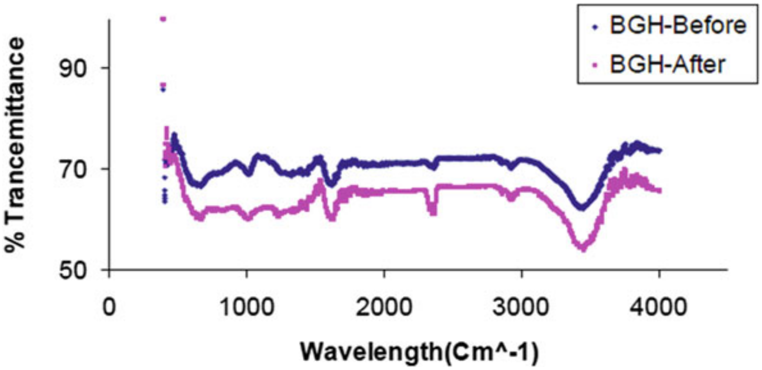

Fig. 6 FTIR spectra of BGH before and after adsorption

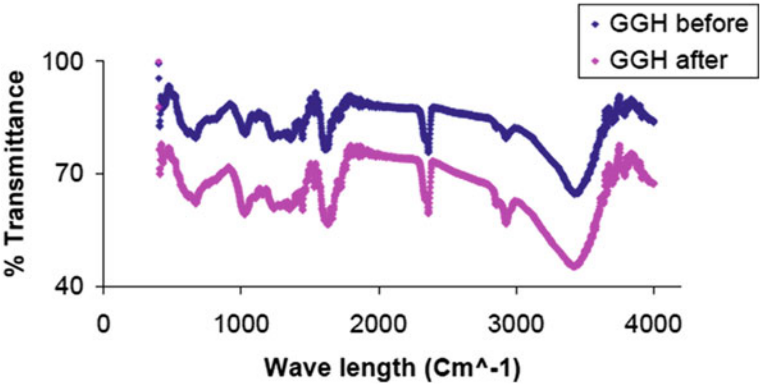

Fig. 7 FTIR spectra of GGH before and after adsorption

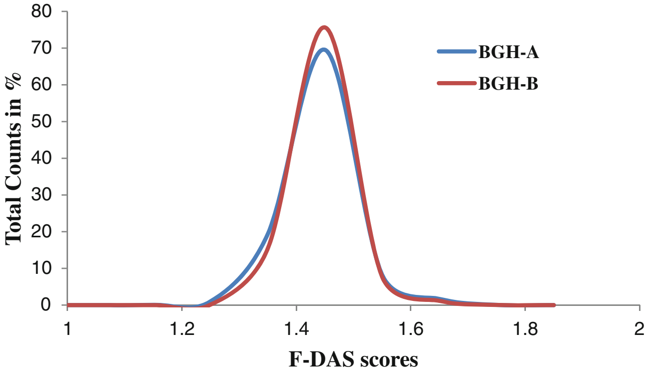

Fig. 8 Variation in total counts at different F-DAS score ranges for BGH before and after adsorption

as their cumulative values (Figs. 8, 9, 10 and 11), we see a clear differences in the plots of BGH and GGH, which is unexplored from FTIR analysis. Although both pre-adsorbed BGH and GGH are non-normal, yet the mean, standard error, median, standard deviation, kurtosis, skewness, range and Inter-Quartile Range (IQR) are higher in case of BGH compared to GGH (Table 3). Besides, the BGH showed a single distinct peak whereas GGH showed double peak distribution (primary at −0.25 and secondary at −0.05 F-DAS scores).

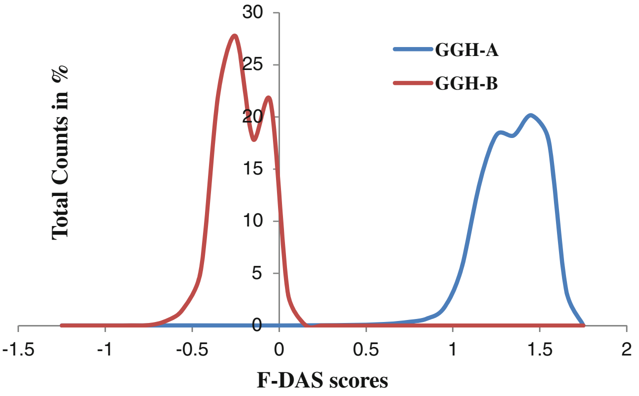

Fig. 9 Variation in total counts at different F-DAS score ranges for GGH before and after adsorption

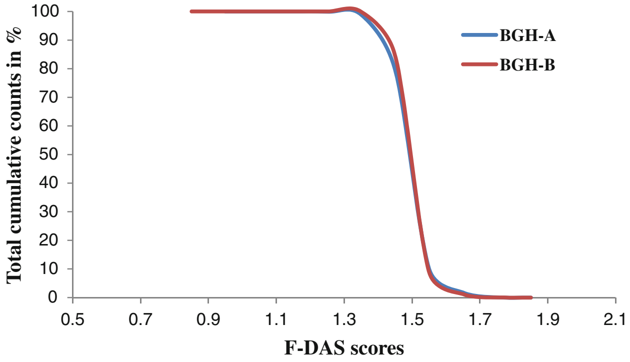

Fig. 10 Variation in total cumulative counts at different F-DAS score ranges for BGH before and after adsorption

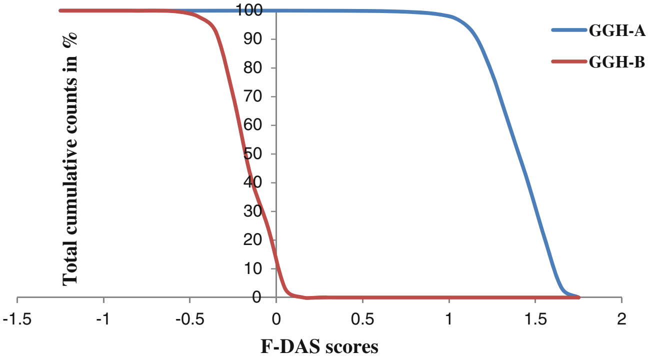

Fig. 11 Variation in total cumulative counts at different F-DAS score ranges for GGH before and after adsorption

5.2 Effect of Adsorption on F-DAS Scores

As per FTIR spectra between adsorbent before and after adsorption, we find the lowering of all the functional groups because of adsorption in case of both BGH and GGH, higher being in the latter than the former (Figs. 5, 6 and 7). However, F-DAS scores analysis gives a better understanding of this scenario (Figs. 8, 9, 10 and 11). In both the cases, there is reduction in the peak percentage of F-DAS scores, but in case of BGH it is mostly marginal without shifting the mean. However, in case of GGH, there is a distinct shift of the mean F-DAS scores from negative to positive values effected by the adsorption. The primary and secondary peaks of pre-adsorbed GGH showed the reverse trends at 1.45 and 1.25, respectively. The difference between peak values also showed the reduction by 6.2–2.0 % as a result of adsorption. When F-DAS scores were plotted against cumulative frequency percentage, we find that the BGH shows a very close distribution pattern among pre-adsorbed and post-adsorbed samples, whereas in case of GGH, the distinct shifting of distribution towards the right (higher values of F-DAS scores), although still the pattern of distribution remains similar. In both the cases, we find the very same relationship existing between pre-adsorbed and post-adsorbed statistics, namely, increase in median and IQR as well as decrease in mean, standard error, standard deviations, kurtosis, skewness and range (Table 3).

5.3 Scope and Limitations for F-DAS Scores Analysis

When compared to conventional approach for evaluation of adsorption on adsorbent, F-DAS score can enrich the understanding of the process based on FTIR analysis. In fact, the basic method of analysis of FTIR is based on the functional group present in the specimen, whereas the F-DAS scores refer to the scale-independence persistency of the visual elements of the imagery and hence they communicate two different aspects of the samples. The purpose of the work is to use the visual analysis to classify the pattern of effect of the adsorbate unto the adsorbent, which was more distinct between BGH and GGH than the FTIR analysis. In fact, as per FTIR analysis, the functional groups of these adsorbents are very much similar, whereas F-DAS scores brought out distinct difference in patterns in both the cases in the original samples and corresponding adsorbed samples. Thus, this technique can be used for better classifications of various substances even with similar chemical compositions and better understanding of the influence of stimuli (in this case, adsorption) unto them.

The F-DAS scores analysis is based on the logarithmic relationship among the parameters. And it assumes linearity among all the elements of Y matrices. If the relationships for all elements of the Y matrices are normal with regard to the corresponding element, the results are most effective. In the present analysis only four different box sizes have been utilized to estimate the difference between the slopes. However, if higher box sizes are considered, then the differences will be more distinct (i.e. it is more persistent). In case of higher number of box sizes, the normality may be assumed (as per central limit theorem) or the values may be normalized by suitable transformation. The F-DAS scores analysis carried out in the present studies referred to the original grey levels of individual pixels, which may be affected by the degrees of exposure during imaging as well as background noises. Thus an attempt to use the coefficient of variation scores (i.e. ratio of mean and standard deviation) of the image is likely to be more meaningful for F-DAS scores studies (as validated by the analysis by authors). The F-DAS scores studies may be applied to various samples from original pictures so as to get a better understanding of the adsorption phenomena to derive the estimates and standard errors at given levels of significance. Furthermore, the segregation method adopted in this study for the various pixels enclosed by the selected box size has 'arithmetic mean', which can be changed to other methods of aggregation such as 'geometry mean' or 'centroid' and so forth, which may give different (even more relevant) insights into the domain of application under concern.

6 Conclusions

As evident in the preceding paragraphs, we find a distinct advantage of F-DAS scores analysis compared to conventional fractal dimensional estimation approach (using box-counting method). In case of conventional approach, the FDs of D–BW, D–BBW and D–WBW show different distribution patterns among the samples and which are not indicative of the nature of modifications due to stimuli (in our case, adsorption). Herein, except D–BW, the other FDs (i.e. D–BBW and D–WBW) do not even show significant variations (at 0.05 level of significance), before and after adsorption. On the other hand, F-DAS scores approach provides a better understanding of surface complexities and persistency and the distribution over the range of entire spectra. Therefore, although the statistical similarity is being maintained by pre- and post-treated (here, adsorbed) samples, they do show distinct variability with regard to mean, standard error, median, standard deviation, kurtosis, skewness, range and IQR. This variability may be ascribed for specific F-DAS scores signature for different adsorbent–adsorbate systems. In fact, the various systems may be classified using F-DAS scores approach. The application of these techniques may be employed in case of various physico-chemical or biological interactions in various domains.

Here, F-DAS analysis was used as an objective analytic tool to quantitatively estimate the behavior of different materials to different responses (in this case, adsorptions) using SEM imageries. Traditionally, the SEM imageries have been used mostly by visual inspections, which are subjective and depend on the interpreters' experience. However, using F-DAS scores the researchers will not only be able to get a visual understanding of the effect of specific phenomenon/stimuli (here, adsorption) but also quantify the effects spatially as well as perceive the zones of persistency, objectively. Additionally, as mentioned in the preceding paragraph, this can also be used to classify various substances, of the similar compositions, in terms of their persistency and behavioral complexities, unexplored by conventional physico-chemical analyses.

Acknowledgements The authors express their sincere thanks to the Department of Science and Technology (DST), Government of India, for the financial support. We also thank Prof. V.P. Dimri (NGRI), for his kind motivation and encouragement throughout the development of this chapter. In fact, it is he only who taught us about this expanding field of research.

References

Bigerelle MD, Iost NA (2003) Relevance of roughness parameters for describing and modelling machined surfaces. J Mater Sci 38:2525

Brouers F, Sotolongo-Costa O (2006) Generalized fractal kinetics in complex systems (application to biophysics and biotechnology). Phys A Stat Mech Appl 368:165–175

Chauvy PF, Madore C, Landolt D (1998) Variable length scale analysis of surface topography: characterization of titanium surfaces for biomedical applications. Surf Coat Technol 110:48

Cole MW, Holter NS, Pfreifer P (1986) Henry's law of adsorption on a fractal surface. Phys Rev B 33:8806–8809

Dimri VP (1992) Deconvolution and inverse theory. Elsevier Science Publishers, Amsterdam, London, New York, Tokyo

Dimri VP (2000) Fractal dimension analysis of soil for flow studies. In: Application of fractals in earth sciences. CRC Press, USA, pp 189–193

Fang TH, Chang WJ (2003) Effects of AFM-based nanomachining process on aluminum surface. J Phys Chem Solids 64:913

Fripiat JJ, Gatineau L, Van Damme H (1986) Multilayer physical adsorption on fractal surfaces. Langmuir 2:562–567

Joseph IG (2003) Scanning electron microscopy and X-Ray microanalysis, 3rd edn. Springer, US

Lasia A, Conway BE, Bockris J, White RE (1999) Electrochemical impedance spectroscopy and its applications: modern aspects of electrochemistry, vol 32. Kluwer Academic/Plenum Publishers, New York, pp 143–248

Li JM, Lu L, Lai MO, Ralph B (2003) Image-based fractal description of microstructures. Kluwer, The Netherlands. ISBN 1 402075073

Mandelbrot BB (1983) The fractal geometry of nature. WH Freeman & Company, New York

Maus S, Dimri VP (1994) Fractal properties of potential fields caused by fractal sources. Geophys Res Lett 21:891–894

Maus S, Dimri VP (1995) Potential field power spectrum inversion for scaling geology. J Geophys Res 100:12605–12616

Maus S, Dimri VP (1996) Depth estimation from the scaling power spectrum of potential fields. Geophys J Int 124:113–120

Othman MR, Mustafa NNN, Ahmad NNN (2006) Effect of thermal treatment on the microstructure of sol–gel derived porous alumina modified platinum. Micropor Mesopor Mater 91:268

Peleg S, Naor J, Hartley R, Avnir D (1984) Multiple resolution texture analysis and classification. IEEE Trans Pattern Anal Mach Intell 6:518

Pfeifer P (1988) Fractal in surface science: scattering and thermodynamics of adsorbed films, in Chemistry and physics of solid surfcaes. In: Vanselow R, Hower RF (eds) (vol VII). Springer, Berlin, p 283–305

Pfeifer P, Avnir D (1983) Chemistry in noninteger dimensions between two and three. I. F heterogeneous surfaces. J Chem Phys 79(7):3558–3565

Pfeifer P, Obert M, Cole MW (1989) Fractal BET and FHH theories of adsorption: a comparative study. Proc Roy Sco Lond A 423:169–188

Price RL (2005) Microscopy and microanalysis. Supplement S02 11:1320–1321

Risovic D, Poljack SM, Furic K, Gojo M (2008) Inferring fractal dimension of rough/porous surfaces—a comparison of SEM image analysis and electrochemical impedance spectroscopy methods. Appl Surf Sci 255:3063–3070

Russ CJ, Mainsah E, Greenwood JA, Chetwynd DG (2001) Fractal geometry in engineering, metrology and properties of engineering surfaces. Kluwer Academic Publishers Inc., MA, USA

Seitavuopio P (2006) The roughness and imaging characterization of different pharmaceutical surfaces. Ph.D. thesis, University of Helsinki, Helsinki

Shapiro SS, Wilk MB (1965) An analysis of variance test for normality (complete samples). Biometrika 52(3–4):591–611

Srihari V (2007) Studies on adsorption capacities of selective Indigenous agro-wastes for dephenolation of Aqueous media. Unpublished Ph.D. thesis, SASTRA University, Thanjavur

Srihari V, Das A (2004) Thermodynamic evaluation of phenol adsorption by agricultural waste—*Hemidesmus indicus*. J Eng Day 6(10):5–7

Zarzycki J(1987) Fractal properties of gels. J Non-Cryst Sol 96:173–184

The Multi-fractal Scaling Behavior of Seismograms Based on the Detrended Fluctuation Analysis

Simanchal Padhy

Abstract The multi-fractal scaling properties of seismograms are investigated in order to quantify the complexity associated with high-frequency seismic signals. The third-order MDFA (MDFA3) method is capable of characterising the multi-fractality of earthquake records associated with frequency- and scale-dependent correlations of small and large fluctuations within seismogram. These correlations are related to changes in waveform properties and hence are a measure of the heterogeneities of the medium at different scales, sensed by direct and converted phases in a seismogram with different amplitudes and phases. The non-linear dependence of generalised Hurst and mass exponent with order q confirms the multi-fractal nature of earthquake records. Amongst different types of earthquakes analysed, the multi-fractal properties are more pronounced for signals with distinct P-, S- and coda waves. The multi-fractal singularity spectrum parameters (maximum, asymmetry and width) are used to measure the frequency-dependent complexity of seismograms. The degree of multi-fractality decreases with increasing frequency, and is generally more for the time period windowing dominant seismic phases in the seismogram. Significant difference in spectrum width between the original record and its randomly shuffled surrogates demonstrates that the multi-fractality in earthquake records is predominantly due to long-range correlation of small and large fluctuations within seismogram, although its origin due to broad probability distribution cannot be completely ruled out, based on the values of scaling exponent ($H_q \approx 0.5$) and their weak q-dependency for the surrogates.

S. Padhy (✉)
Seismological Observatory, CSIR-National Geophysical Research Institute (NGRI),
Uppal Road, Hyderabad 500007, India
e-mail: spadhy@ngri.res.in; sima.padhy@gmail.com

V.P. Dimri (ed.), *Fractal Solutions for Understanding Complex Systems in Earth Sciences*, Springer Earth System Sciences,
DOI 10.1007/978-3-319-24675-8_7

1 Introduction

A signal X[n] is scale invariant when $X[c \cdot n] = c^H \cdot X[n]$, where H is the Hurst exponent, a dimensionless estimator for the self-similarity of a time series, and the constant c indicates contraction if $c > 1$, or dilation if $c < 1$. The exponent H can be estimated from the decay rate of power spectrum of time series. However, the spectral analysis suffers from the problem of aliasing that occurs for frequencies beyond the Nyquist frequency (half of the sampling frequency). Thus, the standard spectral approach is not sufficient to describe the true scaling behavior of time series at higher frequencies. In such case, fractal analyses can be used to estimate the power-law exponent, H to define the scale-invariant structure of time series data.

The mono-fractal structures are defined by a single power-law exponent and assume that the scale invariance is independent of time and space. However, the spatial and temporal variations in scale-invariant structure are characterised by a spectrum of power-law exponents (multi-fractal structure) rather than a single power-law exponent (mono-fractal structure).

Many time series data including geophysical signals do not exhibit a simple mono-fractal scaling behavior (Hu et al. 2001; Kantelhardt et al. 2001); their scaling behavior is more complicated, and different scaling exponents are required for different parts of time series (Chen et al. 2002). In such case, multi-fractal analysis is needed that requires a multitude of scaling exponents for the full description of scaling behavior of such records. The multi-fractal scaling in a time series can be ascribed to (i) broad probability density function for the values of the time series or (ii) different long-range correlations of the small and large fluctuations in the data. Recently, Telesca et al. (2015) showed that the origin of multi-fractality of volcanic signals recorded during pre- and eruptive phases in Canary Islands is due to long-range correlation related to the change in dynamics during volcanic eruption.

The scaling properties of both temporal and spatial distribution of earthquakes have been studied by using fractal methods (Kagan and Knopoff 1980; Main and Burton 1984; Smalley et al. 1987; Rundle 1989; Paladin and Vulpiani 1987, Hirata and Imoto 1991; Godano et al. 1996; Telesca et al. 2001, 2004; Dimri 2005; Tang et al. 2012; Padhy et al. 2014).

Very recently a few statistical methods have been performed on seismograms to investigate their dynamical characteristics. One of these is the Fisher–Shannon method that was applied to identify the tsunamigenic character in seismograms of very large earthquakes occurred worldwide (Telesca et al. 2013), to have additional information on the seismic hazard (Telesca et al. 2014a) or to detect dynamical changes correlated with different stress states of the magmatic setting and the plumbing system in volcanoes (Telesca et al. 2014b).

In this study, we analyse seismic waveforms to explain the complexity of seismograms in terms of change in dynamics of the system including medium heterogeneities, by using multi-fractal methods.

The earthquake signal, that characterises a complex dynamical system, often exhibits long-range correlations (Sornette 2004) of fluctuations in the data. It is important to quantify such long-range correlations for a better understanding of the dynamics of the underlying complex systems. Amongst the various methods used to investigate the fractal scaling properties of non-stationary time series, the most effective is the detrended fluctuation analysis (DFA). The DFA is a technique able to determine the fractal scaling properties and long-range correlations in noisy, non-stationary time series (Buldyrev et al. 1995, Bunde et al. 2000; Talkner and Weber 2000; Ashkenazy et al. 2001). The DFA method was generalised to multi-fractal non-stationary time series data by Kantelhardt et al. (2002), referred to as multi-fractal DFA (MDFA). Later on this method has been successfully applied to study the multi-fractal scaling behavior of many non-stationary time series data (Kantelhardt et al. 2003; Telesca et al. 2004, Lan et al. 2008; Shang et al. 2008; Yuan et al. 2009).

In this study, the MDFA method is used to investigate the multi-fractal scaling properties in earthquake records by analysing the multi-fractal spectrum. The multi-fractal spectrum is obtained with optimal choice of model parameters suited to earthquake data analysed here. We compare the width and shape of multi-fractal spectrum obtained for different events to characterise the observed complexity of seismogram. We examine the dependence of different parts of seismogram, data length (lapse time), frequency band, sampling frequency on the nature of the multi-fractal spectrum and its properties, and ultimately interpret the variation in width and shape of multi-fractal spectra to infer the nature of medium heterogeneities. Finally, we investigate the origin of multi-fractality in earthquake records analysed.

2 Method of Analysis

The DFA for a one-dimensional data series can be described as follows. Let $X(i)$ be a time series of length N ($i = 1, 2, 3, \ldots, N$). The trajectory or profile $Y(i)$ of the time series is determined by taking the sum of deviation from the mean value, $\bar{X}$ (Kantelhardt et al. 2002; Telesca et al. 2004) i.e.

$$Y(i) = \sum_{k=1}^{i} (X(k) - \bar{X}), \quad i = 1, 2, 3, \ldots, N \tag{1}$$

The integrated time series is divided into $N_s = \text{int}(N/s)$ non-overlapping segments of equal size s. Since the length of the series may not be an integral multiple of s, an unequal and short part ($<s$) of the profile may be left at the end of the series. In order to consider such part, the same procedure is repeated in the backward direction starting from the end. Thus, $2N_s$ segments are obtained altogether. Then the local trend for each of the $2N_s$ segments is calculated by a least-squares fit of a polynomial function. The variance of each segment v in forward direction is given by:

$$F(s,v)_f = \frac{1}{s}\sum_{i=1}^{s}\{Y[(v-1)s+i] - y_v(i)\}^2, \tag{2}$$

where v may vary from 1 to N_s and $y_v(i)$ represents the least-squares fit of the segment v for profile $Y(i)$. Similarly, the variance of each segment in backward direction is given by:

$$F(s,v)_b = \frac{1}{s}\sum_{i=1}^{s}\{Y[N-(v-N_s)s+i] - y_v(i)\}^2, \tag{3}$$

where v may vary from $N_s + 1$ to $2N_s$.

After detrending the time series, an average is performed over all the segments ($v = 1$–$2N_s$) to obtain the qth-order fluctuation function as:

$$F_q(s) = \left[\frac{1}{2N_s}\sum_{v=1}^{2N_s}[F(s,v)]^{q/2}\right]^{1/q}, \tag{4}$$

where in general, the index variable q may take any real number other than zero. Since for $q \to 0$, $1/q$ blows up, $F_q(s)$ cannot be obtained by the normal averaging procedure described in Eq. (4), instead a logarithmic averaging procedure is applied to get:

$$F_0(s) = \exp\left\{\frac{1}{4N_s}\sum_{v=1}^{2N_s}\ln[F(s,v)]\right\} \approx s^{H_{q=0}}, \tag{5}$$

A similar procedure is performed for different values of time scale length s of the segment v. If the time series is governed by long-range power-law correlation, $F_q(s)$ also follows a power-law for large values of s as:

$$F_q(s) \propto s^{H_q}, \tag{6}$$

The plot of $\log_2 F_q(s)$ versus $\log_2 s$ gives a straight line with slope H_q, known as the generalised Hurst exponent, for a given value of q. The slope H_q, for positive q, describes the scaling behavior of segments with large fluctuations, while that for negative q, describes the scaling behavior with small fluctuations. From the values of H_q obtained for each q, one can determine the scaling behavior of the function $F_q(s)$. A mono-fractal time series is characterised by a unique H_q for all values of q. In cases, when small and large fluctuations scale differently (multi-fractal time series), H_q strongly depends on q. For positive values of q, the scaling behavior of segments with large fluctuations is characterised by a smaller H_q. On the contrary, for negative values of q, the scaling behavior of segments with small fluctuations is characterised by a larger H_q (Kantelhardt et al. 2002).

The generalised Hurst exponent H_q based on the MDFA method is related to the classical or global scaling exponent t_q as:

$$t_q = qH_q - 1, \tag{7}$$

A mono-fractal series with long-range correlation is characterised by linearly dependent t_q with single Hurst exponent H. Multi-fractal series, however, is characterised by non-linearly dependent t_q with multiple Hurst exponent (Ashkenazy et al. 2003).

Using the Legendre transformation, one can introduce the spectrum of local dimensions (Holder exponents or singularities), also called as multi-fractal spectrum, D_q from the scaling exponent, t_q as:

$$D_q = qh_q - t_q, \tag{8}$$

where $h_q = \frac{\mathrm{d}t_q}{\mathrm{d}q}$ is the q-order singularity exponent. The multi-fractal spectrum D_q expresses the dimension of the subset of the series characterised by singularity strength h_q, and its width denotes the range of exponents. The spectrum can be quantitatively expressed by least-squares fitting it to a quadratic function around its maximum $h_{q,\max}$ (Shimizu et al. 2002) as:

$$D_q = a \cdot \left(h_q - h_{q,\max}\right)^2 + b \cdot \left(h_q - h_{q,\max}\right) + c, \tag{9}$$

where c is an additive constant, $c = D_q(h_{q,\max}) = 1$. The coefficient b indicates the asymmetry of the spectrum. The width of the spectrum, w, obtained by extrapolating the fitted curve to zero, is defined as:

$$w = h_{q1} - h_{q2}, \text{ with } D_q(h_{q1}) = D_q(h_{q2}) = 0.$$

For a mono-fractal series, H_q is independent of q. It thus follows from Eqs. (7) and (8) that the width of the spectrum is zero for a mono-fractal series. The three parameters ($h_{q,\max}$, w and b) characterising Eq. (9) describe the complexity of the signal. If the value of parameter $h_{q,\max}$ is low, then the signal is correlated and the underlying process loses fine structure, becoming more regular in appearance (Shimizu et al. 2002). The multi-fractal width, w, measures the range of fractal exponents in the signal; the wider the range, the higher is the degree of multi-fractality. The asymmetry parameter, b, informs about the dominance of low or high fractal exponents with respect to the other. A right-skewed spectrum represents strongly weighted high fractal exponents, corresponding to fine structures, while the left-skewed spectrum represents low fractal exponents with a smoothly varying appearance (Telesca et al. 2004).

2.1 Estimation of the Multi-fractal Spectrum of Time Series (D_q vs. H_q)

The following procedure is adopted to obtain the multi-fractal spectrum (D_q vs. h_q) of a time series (Vjushin et al. 2001; Kantelhardt et al. 2002).

(1) Computing the root-mean-square (RMS) variation of time series.
(2) Finding local detrending of the time series.
(3) Computing multi-fractal detrending, q-order RMS, $F_q(s)$ using Eq. (4). The scaling function $F_q(s)$ is obtained based on the q-order statistical moments, for q ranging between −5 and 5 with an increment of 2.
(4) Computing q-order Hurst exponent (H_q) as the slope of scaling function $F_q(s)$ for each q, and q-order mass exponent (t_q) using Eq. (7).
(5) Computing q-order singularity exponent, h_q $\left(h_q = \frac{\mathrm{d}t_q}{\mathrm{d}q}\right)$, q-order singularity dimension, D_q using Eq. (8), and
(6) Finally obtaining the multi-fractal spectrum as D_q versus h_q curve.

2.2 Selection of Parameters

The parameters, such as scale s, q-order and trend order m for obtaining the multi-fractal spectrum, are selected based on the following criteria.

2.2.1 Selection of Scale

The minimum and maximum segment sizes are selected in order to obtain numerically stable RMS values and hence to obtain a stable scale function $F_q(s)$. The minimum sample size should be considerably larger than the polynomial order m to prevent over-fitting of polynomial trend (Kantelhardt et al. 2002). The maximum segment size (i.e. scale) should be small enough in order to have large number of segments in the computation of $F_q(s)$ and hence for a stable estimation of the multi-fractal spectrum D_q (Scafetta et al. 2003). Here, we used the polynomial order for detrending the time series as 3 ($m = 3$). Based on the above criteria, we selected minimum and maximum values of scale as 16 and 1024, respectively, for computing the spectrum (D_q vs. h_q).

2.2.2 Selection of Order q

Higher value of q (both positive and negative) may induce larger numerical error in the tail of the multi-fractal spectrum. The destabilisation of F_q at large positive and negative q-orders also depends on the sample size. For example, time series with large sample size have multiple segments of small and large fluctuations, that stabilisethe F_q computation at large negative and positive q-orders. In addition, the stability of the computation of the multi-fractal spectrum depends on the difference between the segments of largest and smallest fluctuation. Time series with large multi-fractal spectrum width have large differences between the segments with the smallest and largest fluctuation and, consequently, the computation of F_q at smaller negative and positive q-orders is not stable. Here, we used the q-order that weights the local variations in time series to vary between −5 and 5 to have optimal performance of multi-fractal spectrum.

2.2.3 Selection of Trend Order m

A higher value of polynomial order, m, for detrending the time series gives rise to a more complex shape of the trend. Multi-fractal spectrum for multiple orders may be influenced by non-stationary trends in time series. Linear, quadratic, cubic or higher-order polynomials can be used in least-squares fit of time series (MDFA1, MDFA2, MDFA3, …). The potential of trend removal in a series depends on the order of polynomial used in the fitting procedure (Kantelhardt et al. 2002). Here we selected the value of m in the range 1–3 for minimum segment size of 16, as used here for the computation of multi-fractal spectrum (D_q vs. h_q).

3 Results

In Figs. 1, 2, 3 and 4, we show the q-order scaling function $F_q(s)$, q-order generalised Hurst exponent H_q, q-order mass exponent t_q and the resulting multi-fractal spectrum to investigate the multi-fractal scaling nature of noise record and three types of earthquake records. Figures 1a–e show, respectively, the time series, the scaling functions $F_q(s)$ (circles) obtained with different segment sizes (scaling, s) for different q-orders and the corresponding regression lines computed by MDFA, the q-order Hurst exponent, the q-order mass exponent and the multi-fractal spectrum for the white noise. In addition, we analysed three different types of seismograms based on the MDFA method and compared their multi-fractal spectra. These seismograms include (i) an event with clear P-, S- and surface waves with long coda waves (Event-1) (Fig. 2), (ii) an event with P-, S- and surface waves, but with more diffused and slowly decaying coda waves (Event-2) (Fig. 3) and (iii) an event with no clear S- and surface waves (Event-3) (Fig. 4). The complexities associated with different types of records may be attributed to varying degrees of medium heterogeneities, which are characterised by different degrees of multi-fractal structures expressed in terms of H_q, t_q and width and shape of multi-fractal spectrum. For all types of time series records analysed, the slope of the regression of scaling function $F_q(s)$ for different q (Figs. 1b–4b) (generalised q-order Hurst

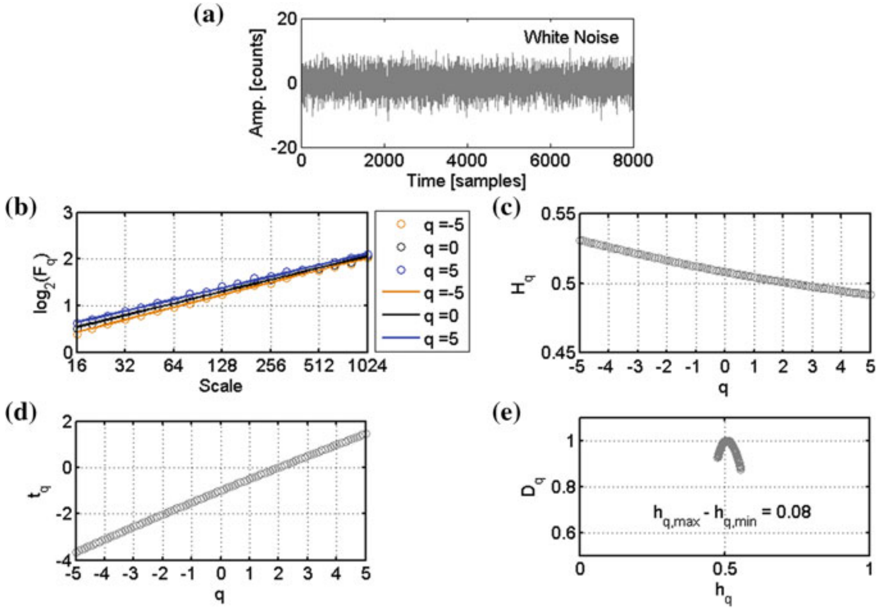

Fig. 1 MDFA3 results obtained for the white noise record. **a** White noise time series, **b** fluctuation functions $F_q(s)$ (*circles*) versus scale s, plotted in log 2–log 2 scales, for different orders q and corresponding regression lines (*solid lines*), **c** H_q functions, **d** q-order mass exponent t_q versus order q and **e** multi-fractal spectrum (plot of generalised fractal dimensions, D_q vs. q-order singularity exponents, h_q)

exponent, H_q) decreases with q (Figs. 1c–4c), although the exact nature of variations depends on the type of signal, explaining the multi-fractal structure of the data. The difference between the scaling functions for positive and negative q's is more apparent at small scales (small segment sizes) compared to the large ones (Fig. 2b). Such a difference is clearly seen for earthquake signals than noise records (see Fig. 1b). The small segments are able to distinguish between the periods with large and small fluctuations (i.e. positive and negative q's, respectively). In contrast, the large segments include several local periods with small and large fluctuations and therefore average out their differences in magnitude. For white noise, the values of H_q attain almost constant value of 0.5 with very small variations around 0.5 (Fig. 1c). The constant H_q leads to almost linear mass exponent t_q (Fig. 1d), that further leads to almost constant h_q and D_q, and finally giving rise to small arcs with very small width in the multi-fractal spectrum (Fig. 1e). The non-constant H_q values (Fig. 2c) leads to non-linear q-dependency of t_q (Fig. 2d) that further leads to parabolic (upside-down parabola) multi-fractal spectrum with large width (Fig. 2e). Almost a similar scaling behavior (q-dependency of H_q and t_q) is observed for signals of type 2 (Event-2, Fig. 3c–d) and 3 (Event-3, Fig. 4c–d), with a difference in the shape and width of their multi-fractal spectra (Figs. 3e–4e). The multi-fractal spectrum width (hereafter referred to as MS width) is a measure of the deviation

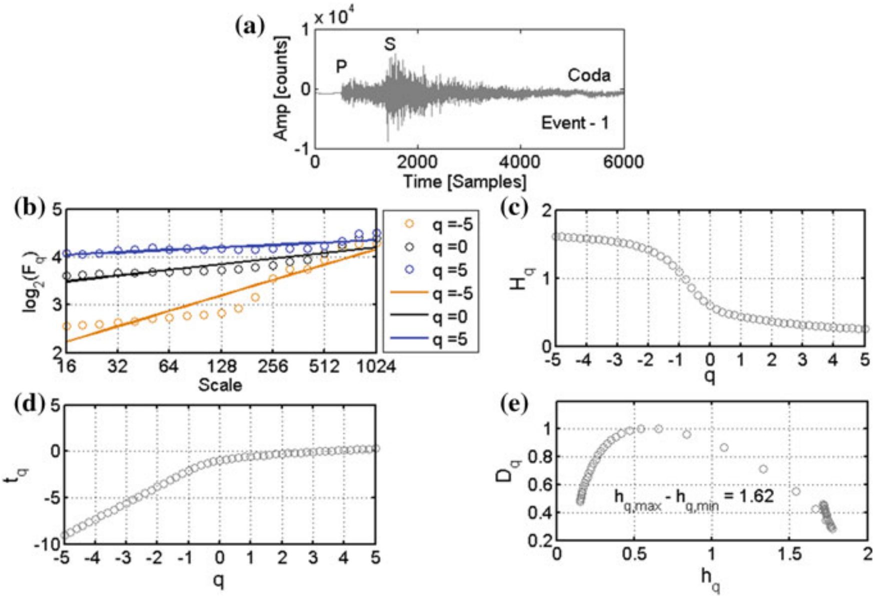

Fig. 2 Same as Fig. 1, but for an earthquake time series (Event-1), recorded with a sampling rate of 100 Hz, and characterised by clear P-, S-, surface and coda waves

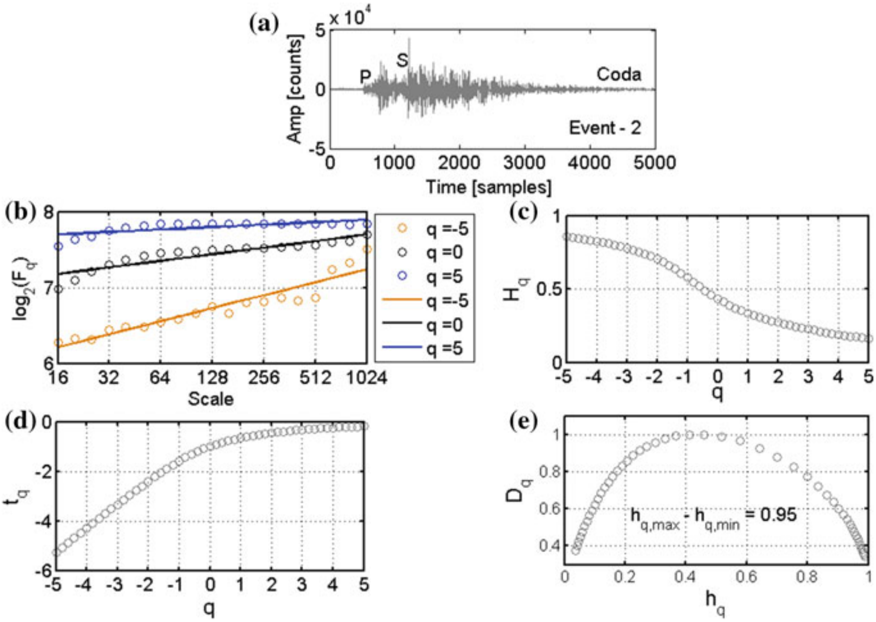

Fig. 3 Same as Fig. 1, but for an earthquake time series (Event-2) recorded with a sampling rate of 100 Hz, and characterised by P-, S-, and surface waves, but with more diffused and slowly decaying coda waves

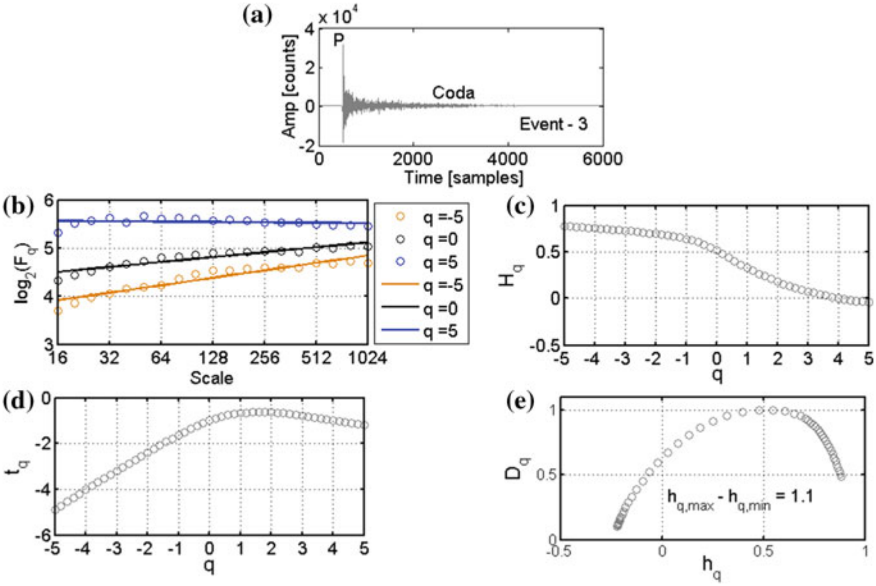

Fig. 4 Same as Fig. 1, but for an earthquake time series (Event-3) recorded with a sampling rate of 100 Hz, and characterised by no clear S- and surface waves

from average fractal structure for segments with large and small fluctuations. The value of MS width is larger for signals (Figs. 2e–4e) than noise records (Fig. 1e), that is expected because of the presence of several seismic phases of varying waveform properties in an earthquake record than the noise record. These phases are a measure of heterogeneities of the medium of different scales. Moreover, high-quality signal with good signal-to-noise ratio, such as Event-1, characterised by the presence of clear seismic phases with dominant S-wave, represents large anomaly in waveform properties, and shows spectrum with MS width larger than other signals analysed (Events-2 and 3). The values of MS width for a normal seismogram become larger than those for any seismogram with anomalous seismic phases. This property is clearly observed on comparing the MS width for normal seismogram (MS width of 1.62 for Event-1) with that of anomalous seismograms (MS width of 0.95 for Event-2 and 1.1 for Event-3).

Next, the shape of the multi-fractal spectrum of the seismogram of Event-1 is asymmetrical around the maximum $hq_{\max}$ (Fig. 2e). In particular, it is right-skewed, indicating a relative dominance of small fluctuations, while in the case of Event-3 for anomalous seismograms with strongly attenuated S-waves (Fig. 4e), the multi-fractal spectrum exhibits a long left tail indicating that the corresponding time series becomes insensitive to the local fluctuations represented by small variation and its dynamics is dominated by the large fluctuations.

4 Discussion

4.1 *Effect of Sampling Frequency and Window Length on MS Width*

The sampling frequency is related to the scale length of heterogeneities of the medium sampled by the signal. Here, we attempt to characterise these medium heterogeneities from the multi-fractal analysis of seismograms for different sampling frequencies. The sampling frequency should preferably be selected at least a magnitude higher than the dominant frequency of the observed time series so as to avoid aliasing-related artefact of the spectrum. A high sampling rate is needed for a better understanding of the small-scale medium heterogeneities. Assuming a dominant frequency of ~ 10 Hz for local to regional earthquakes analysed here, we calculated the MS width for sampling frequencies of 25, 50 and 100 Hz, all greater than twice the dominant frequency (Nyquist rate = 20 Hz). It is observed from Fig. 5 that the MS width decreases with increase in sampling frequency, consistently with the nature of variations of scaling function $Fq(s)$ (Figs. 2b–4b) with scale.

Figure 6 shows the variation of MS width with the length of the time series starting from the pre-event noise. If the MS width for noise is smaller than that for signal, we see that, except Event-1, for the other signals the width increases at beginning from minimum corresponding to pre-event noise to maximum corresponding to P-wave

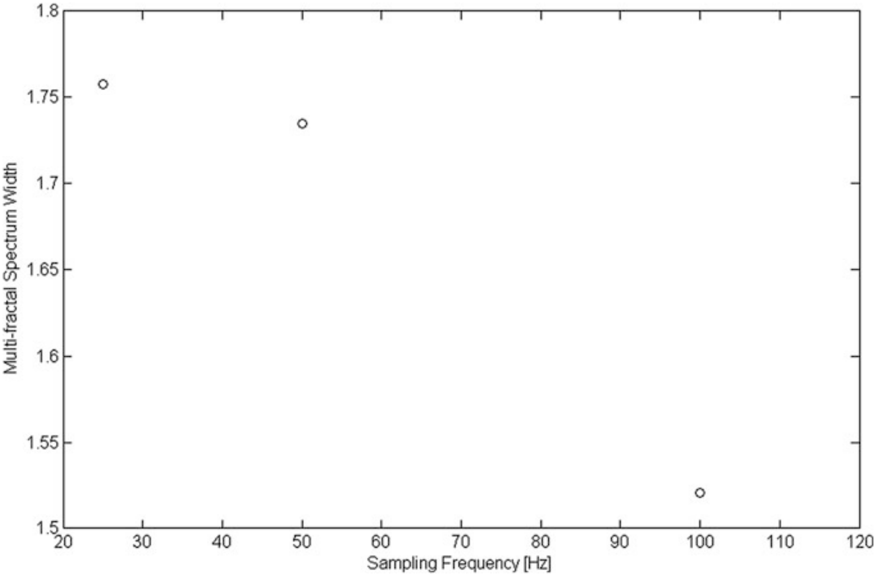

Fig. 5 Variation of MS width with sampling rates of 25, 50 and 100 Hz for Event-1. Similar variation is observed for other events

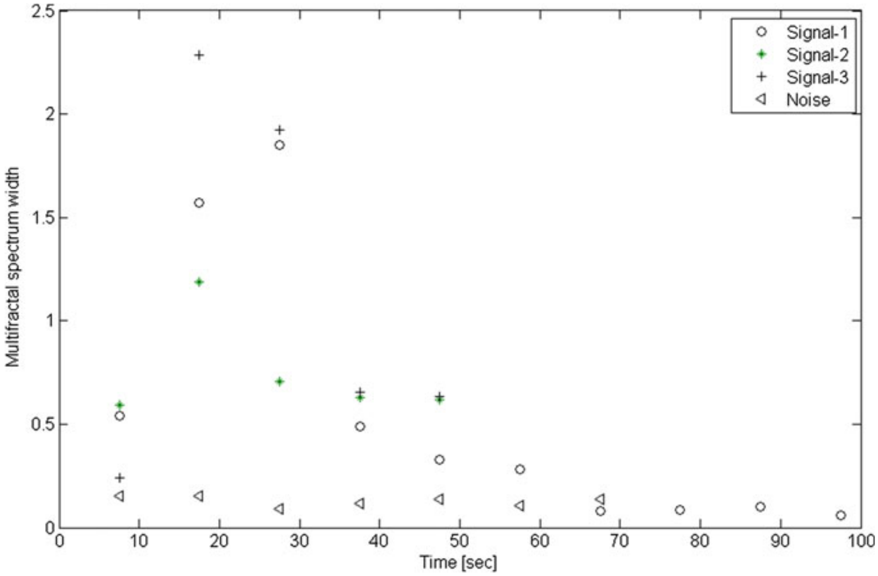

Fig. 6 Variation of MS width with lapse time (time measured from the beginning of record), used for computing multi-fractal spectrum for both noise and signals used in this study

onset, then decreases corresponding to the arrival of S-wave, and finally reaches the lowest value corresponding to later coda arrivals of smaller amplitude at long lapse times. Such lapse time dependence of MS width suggests that the change in waveform properties (amplitude and phase) is maximum between pre-event noise and P-wave than that encountered between P- and S-wave. However, for Event-1, for which S-wave energy dominates the entire seismogram, the MS width reaches maximum corresponding to the S-wave arrival group, representing the maximum waveform change related to S-wave arrival in a seismogram. Thus, the MS width is a measure of the degree of waveform change with lapse time in a seismogram, and its variation depends on the nature of seismogram.

For seismograms of short duration with an unknown trend, application of the MDFA method for different detrending polynomial orders will help to distinguish spurious spikes or transients from true seismic phases in a seismogram. This aspect of automatic seismic phase detection in a seismogram with low signal-to-noise ratios, that will accurately estimate the arrival times of different phases is an important input to travel-time seismic tomography studies, is planned in future studies.

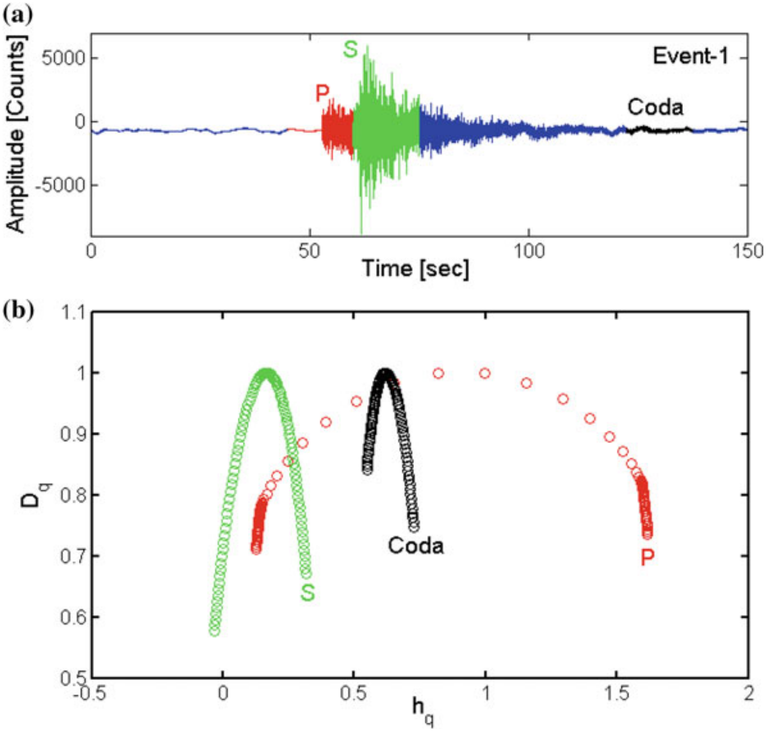

Fig. 7 Comparison of multi-fractal spectra for **a** different parts of seismogram windowed around P-, S- and coda waves. **b** Comparison of MS width for different parts of the seismogram

4.2 Effect of Different Parts of Seismogram

We analysed different parts of seismogram windowing different phases, such as P-, S- and coda waves (Fig. 7a), to examine the nature of heterogeneities sampled by each phase and their effects on MS width and shape (Fig. 7b). We found that the change in MS width is large corresponding to the P-wave window in a seismogram (Fig. 7b), that corresponds to large change in both amplitude and phase of the signal against its background. The coda wave window is found to exhibit minimal width, and this is because the change in waveform amplitude and phase for coda waves against its background is much less than those for P- and S-waves (Fig. 7a).

4.3 Effect of Filtering

We examined the effect of filtering on multi-fractal spectrum by examining the MS width obtained from analysing the band-pass filtered seismograms in six frequency

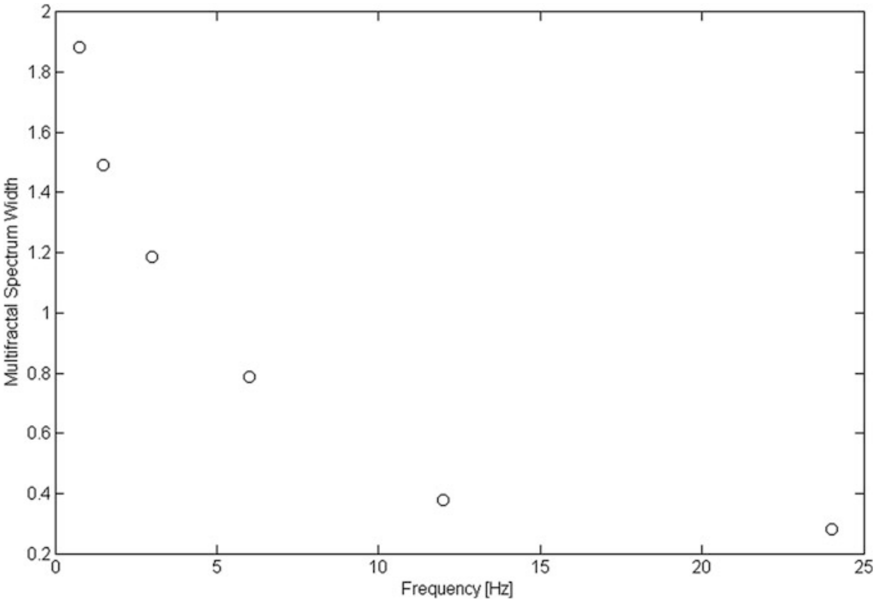

Fig. 8 Variation of MS width with central frequency after the seismograms from Event-1 are band-pass filtered. The bands used for filtering are 0.5–1, 1–2, 2–4, 4–8, 8–16 and 16–32 Hz with central frequencies at 0.75, 1.5, 3, 6, 12 and 24 Hz

bands with central frequencies at 0.75, 1.5, 3, 6, 12 and 24 Hz. It is observed from Fig. 8 that the MS width is maximum at lower frequencies (<6 Hz) and gradually decreases with increase in frequency. We observed that the MS width is relatively minimum for frequencies around 12 Hz, which is close to the dominant frequency of 10 Hz, as assumed in this study.

4.4 *Origin of Multi-fractality*

We investigate the origin of multi-fractality in the analysed seismograms by randomly shuffling the original time series. During the random shuffling, all correlations in the time series are destroyed. Hence, if multi-fractality is due to long-range correlation, the shuffled series exhibits mono-fractal scaling. If both the original and shuffled series exhibit same scaling, then the multi-fractality is due to broad probability density function of the time series. Figure 9a–b shows, respectively, the multi-fractal spectra and the scaling exponents of the original time series and those of ten surrogates. It is clear that the spectra of surrogates, centred around 0.5, are narrower than those of the original time series. These results confirm that the multi-fractal properties of the earthquake records are dominantly due to long-range correlations. However, because the surrogates show weak q-dependence of the

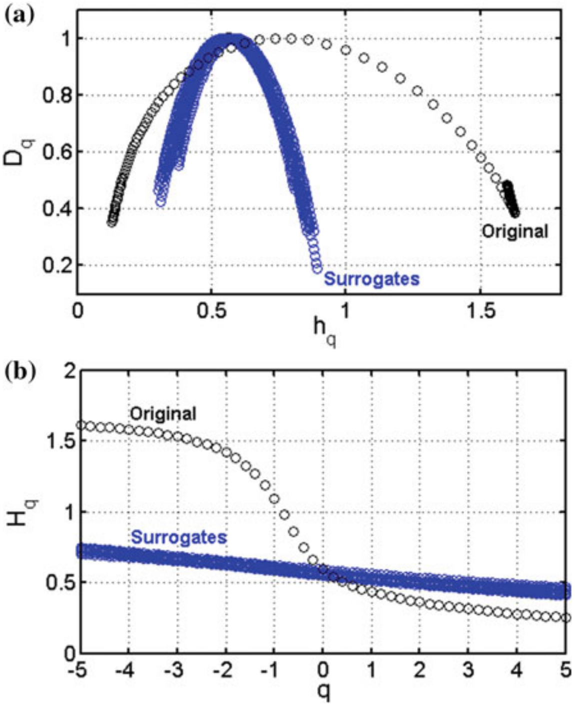

Fig. 9 Comparison of the **a** multi-fractal spectra and **b** generalised Hurst exponents of original time series record of Event-1 and its ten randomly shuffled surrogates

scaling exponents *Hq*, which are not exactly equal to 0.5, the effect of broad probability distribution cannot be ruled out (Kantelhardt et al. 2002). In summary, the multi-fractal properties of the earthquake records partly result from long-range correlations and partly from broad distributions.

5 Conclusions

The multi-fractal DFA was applied in scaling analysis of earthquake seismograms to characterise their complexity. The study reveals that the degree of multi-fractality is higher for seismograms than noise records, due to the co-existence of seismic phases of different waveforms. The large spectrum width is found for the part of seismogram containing P-waves, representing a sharp change in the waveform properties of signal against the pre-event noise. However, for seismograms with anomalous seismic phases, the maximum width coincides with time of occurrences of those phases. We could resolve the frequency-dependent scaling properties of the seismogram, even of finite length, based on different correlations of small and large fluctuations within a seismogram. The minimal and stable multi-fractal spectrum width is obtained for band-passed signals with central frequencies close to the dominant frequency of the signal. By comparing the multi-fractal spectrum for original series to those for randomly shuffled series, we can attribute the multi-fractality for the analysed seismograms to long-range correlations, although the minimal effect of broad probability distribution on its origin cannot be completely ruled out.

Acknowledgements The author (SP) sincerely thanks anonymous reviewers and Prof. Vijay P. Dimri for their helpful review that improved the clarity of this work. SP acknowledges Prof. Dimri for his kind invitation to contribute this work as one of the chapters of the book to be published by Springer. The Director, CSIR-NGRI is thanked for his kind permission to publish this work.

References

Ashkenazy Y, Ivanov PC, Havlin S, Peng CK, Goldberger AL, Stanley HE (2001) Magnitude and sign correlations in heart beat fluctuations. Phys Rev Lett 86:1900–1903

Ashkenazy Y, Havlin S, Ivanov PC, Peng CK, Schulte-Frohlinde V, Stanley HE (2003) Magnitude and sign scaling in power-law correlated time-series. Phys A 323:19–41

Buldyrev SV, Goldberger AL, Havlin S, Mantegna RN, Matsa ME, Peng CK, Simons M, Stanley HE (1995) Long-range correlation properties of coding and non-coding DNA sequences: GenBank analysis, Phys. Rev. E 51:5084–5091

Bunde A, Havlin S, Kantelhardt JW, Penzel T, Peter JH, Voigt K (2000) Corrrelated and uncorrelated regions in heart-rate fluctuations during sleep. Phys Rev Lett 85:3736–3739

Chen Z, Ivanov PC, Hu K, Stanley HE (2002) Effect of non-stationarities on detrended fluctuation analysis. Phys Rev E 65:041107

Dimri VP (2005) Fractals in geophysics and seismology: an introduction. In: Dimri VP (ed) Fractal behaviour of the earth system. Springer, Berlin, pp 1–19

Godano C, Alonzo ML, Bottari A (1996) Multifractal analysis of the spatial distribution of earthquakes in southern Italy. Geophys J Int 125:901–911

Hirata T, Imoto M (1991) Multi-fractal analysis of spatial distribution of micro-earthquakes In the Kanto region. Geophys J Int 107:155–162

Hu K, Ivanov PC, Chen Z, Carpens P, Stanley HE (2001) Effects of trends on detrended fluctuation analysis. Phys Rev E 64:011114

Kagan YY, Knopoff L (1980) Spatial distribution of earthquakes: the two-point correlation function. Geophys J R Astron Soc 62:303–320

Kantelhardt JW, Zschiegner SA, Bunde EK, Havlin S, Bunde A, Stanley HE (2002) Multi-fractal detrended fluctuation analysis of non-stationary time series. Phys A 316:87–114

Kantelhardt JW, Konscienly-Bunde E, Rego HHA, Havlin S, Bunde A (2001) Detecting long-range correlations with detrended fluctuation analysis. Physica A 295:441–454

Kantelhardt JW, Rybski D, Zschiegner SA, Braun P, Bunde EK, Livina V et al (2003) Multifractality of river runoff and precipitation: comparison of fluctuation analysis and wavelet methods. Phys A 330:240–245

Lan T-H, Gao ZY, Abdalla Ahmed N, Cheng B, Wang S (2008) Detrended fluctuation analysis as a statistical method to study ion single channel signal. Cell Biol Int 32:247–252

Main IG, Burton PW (1984) Information theory and the earthquake-magnitude distribution. Bull Seismol Soc Am 74:1409–1426

Padhy S, Mishra OP, Subhadra N, Dimri VP, Singh OP, Chakrabortty GK (2014) Effects of errors and biases on the scaling of earthquake spatial pattern: application to the 2004 Sumatra-Andaman sequence. Nat Hazards 1–22

Paladin G, Vulpiani A (1987) Anomalous scaling laws in multifractal objects. Phys Rep 156:147

Rundle JB (1989) Derivation of the complete Gutenberg-Richter frequency-magnitude relation using the principle of scale invariance. J Geophys Res 94:12337–12342

Scafetta N, Griffin L, West BJ (2003) Hölder exponent spectra for human gait. Phys A 328:561–583

Shang P, Lu Y, Kamae S (2008) Detecting long-range correlations of traffic time series with multifractal detrended fluctuation analysis. Chaos Solitons Fractals 36:82–90

Shimizu Y, Thurner S, Ehrenberger K (2002) Multifractal spectra as a measure of complexity in human posture. Fractals 10:103–116

Smalley RF, Chatelain JL, Turcotte DL, Prevot R (1987) A fractal approach to the clustering of earthquakes: applications to the seismicity of the New Hebrides. Bull Seismol Soc Am 77:1368–1381

Sornette D (2004) Critical phenomena in natural sciences, 2nd edn. Springer, Berlin

Talkner P, Weber RO (2000) Power spectrum and detrended fluctuation analysis: application to daily temperatures. Phys Rev E 62:150–160

Tang YJ, Chang YF, Liou TS, Chen CC, Wu YM (2012) Evolution of the temporal multi-fractal scaling properties of the Chiayi earthquake (ML = 6.4), Taiwan. Tectonophysics 546–547:1–9

Telesca L, Cuomo V, Lapenna V, Macchiato M (2001) Identifying space-time clustering properties of the 1983–1997 Irpinia-Basilicata (southern Italy) seismicity. Tectonophysics 330:93–102

Telesca L, Lapenna V, Macchiato M (2004) Mono- and multi-fractal investigation of scaling properties in temporal patterns of seismic sequences. Chaos Solitons Fractals 19:1–15

Telesca L, Lovallo M, Chamoli A, Dimri VP, Srivastava K (2013) Fisher-Shannon analysis of seismograms of tsunamigenic and non-tsunamigenic earthquakes. Phys A 392:3424–3429

Telesca L, Lovallo M, Alcaz V, Ilies I (2014a) Investigating the inner time properties of seismograms by using the Fisher information measure. Phys A 409:154–161

Telesca L, Lovallo M, Martì Molist J, Lopez Moreno C, Abella Mendelez R (2014b) Using the Fisher-Shannon method to characterize continuous seismic signal during volcanic eruptions: application to 2011–2012 El Hierro (Canary Islands) eruption. Terra Nova 26:425–429

Telesca L, Lovallo M, Molist JM, Moreno CL, Melendez RA (2015) Multi-fractal investigation of continuous seismic signal recorded at El Hierro volcano (Canary Islands) during the 2011–2012 pre- and eruptive phases. Tectonophysics 642:71–77

Vjushin D, Govindan RB, Monetti RA, Havlin S, Bunde A (2001) Scaling analysis of trends using DFA. Phys A 302:234–243

Yuan Y, Zhuang X-T, Jin X (2009) Measuring multi-fractality of stock price fluctuation using multi-fractal detrended fluctuation analysis. Phys A 388:2189–2197

Fractal Methods in the Investigation of the Time Dynamics of Fires: An Overview

Luciano Telesca

Abstract Fires represent one of the most critical issues in the context of natural hazards. Yearly, they affect large areas worldwide causing loss of biodiversity, decrease in forests, alteration of landscape, soil degradation, increase in greenhouse, etc. Most of these fires have anthropic causes, however there are natural factors, above all summer drought, that strongly influence fire ignition and spread. The investigation of the time dynamics of fires can be carried out considering the fire process per se or focusing on some signal whose variability can be informative of a fire occurrence. In the first case, fires are described by a stochastic point process, whose events are identified by spatial location, occurrence time and size of burned area, or amount of loss. In the second case, time-continuous signals are employed to reveal indirectly the occurrence of fires; one of the mostly used signals is the satellite normalized difference vegetation index (NDVI) that gives information about the "health" of vegetation and, thus, is suited to enhance the status of vegetation after a fire stress. In both cases, the concept of fractal can be used to qualitatively and quantitatively characterize the time dynamics of fires. Fractals are featured by power-law statistics, and, if applied to time series, can be a powerful tool to investigate their temporal fluctuations, in terms of correlation structures and memory phenomena. In the present review we describe fractal methods applied to fire point processes and satellite time-continuous signals that are sensitive to fire occurrences.

1 Introduction

To quantitatively characterize fire dynamics, methodologies, which allow to extract robust features hidden in their complex time fluctuations, have to be employed. Fractality is one of the aspects of such complexity. A fractal is defined as an object

---

L. Telesca (✉)
Institute of Methodologies for Environmental Analysis, National Research Council,
C. da S. Loja, Tito 85050, PZ, Italy
e-mail: luciano.telesca@imaa.cnr.it

V.P. Dimri (ed.), *Fractal Solutions for Understanding Complex Systems in Earth Sciences*, Springer Earth System Sciences,
DOI 10.1007/978-3-319-24675-8_8

whose sample path included within some radius scales with the size of the radius. From such definition, clearly fractal processes evidence a scaling behavior, which implies that the statistics used to describe them are power laws. In fact, consider a statistics $f(x)$, which depends continuously on the scale x, over which the measurements are taken. Suppose that changing the scale x by a factor a will effectively scale the statistics $f(x)$ by another factor $g(a)$, $f(ax) = g(a)f(x)$. The only nontrivial solution for this scaling equation is given by $f(x) = bg(x)$, $g(x) = x^c$, for some constants b and c (Thurner et al. 1997, and references therein). Therefore, power-law statistics and fractals are very closely related concepts.

A fractal signal can be investigated in terms of its geometrical characterization as self-similar curve; but if the fractality of a time series is studied in order to characterize its temporal fluctuations, we need to perform second-order fractal measures, which convey information concerning its correlation properties.

The well-known method of the power spectral density represents the standard manner to investigate the fractality of a time series. The power spectral density furnishes information on the distribution of the power of the time series at various frequency bands. Since it is calculated by Fourier transforming the series, it allows to identify periodic, multi-periodic, or no-periodic behaviors. If the time series is characterized by scaling properties the power spectral density is a power-law function of the frequency f, $S(f)\propto f^{-\beta}$, with the spectral exponent β measuring the type and the strength of the time-correlation structures intrinsic in the time series fluctuations (Havlin et al. 1999). If $\beta = 0$ the fluctuations can be considered purely random, typical of white noise processes, characterized by completely uncorrelated samples. If $\beta > 0$, the fluctuations are called persistent, meaning that positive (negative) increments are very likely followed by positive (negative) increments; this is typical of systems governed by positive feedback mechanisms. If $\beta < 0$, the fluctuations are called antipersistent, meaning that positive (negative) increments are very likely followed by negative (positive) increments; this is typical of systems governed by negative feedback mechanisms (Dimri 2000, 2005a, b).

2 Fire Sequences

2.1 Representations of Fire Sequences

A fire sequence can be considered as a realization of a marked temporal stochastic point process, which describes events that occur at some random locations in time (Cox and Isham 1980) marked by a quantity related to the burned area. Such representation was used in modeling several and diverse point processes like earthquakes (Telesca et al. 2009a, b; Telesca 2007a), lightning (Telesca et al. 2008), starquakes (Telesca 2005), solar flares (Telesca 2007b), and some human and social disasters (Telesca and Lovallo 2006, 2007, 2008).

A temporal point process may display a fractal behavior if a number of its relevant statistics evidence scaling with related scaling coefficients that indicate the represented phenomenon contains clusters of points over a relatively large set of timescales (Lowen and Teich 1993, 1995; Teich et al. 1996).

In order to appropriately analyze the temporal properties of a fire sequence, we need a proper representation of the series of fire events; depending on this representation, suitable methods will be applied to disclose its fractal behavior.

A discrete-time process can be derived from the stochastic point process in two equivalent ways: (1) using the interevent time series or (2) forming its relative counting process. In the first representation a discrete-time series is formed by the rule $\tau_i = t_{i+1} - t_i$, where t_i indicates the time of event numbered by the index i. In the second representation, the time axis is divided into equally spaced contiguous counting windows of duration T to produce a sequence of counts $\{N_k(T)\}$, where $N_k(T)$ represents the number of events falling into the kth window of duration T. The duration T of the window is called counting time or timescale. The latter approach considers the fire events as the events of interest and assumes that there is an objective clock for the timing of the events. The former approach emphasizes the interspike intervals and uses the event number as an index of the time.

Both representations allow us to use different statistical techniques in order to investigate the time behavior of a fire sequence, and, in particular, to identify its fractality.

It should be observed that for point processes fractality is a concept used for meaning that a process is characterized by time-clustering behavior, where time-clustering indicates a time dynamics that is opposite to a homogenous Poissonian one. The clustering behavior of a point process leads to a power-law (fractal) shape of some of the statistics, used to describe its properties (Thurner et al. 1997), and that allows estimating the so-called fractal exponent α (Lowen and Teich 1995; Teich et al. 1996), whose numerical value is an index of the presence of clusterization within the process (Lowen and Teich 1993). If the point process is Poissonian, the event occurrence times are uncorrelated; for this memoryless process $\alpha \approx 0$. On the other side, $\alpha \neq 0$ is typical of point processes with self-similar behavior; self-similar meaning that parts of the whole can be made to fit to the whole in some way by scaling (Mandelbrot 1982). Thus, we can understand that the estimation of the fractal exponent α for a fire sequence plays an important role in the general characterization of the mechanism underlying the fire phenomenon.

2.2 Methods

Depending on the time structure of the representation of a fire sequence (interevent times or counting process), different statistical measures can be defined and employed to characterize the temporal distribution of a sequence of fire events. In this review, we will describe the coefficient of variation (CV), the detrended fluctuation analysis (DFA), and the multifractal detrended fluctuation analysis

(MF-DFA) for fire sequences represented as sets of interevent times; and the Fano Factor (FF), the Allan Factor (AF), and the count-based periodogram (PG) for fire sequences represented as counting processes.

2.2.1 Coefficient of Variation (CV)

A commonly used measure to evaluate the clustering behavior of a point process is the CV, defined as

$$C_V = s_t / \langle t \rangle, \tag{1}$$

where $<\tau>$ is the mean of the interevent times and σ_τ is the standard deviation: a Poissonian process (completely random) has a CV = 1, but a clusterized process is characterized by a CV > 1. This coefficient does not give information about the timescale ranges where the process can be reliably characterized as a clustered process. The CV represents a first indicator of the presence of clustering in a point process. It only discriminates between clusterized and Poissonian sequences, but it does not convey any information about what timescales are involved in the clustering behavior (Telesca and Lasaponara 2010). This can be considered a limitation of such measure, because a complex phenomenon can be deeply known only if the different timescales governing its dynamics are well identified and understood. Figure 1 shows the CV of the interevent times of forest fire sequences recorded in the 20 regions of Italy from 1997 to 2003; all the fire sequences appear clusterized in time, since their CV is larger than 1; however, it is not possible to derive any information about the timescale ranges where the clustering behavior is effective.

2.2.2 Detrended Fluctuation Analysis (DFA)

The DFA was developed by Peng et al. (1995), and it allows to investigate the power-law correlations of nonstationary signals, whose trends should be well distinguished from the intrinsic fluctuations of the system in order to find the correct scaling behavior of the fluctuations. DFA is a fractal technique for identifying the scaling behavior of time series in the presence of possible trends whose origin and shape is not very often known, especially if the time series are observational or experimental. The method operates on the time series $x(i)$, where $i = 1,2, \ldots, N$ and N is the length of the series. With x_{ave} we indicate the mean value

$$x_{\text{ave}} = \frac{1}{N} \sum_{k=1}^{N} x(k). \tag{2}$$

The signal is first integrated

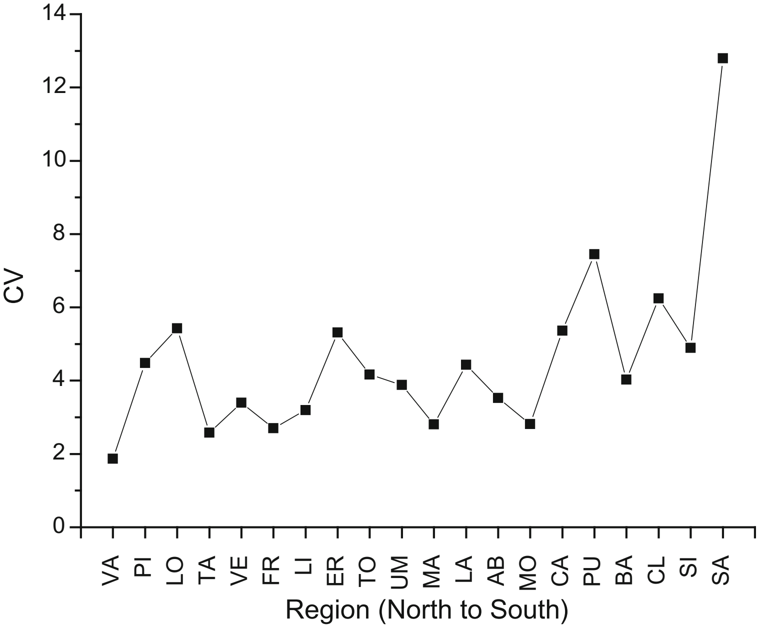

Fig. 1 Coefficient of variation versus region of the interevent time series of forest fires in Italy. Values of CV larger than 1 indicate clustering behavior. As shown by the figure, all the sequences have a CV > 1. The CV gives only information about the global clustering behavior of the fire series, but does not inform about the timescale range where the clusterization takes place (Telesca and Lasaponara 2010)

$$y(k) = \sum_{i=1}^{k} [x(i) - x_{\text{ave}}]. \tag{3}$$

Next, the integrated time series is divided into boxes of equal length, n. In each box a least-squares line is fit to the data, representing the trend in that box. The y coordinate of the straight line segments is denoted by $y_n(k)$. Next we detrend the integrated time series $y(k)$ by subtracting the local trend $y_n(k)$ in each box. The root-mean-square fluctuation of this integrated and detrended time series is calculated by

$$F(n) = \sqrt{\frac{1}{N}\sum_{k=1}^{N} [y(k) - y_n(k)]^2}. \tag{4}$$

Repeating this calculation over all box sizes, we obtain a relationship between $F(n)$, that represents the average fluctuation as a function of box size, and the box size n. If $F(n)$ behaves as a power-law function of n, data present scaling:

$$F(n) \propto n^d. \tag{5}$$

Under these conditions the fluctuations can be described by the scaling exponent d, representing the slope of the line fitting $\log[F(n)]$ to $\log(n)$. For a white noise process, $d = 0.5$. If there are only short-range correlations, the initial slope may be different from 0.5 but will approach 0.5 for large window sizes. $0.5 < d < 1.0$ indicates the presence of persistent long-range correlations, meaning that a large (compared to the average) value is more likely to be followed by large value and vice versa. $0 < d < 0.5$ indicates the presence of antipersistent long-range correlations, meaning that a large (compared to the average) value is more likely to be followed by small value and vice versa. $d = 1$ indicates flicker-noise dynamics, typical of systems in a self-organized critical state. $d = 1.5$ characterizes processes with Brownian-like dynamics.

Figure 2 shows the interevent time series (Fig. 2a) and the DFA curves (Fig. 2b) for the city fires of Anshan City (China) (Telesca and Song 2011). The city-fire data include 6529 fires occurred between 2000 and 2009. By its population, Anshan is the 5th largest city in Northeast China, and the 31st largest city in China, covering an area of 9,252 km^2, and with a population of 3.4 million. Each fire was marked by the estimated loss (in Yuan). The interevent times τ of the whole sequence show regions with low values of τ interspersed with those with high values of τ; this indicates a certain heterogeneity of the temporal distribution of fire events, leading to the presence of certain clusterization of the city fires. The DFA curve, plotted in log–log scales, shows two scaling regions with a crossover at the scale $n_C \approx 30$; at scales lower than n_C the process is characterized by weak persistence with scaling exponent about 0.68, while for scales larger than n_C the process is featured by strong persistence with scaling exponent about 1.03 that indicates a flicker-noise (1/f) behavior of the point process modeling the city-fire series. Using the relationship between the DFA scaling exponent and the spectral exponent $d = (1 + \alpha)/2$ (Havlin et al. 1999), at small scales $\alpha_{\mathrm{DFA}} \approx 0.36$ and at large scales $\alpha_{\mathrm{DFA}} \approx 1.06$. An estimate of the timescale corresponding to the crossover scale n_C can be obtained multiplying the crossover for the mean intervent time $<\tau> \sim 771$ min, thus giving a crossover timescale of about 17 days. The comparison of the DFA results with those obtained on a shuffled series (the shuffling procedure destroys the correlations and transforms the series into a purely random one) shows that the two curves (the original and the shuffled one) do not overlap and the scaling exponent evaluated for the shuffled time series is around 0.5, typical of purely random processes. This strengthens the robustness and significance of the scaling exponent estimated by using the DFA.

For loss thresholds L_{th} assuming the values 100, 500, 1000, 1500, 2000, 2500, 5000, and 10^4 Yuan, the DFA curves, plotted in log–log scales, show very similar behavior and indicate that the scaling properties of the city-fire process are invariant with the size of the loss (Fig. 3). At higher scales the range of variability of the DFA

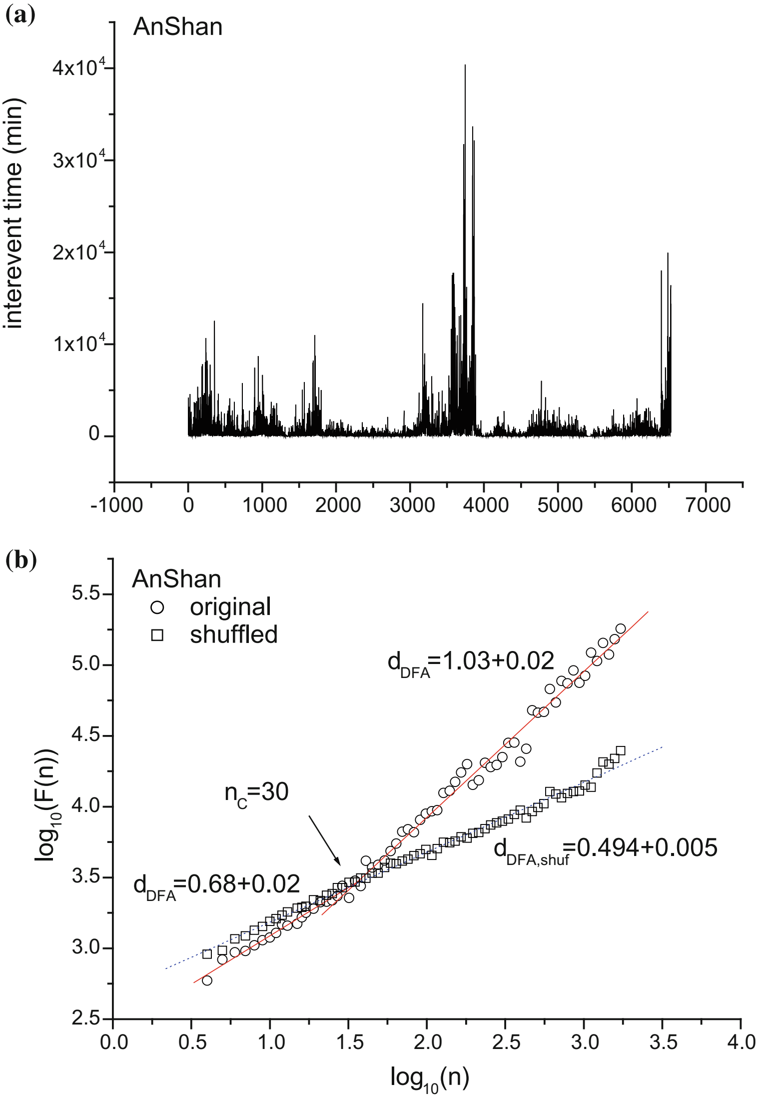

Fig. 2 **a** Interevent times of the city fires of Anshan City (Northern China). **b** DFA curves (original and shuffled) for the city fires of Anshan City (Telesca and Song 2011)

exponents is between 0.57 and 0.99. The double scaling behavior observed for very low loss thresholds tends to disappear with the increase of the threshold and to be substituted by a single scaling region with lower scaling exponent, suggesting that the sequence of large city-fires tends to behave as Poissonian processes.

2.2.3 Fano Factor (FF)

The FF is defined as the variance of the number of events in a specified counting time or timescale T divided by the mean number of events in that counting time; that is

$$\mathrm{FF}(T) = \frac{<N_k^2(T)> - <N_k(T)>^2}{<N_k(T)>}, \tag{6}$$

where <…> indicate the average value. In order to evaluate the presence of scaling, the timescale T is varied and a relationship $\mathrm{FF}(T) \sim T$ is obtained.

The FF(T) of a fractal point process with $0 < \alpha < 1$ varies as a function of counting time T as:

$$\mathrm{FF}(T) = 1 + \left(\frac{T}{T_0}\right)^{\alpha}. \tag{7}$$

The monotonic power-law increase is representative of the presence of fluctuations on many timescales (Lowen and Teich 1995). The scaling exponent α is the so-called fractal exponent. If $\alpha > 0$ then the represented phenomenon contains clusters of points over a relatively large set of timescales (Lowen and Teich 1993, 1995; Teich et al. 1996). If $\alpha \approx 0$, the city-fire occurrence process is Poissonian and the occurrence times are uncorrelated. The crossover timescale T_0 is the fractal onset time, and marks the lower limit for significant scaling behavior in the FF (Teich et al. 1996), so that for $T \ll T_0$ the clustering property becomes negligible at these timescales. Thus, T_0 is estimated as the timescale over which the FF increases as a power-law function of the timescale T. FF assumes values near unity for Poisson processes.

Figure 3 shows the FF for fire sequences occurred in southern Italy for counting times T of duration of 10 min up to 1/10 of the total period. The FF plots clearly indicate the fractal behavior of the fire sequences. The FF increases with linear form in log–log scales, and this indicates the presence of correlated structures. The early flat behavior can be interpreted as the presence of Poissonian dynamics for short timescales T up to approximately 50 min. The scaling behavior presents two timescale regimes with a crossover at about 24 h in all the plots. This crossover seems more evident in 1997 and 2001 FF plots. The fractal exponent is estimated in the longer timescale region, obtaining an estimate of α_{FF} ranging from 0.69 to 0.91. This result indicates the presence of strong time-correlated structures in the sequences of fires.

The fires are marked by a quantity that for forest fires can be the burned area, for city fires can be the loss. The variation of the fractal properties of fires depending on the intensity of such quantity becomes crucial if we investigate how the time characteristics of the fire process change with the level of the intensity of the fires. Figure 4 shows the FF for subsequences of fires with burned area $A \geq A_{\mathrm{th}}$, varying the value of the threshold burned area A_{th}. Figure 4a shows the FF curves for A_{th}

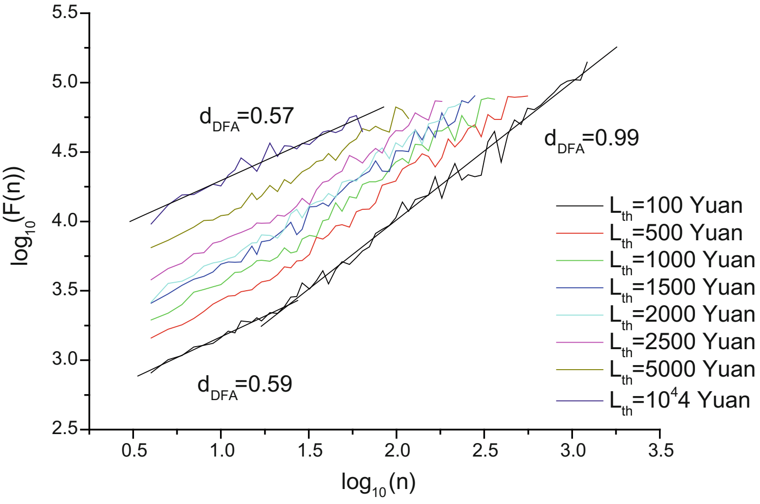

Fig. 3 DFA curves for the city fires of Anshan City depending on the loss threshold (Telesca and Song 2011)

assuming the values 0, 1, 3, 5, 10, 15, 20, 30, and 50 ha. All the FF curves, plotted in log–log scales, show clear linear behavior from the timescale $T > 10^{3.5}$ min. The exponent $\alpha_{\mathrm{FF}}(A_{\mathrm{th}})$ is a function of the threshold A_{th}. Figure 4b shows that α_{FF} decreases with the increase of the threshold area A_{th} from approximately 0.7 to 0.3, with a mean value (± standard deviation) of 0.5 (± 0.1). This behavior of α_{FF} indicates that the time-clustering degree of the events decreases with the increase of the threshold burned area. This also indicates that the fire process tends to behave in a Poissonian process with the increase of the burned area.

2.2.4 Allan Factor (AF)

Another measure, related to the variability of successive counts, useful to detect the event clustering in a point process, is the AF (Allan 1966), defined as the variance of successive counts for a specified counting time T divided by twice the mean number of events in that counting time

$$\mathrm{AF}(T) = \frac{<(N_{k+1}(T) - N_k(T))^2>}{2<N_k(T)>}. \tag{8}$$

This measure reduces the effect of possible nonstationarity of the point process, because it is defined in terms of the difference of successive counts (Viswanathan et al. 1997). As for the FF, varying the timescale T allows producing a relationship between AF(T) and T, useful to detect scaling behavior in the sequence.

Fig. 4 FF plots for the years 1997 (**a**), 1998 (**b**), 1999 (**c**), 2000 (**d**), and 2001 (**e**) of fire sequences in southern Italy (Lasaponara et al. 2005)

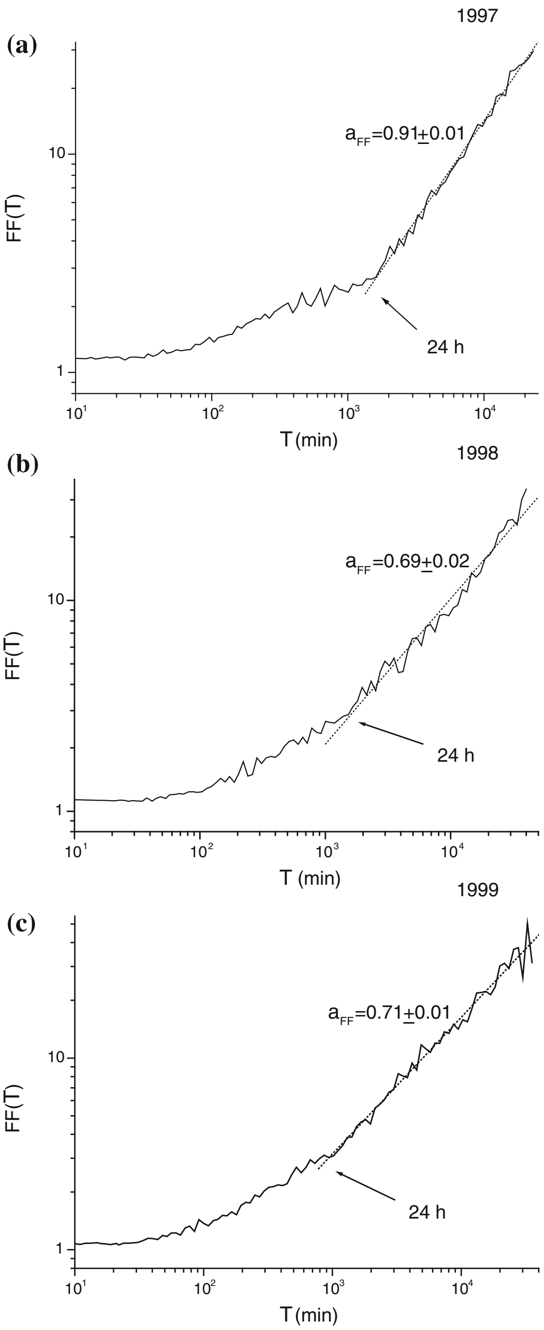

Fig. 4 (continued)

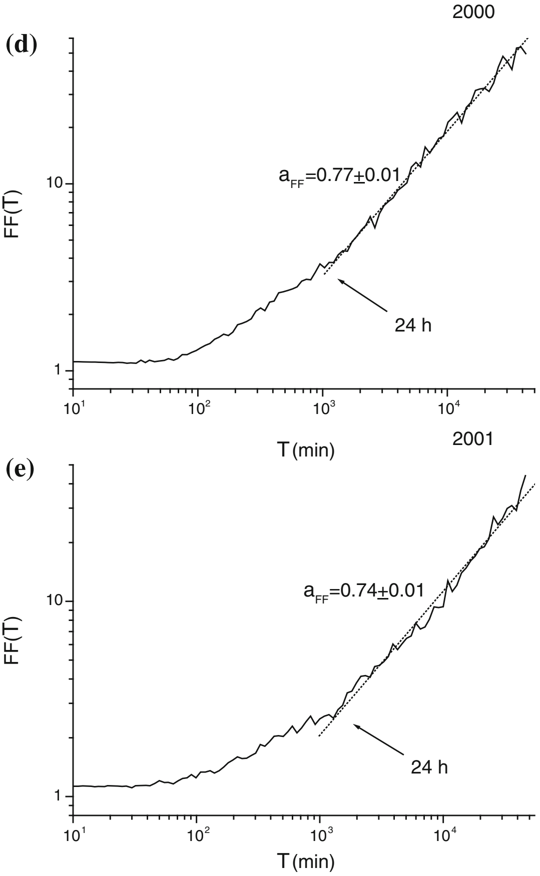

The AF of a fractal point process varies with the counting time T with a power-law form:

$$\mathrm{AF}(T) = 1 + \left(\frac{T}{T_1}\right)^{\alpha} \tag{9}$$

with $0 < \alpha < 3$ over a large range of counting times T (Lowen and Teich 1995); T_1 is the fractal onset time for the AF and is estimated as the crossover timescale between Poissonian and scaling behaviors. It is related to T_0 by (Teich et al. 1997)

$$T_0^{\alpha} T_1^{-\alpha} = 2 - 2^{\alpha}. \tag{10}$$

As for FF, AF assumes values near unity for Poisson processes.

The AF represents the most used measure of the clustering of fire point processes and was employed in many study-cases worldwide.

Figure 5 shows the AF(T) in log–log scales for the 1997–2003 fire sequence in an area of central Italy (Telesca and Lasaponara 2006a, b, c). The analysis of this AF curve can be considered as paradigmatic because it reveals several features of the fire regime. First of all, the non-Poissonianity of the sequence, since the AF curve is not flat for all the timescales *T*. Then, the time dynamics of the fire sequence is characterized by the presence of periodicities, indicated by the drops in the AF curve (indicated by arrows in Fig. 5); three periodic components are clearly detected at 12, 24 h, and about 3 months. The first two frequencies can be put in relation to the semidiurnal and diurnal meteorological cycle linked with the state of the dead fuel moisture content of open woodland fuel, in response to the normal diurnal weather changes, such as the rise and fall of temperature and solar radiation. The third frequency is connected with the typical seasonal variability of the vegetation, in particular grass, which has an important influence on the ignition and spreading of fires. Two scaling regions (given by the linear parts of the log–log AF curve) exist: one ranging between ~ 1.2 days and ~ 13 days, with scaling exponent ~ 0.8; the other ranging between ~ 13 days and ~ 42 days, with scaling exponent ~ 1.55. The presence of two different scaling regions indicates that two different mechanisms co-exist (due to mixed natural and anthropogenic causes), and the different values of the scaling exponent suggest different strengths of the temporal fluctuations of the fire sequence. The presence of scaling in the AF statistics evidences the self-organization of the fire regime. Fires have a direct impact on vegetation, which, in turn, contributes to the future fire activity (Turner 1898). The existence of feedback mechanisms involving both fires and the ecological patterns (vegetation type, age, physiognomy, etc.) gives rise to correlation structures and memory phenomena, identified by the time-scaling behavior. The vegetation patterns constrain and at the same time are constrained by the processes that generate them. A fire occurring in an area, that was never burned before, creates a pattern of burned and unburned vegetation patches, which will influence the occurrence of the next fire within a continuous feedback dynamics (Malamud et al. 2005; Gill et al. 2003).

Figure 6 shows the AF(*T*) of the 1992–2007 fire sequence in a fire vulnerable area of Patagonia (Argentina) (Ghermandi et al. 2008). The AF pattern is even more complex showing three time-scaling regions (given by the linear parts of the log–log AF curve): the first ranging between ~ 1 day and ~ 6 days, with scaling exponent ~ 0.5; the second ranging between ~ 6 days and ~ 1 month, with scaling exponent ~ 1.1; the third ranging between ~ 1 month and ~ 4 months, with scaling exponent ~ 1.7. The crossover timescales of 6 days and 1 month could have probably an anthropogenic nature. The crossover at about 4 months could be connected with the mean duration of the fire season (occurring in the austral summer). The time dynamics of the Patagonia fire sequence is characterized by the presence of periodicities, shown by the drops in the AF curve at about ½ year (clearly connected with the typical seasonal variability, due to cumulative effects of weather, climate as well as normal bio-physiological life cycles), and at about 1.1 years (related to the yearly cycle of vegetation, connected with the meteorological and climatic yearly cycles).

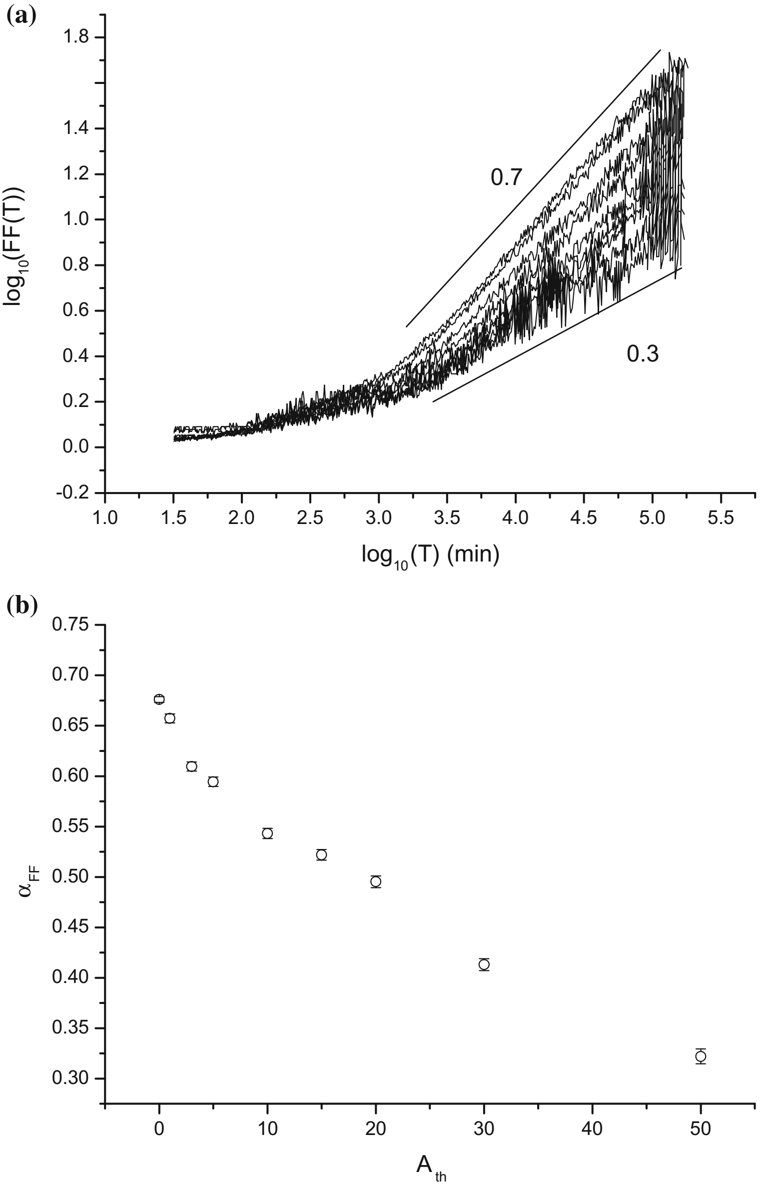

Fig. 5 Variation of the FF of the fire sequence in Gargano region (southern Italy) with the threshold burned area A_{th}. **a** Log–log plot of the FF curves varying the threshold burned area A_{th}; all the FF curves show clear linear behavior from the timescale $T > 10^{3.5}$ min. **b** Dependence of the scaling exponent α_{FF} on the threshold burned area A_{th}; α_{FF} decreases with the increase of the threshold area A_{th} from approximately 0.7 to 0.3, with a mean value (± standard deviation) of 0.5 (± 0.1). (Telesca et al. 2005)

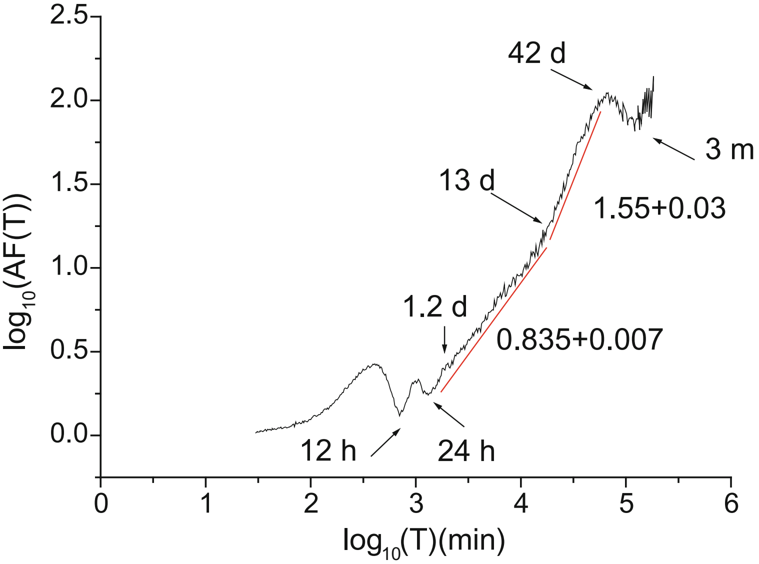

Fig. 6 AF of the fire sequence in Tuscany region (central Italy) from 1997 to 2003 (Telesca and Lasaponara 2006a, b, c)

Figure 7 shows the AF(*T*) for a very long record of forest fires occurred in Ticino (Switzerland) from 1969 to 2008 (Telesca et al. 2010). Different time regimes co-exist: Poissonian behavior at small and large timescales (the AF is almost

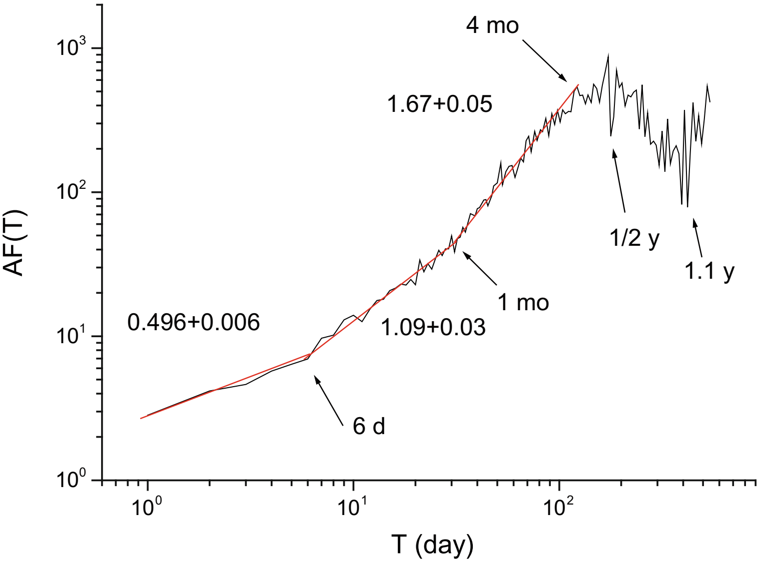

Fig. 7 AF of the fire sequence in Patagonia (Argentina) from 1992 to 2007 (Ghermandi et al. 2008). © 2008 Worldscientific

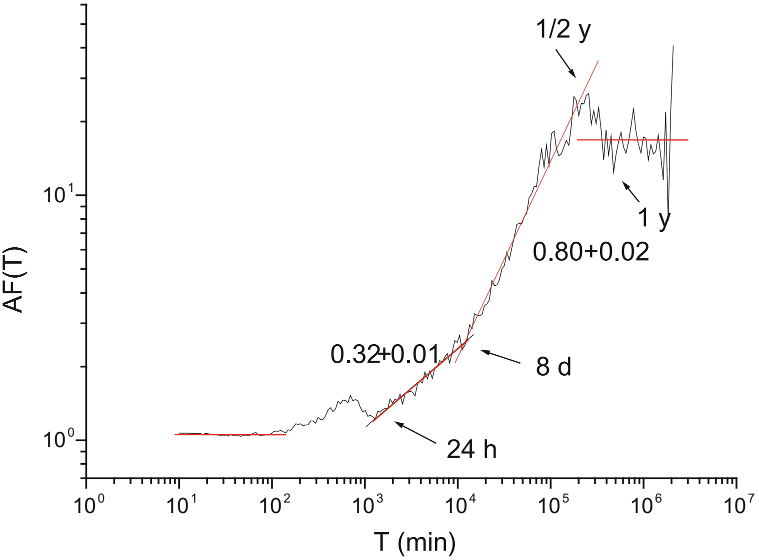

Fig. 8 AF of the fire sequence in Ticino (Switzerland) from 1969 to 2008 (Telesca et al. 2010)

constant), two scaling regions with scaling exponents about 0.32 between 1 and 8 days, and about 0.8 between 8 days and 1/2 year. The crossover at about 8 days could be related to anthropic activities (Wang et al. 2010). Then daily and annual periodicities, indicated by the two drops in the AF curve, are also typical features of the sequence of forest fires.

The correlation between the occurrence of fires and the meteorological conditions was investigated by using the AF for both the point process of the fires and the point process of the relative humidity, the last one obtained after fixing a threshold and considering all humidity values below a certain threshold. Wang et al. (2010) compared the AF(*T*) of the relative humidity point process (with a threshold of 60 %) measured at Miyakonojo (Japan) between 1998 and 1999 (Figs. 8 and 9) with that of the forest fire point process recorded in Japan (Fig. 10) (from Song et al. (2005)), a fire in Japan has a good probability to occur if the average humidity is smaller than 60 %).

It can be observed that the humidity (Fig. 9) has the same scaling properties shown by fires (Fig. 10), with, moreover, the presence of the daily cycle. This result validates the existence of a strong link between weather and fires, and it is very likely that the daily humidity cycle determines the daily fire periodicity.

2.2.5 Count-Based Periodogram (PG)

The count-based PG (Teich et al. 1997), that is the PG of the sequence of the counts, is another statistical measure that allows estimating the fractal exponent α.

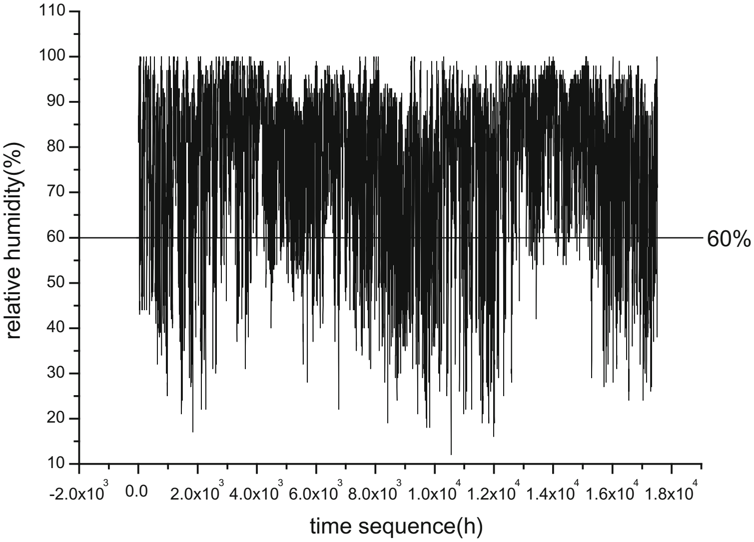

Fig. 9 Relative humidity recorded at Miyakonojo (Japan) from 1998 to 1999 (Wang et al. 2010)

This measure performs an estimate of the power spectral density, which gives information on how the power of the process is concentrated at various frequency bands. The calculation of the PG by means of a count-based approach implies the

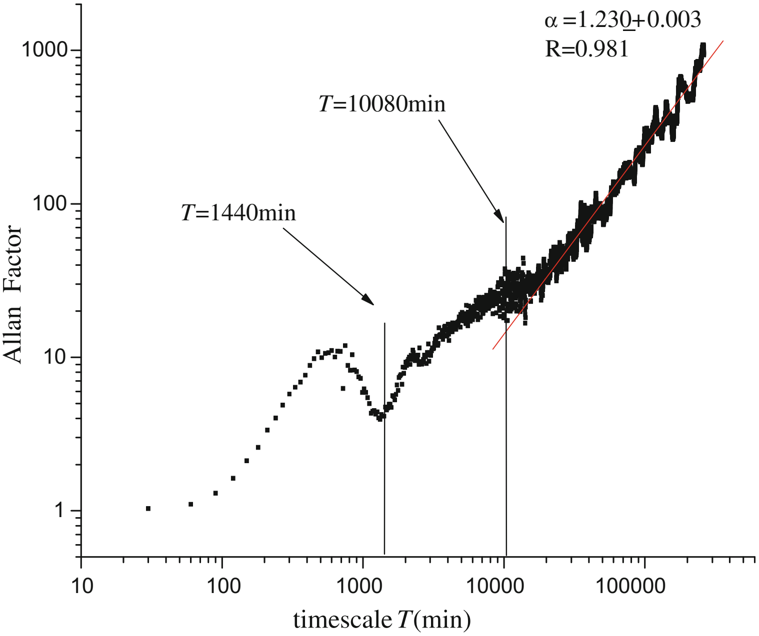

Fig. 10 AF of the forest fire sequence from 1998 to 1999 (Wang et al. 2010)

division of the total observation period into a number N of nonoverlapping windows of length T_W. The sequence of the counts is then Fourier transformed and the PG is obtained by the squares of the coefficients of the Fourier representation of the series of counts. Generally, in order to use the Fast Fourier Transform (FFT) the number N of the windows of duration T_W is a power of 2. For point processes with scaling properties the PG decreases as a power-law function of the frequency f over a significant range of frequencies, $S(f) \propto f^{-\alpha}$. Of course, for a finite size fractal process the power spectral density behaves as an inverse power-law function in a limited range of frequencies, approaching an asymptotic value at high frequencies, at which the behavior of the process can be considered Poissonian. The numerical value of α is an indicator of the presence of clusterization in the process (Thurner et al. 1997). If the point process is Poissonian, the occurrence times are uncorrelated; for this memoryless process, the PG is approximately flat for any frequency bands and $\alpha \approx 0$. On the other side, $\alpha \neq 0$ is typical of point processes with scaling behavior. This method introduces a bias at higher frequencies, since the fine time resolution information is lost as a result of the minimum count-window size. But, the estimation of the exponent α principally involves lower frequencies where this bias is negligible.

Figure 11 shows an example of the application of PG measure for the point process of Anshan city (China) fires. Each plot shows the AF curves for the original sequence (black curve) and for a random point process (blue curve) sharing with the original one the same probability density function of the interevent times. The random sequence is obtained shuffling the interevent time series of the original sequence and then forming the corresponding point process. Each AF curve is obtained varying the parameter T_W (and hence, the number of n overlapping windows N) from 9858 to 615 min. It is evident that if the scaling exponent of shuffled sequence does not depend on the length of the window (the scaling exponent is approximately around 0.3 in all cases), this does not apply to the original sequence, whose scaling exponent decreases from about 0.9 when the window length is the largest to about 0.5 when the window length is the smallest.

This indicates how careful the analysis of the scaling properties of the fire point process has to be done when using this measure.

2.2.6 Multifractal Detrended Fluctuation Analysis

Multifractals are characterized by high variability on a wide range of temporal scales, associated to intermittent fluctuations and long-range power-law correlations. Many phenomena show multifractality (Currenti et al. 2005; Telesca et al. 2001). They are generally characterized by sudden bursts of high-frequency fluctuations, thus evidencing the presence of different scaling behaviors for different intensities of fluctuations. The MF-DFA is an extension of the DFA. The only modification concerns the fluctuation function, which becomes

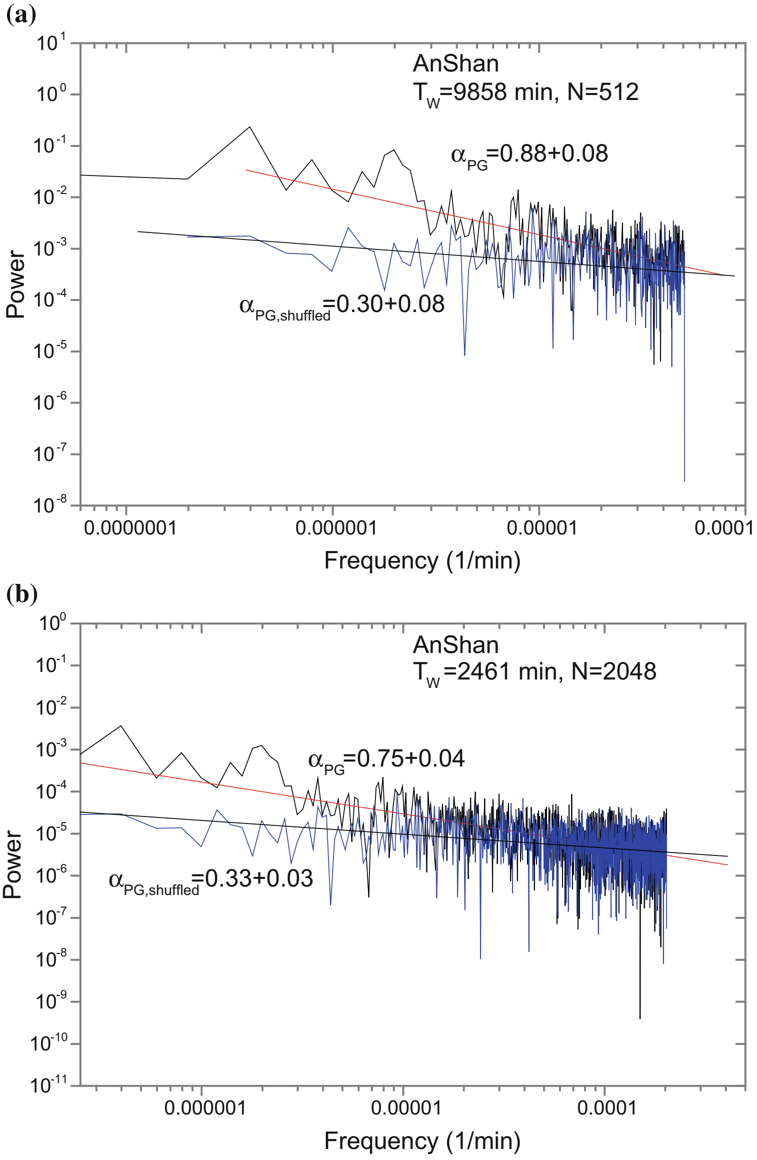

Fig. 11 PG for the original (*black*) and the shuffled (*blue*) city-fire sequences (Telesca and Song 2011)

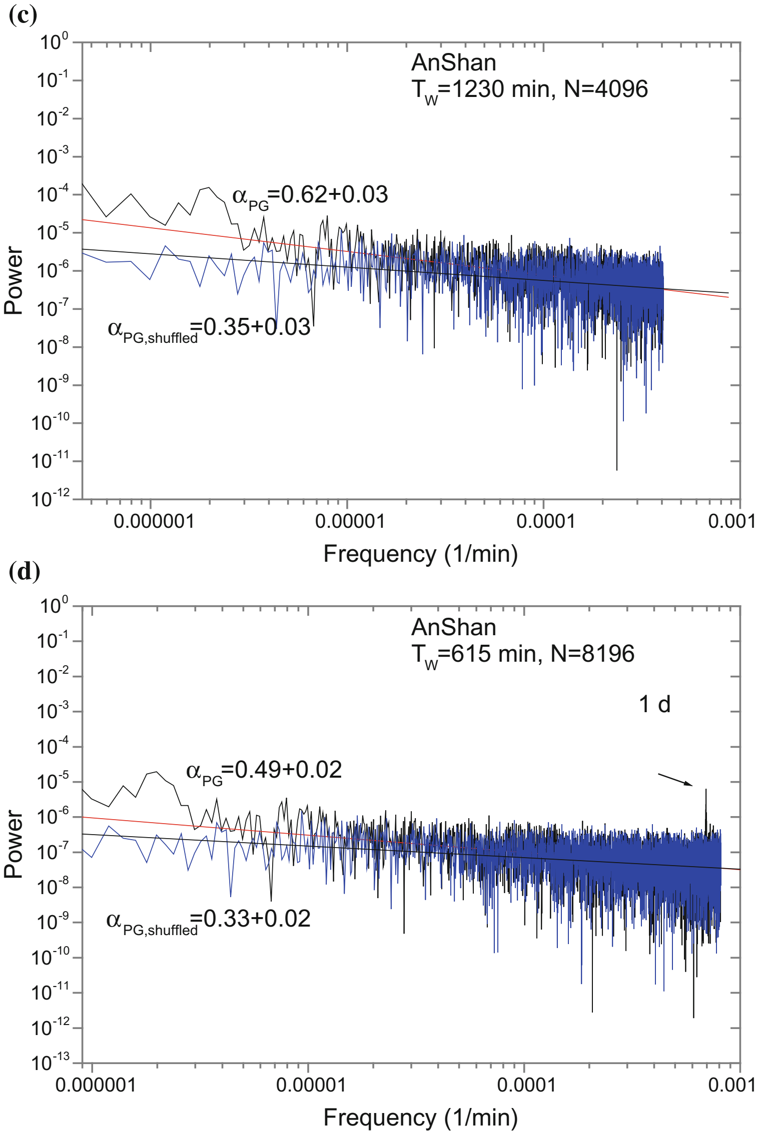

Fig. 11 (continued)

$$F_q(s) = \left\{ \frac{1}{N_S} \sum_{v=1}^{N_S} \left[F^2(s,v) \right]^{\frac{q}{2}} \right\}^{\frac{1}{q}} \tag{11}$$

where $v = 1,\ldots,N_S$, N_S is the number of nonoverlapping windows of duration s and the index variable q represents the moment order, whose meaning will be detailed below. Varying the timescale s, $F_q(s)$ will increase with increasing s. Then analyzing log–log plots $F_q(s)$ versus s for each value of q, we determine the scaling behavior of the fluctuation functions

$$F_q(s) \propto s^{h(q)}. \tag{12}$$

Monofractal time series are characterized by $h(q)$ independent of q, also called generalized Hurst exponent (Kantelhardt et al. 2002). The different scaling of small and large fluctuations will yield a significant dependence of $h(q)$ on q. For positive q, the segments v with large variance (i.e., large deviation from the corresponding fit) will dominate the average $F_q(s)$. Therefore, if q is positive, $h(q)$ describes the scaling behavior of the segments with large fluctuations; and generally, large fluctuations are characterized by a smaller scaling exponent $h(q)$ for multifractal time series. For negative q, the segments v with small variance will dominate the average $F_q(s)$. Thus, for negative q values, the scaling exponent $h(q)$ describes the scaling behavior of segments with small fluctuations, usually characterized by a larger scaling exponent.

The computation of the multifractal spectrum by means of the Legendre transform can be performed. The multifractal scaling exponents $h(q)$ defined in Eq. 8 are directly related to the scaling exponents $\tau(q)$ defined by the standard partition function multifractal formalism (Kantelhardt et al. 2002)

$$\tau(q) = qh(q) - 1. \tag{13}$$

Monofractal series with long-range correlations are characterized by linearly dependent q-order exponents $\tau(q)$, i.e., the exponents $\tau(q)$ of different moments q are linearly dependent on q

$$\tau(q) = Hq - 1, \tag{14}$$

because $h(q)$ is independent of q for monofractal series. Long-range correlated multifractal signals have a multiple Hurst exponent, i.e., the generalized Hurst exponent $h(q)$,

$$h(q) = d\tau/dq \neq \text{const}, \tag{15}$$

where $\tau(q)$ depends nonlinearly on q.

The singularity spectrum $f(\alpha)$ is related to $\tau(q)$ by means of the Legendre transform,

$$\alpha = \frac{d\tau}{dq} \tag{16}$$

$$f(\alpha) = q\alpha - \tau(q), \tag{17}$$

where α is the Hölder exponent and $f(\alpha)$ indicates the dimension of the subset of the series that is characterized by α. The singularity spectrum quantifies in detail the long-range correlation properties of a time series. The multifractal spectrum gives information about the relative importance of various fractal exponents present in the series. In particular, the width of the spectrum indicates the range of present exponents. The width of the spectrum W is a measure of how wide the range of fractal exponents found in the signal is; and, thus, it measures the degree of multifractality of the series. The wider the range of possible fractal exponents, the "richer" is the process in structure.

In order to understand the type of multifractality underlying the q-dependence of $h(q)$, the random shuffle method can be applied. Generally, two different types of multifractality in time series can be discriminated: (i) due to a broad probability density function and (ii) due to different long-range correlations for small and large fluctuations. In the shuffling procedure the values are put into random order, and although all correlations are destroyed, the probability density function remains unchanged. Hence the shuffled series coming from multifractals of type (ii) will exhibit simple random behavior with $h_{\text{shuf}}(q) = 0.5$. While those coming from multifractals of type (i) will show $h(q) = h_{\text{shuf}}(q)$, since the multifractality depends on the probability density (Kantelhardt et al. 2002). If both types of multifractality characterize the time series, then the shuffled series will show weaker multifractality than the original one.

In cases of fire point processes, the multifractality can be investigated using the representation of the interevent times. Figure 12 shows the $h(q)$–q relationships for the original and shuffled sequence of fires recorded in Anshan city (China) (Telesca and Song 2011) for q varying between −10 and 10. The original sequence is characterized by a larger multifractality than that of the shuffled one. Furthermore, Fig. 13, which shows the Legendre spectrum for both series, reveals that the width of the multifractal spectrum for the original series is larger than that of the shuffled series. Furthermore, since the $h(q)$-spectrum of the shuffled series is different from that of the original one, the multifractality of the city-fire series is given mainly by the different long-range correlations for the small and large interevent fluctuations. Moreover, the Legendre spectrum of the original sequence appears left-skewed, which indicates an asymmetrical weight between the small and the large fluctuations of the interevent times, in favor of the large fluctuations that dominate the multifractality of the fires.

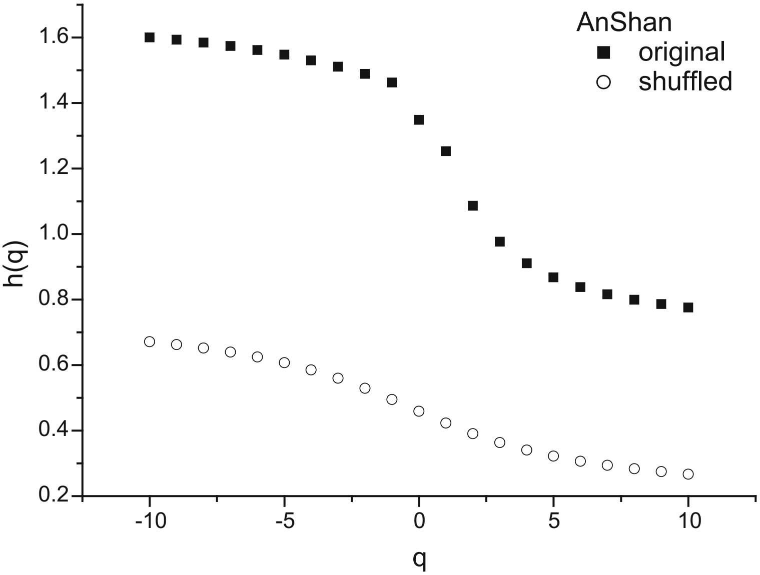

Fig. 12 $h(q)$–q relationship for the original and shuffled city-fire sequence (Telesca and Song 2011)

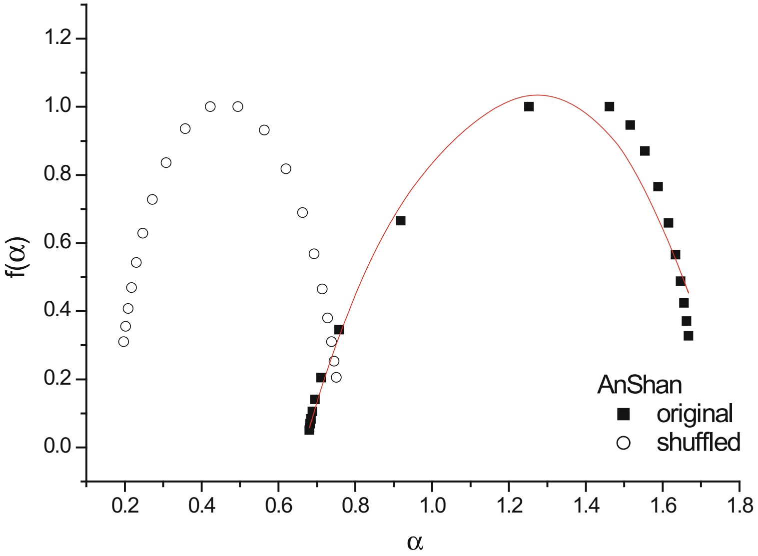

Fig. 13 Legendre spectrum $f(\alpha)$–α for the original and shuffled city-fire sequence. The *red line* is the parabola fitting the spectrum of the original series (Telesca and Song 2011)

3 Fires in Satellite Time Series

Remote sensing techniques allow to investigate properties and dynamics of ecosystems and their interannual variability at different temporal and spatial scales. Due to their large coverage, high revisitation frequencies and a reliable consistency, the estimations of fire-induced variability in ecosystems can be effectively approached by using satellite data. The investigation of fires in satellite time series has been carried out mainly in analyzing the vegetation characteristics affected by fires. The role of vegetation is well known in terms of its ecological impacts. Variations in the composition and distribution of vegetation can arise in response to natural hazards and anthropic stresses and represent one of the main sources of systematic environmental change on local, regional, or global scale (Crowling et al. 1996). Fire is one of the most critical stresses for vegetation. The effects of fires on soil, plants, landscape, and ecosystems depend on many factors, among them fire frequency, fire severity, and plant resistance (Huemmrich et al. 1999). Characterizing vegetation post-fire behavior is a crucial issue to estimate the fire resilience that is the capability of vegetation to recover after fire. Satellite technologies can be profitably employed to study the time dynamics of vegetation re-growth after fire disturbance at different temporal fluctuations. Moreover, fire-induced dynamical processes in vegetation are very complex, since they affect the complex soil–surface–atmosphere interactions, due to feedback mechanisms involving human activity, ecological patterns, and different subsystems of climate (Telesca and Lasaponara 2008). Therefore, the vegetation patterns constrain fires and at the same time are constrained by the fire processes that influence them. Therefore, the use of fractal methods to investigate the vegetation characteristics in fire-affected and fire unaffected sites or to discriminate vegetation patterns before and after fire occurrence has represented an important methodological innovation in the recent years.

The remote sensing of vegetation has been traditionally performed by means of several vegetation indices obtained through vegetation spectral properties that measure the biomass or vegetative vigor. The vegetation indices operate by contrasting intense chlorophyll pigment absorption in the red against the high reflectance of leaf mesophyll in the near infrared. The simplest form of vegetation index is the ratio between two digital values from these two spectral bands. The most widely used index is the NDVI (Campbell 1987). The NDVI informs about the plant photosynthetic activity and has been found to be related to the green leaf area index and the fraction of photosynthetically active radiation absorbed by vegetation. Therefore variations in NDVI values reveal variations in vegetation composition and dynamics (Myneni et al. 1996).

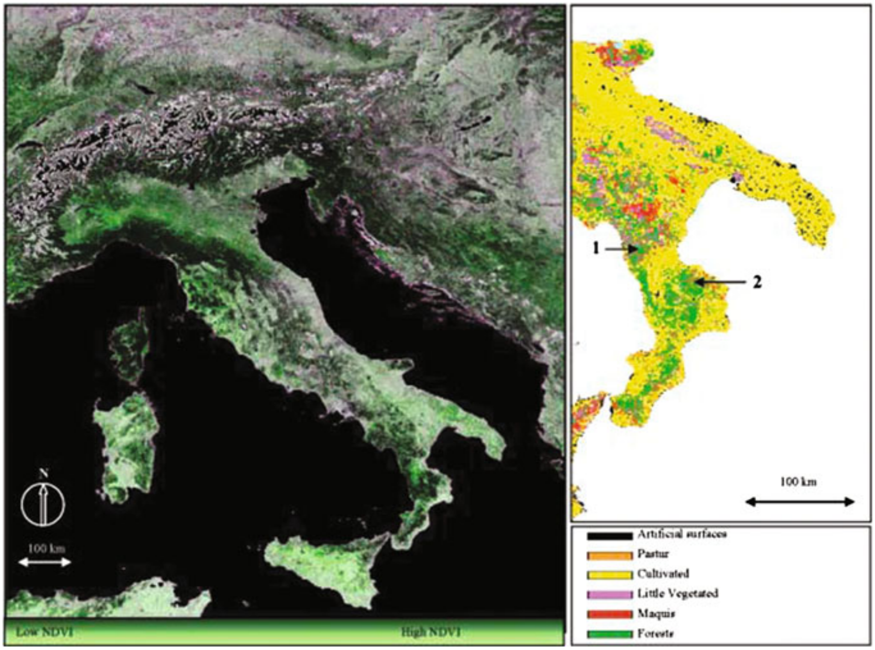

Fig. 14 Location of the forest test sites, fire unaffected Orsomarso (*1*) and fire-affected Bocchigliero (*2*) NDVI (*left*) and Corine land-cover map (*right*) (Telesca and Lasaponara 2006a, b, c)

Telesca and Lasaponara (2006a, b, c) applied the DFA method on the decadal satellite SPOT-VEGETATION pixel time series of NDVI covering two vegetation sites in southern Italy, one affected and the other unaffected by fire, in order to detect scaling differences in the time fluctuations of the NDVI. The two sites are shown in Fig. 14 and an example of the pixel time series is shown in Fig. 15.

The NDVI shows a periodical behavior that follows the yearly climatological cycle. However, before applying the DFA, it is necessary to remove such seasonal fluctuation by removing the decadal mean (the decadal mean is calculated for each decade, e.g., first decade of January, by averaging over all years in the record), obtaining the $\mathrm{NDVI_d}$ (Fig. 16). The DFA performed on the time variation of $\mathrm{NDVI_d}$ of the two pixels indicates a value of the scaling exponents larger than 0.5 (Fig. 17) that suggests that the temporal fluctuations of both time series are positively correlated or persistent. And this suggests that the investigated ecosystems are governed by positive feedback mechanisms, which tend to destabilize the system under external forces. The feedback mechanisms express a positive circular causality that acts as a growth-generating

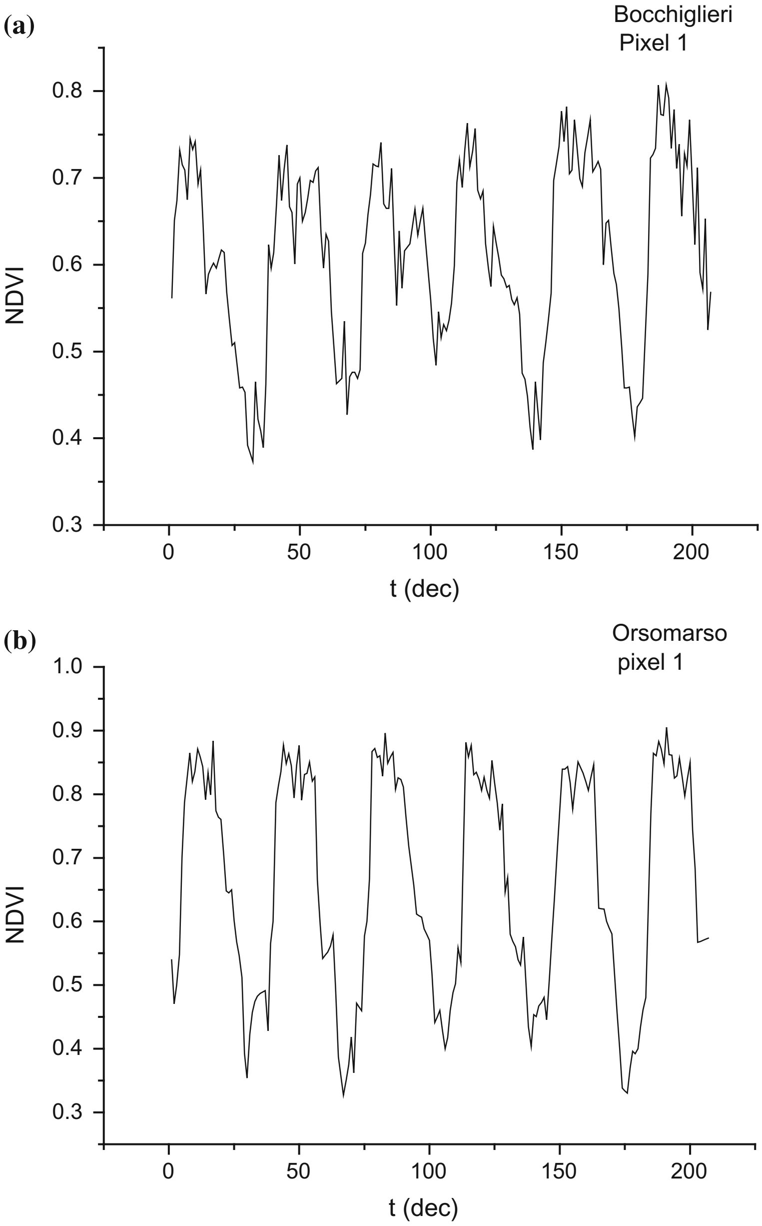

Fig. 15 NDVI decadal SPOT VEGETATION satellite data of a pixel from 1998 to 2003 for **a** Bocchiglieri site and **b** Orsomarso site (Telesca and Lasaponara 2006a, b, c)

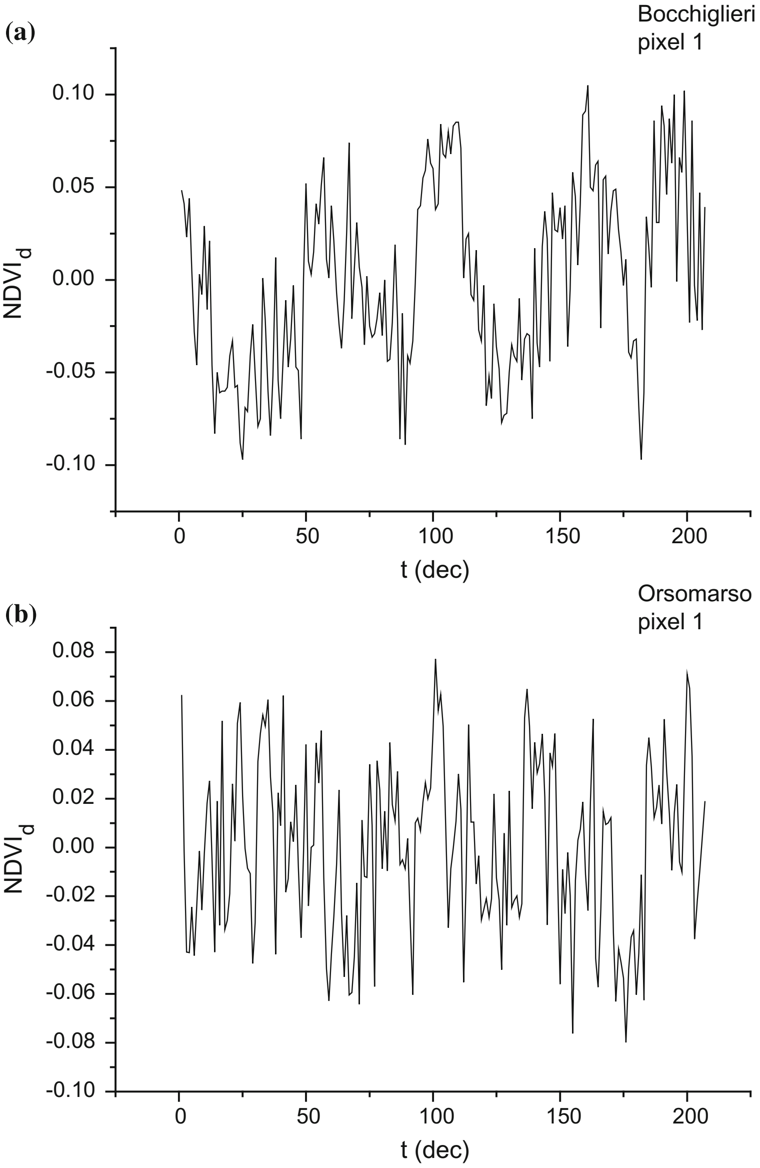

Fig. 16 NDVI$_d$ decadal SPOT VEGETATION satellite data of a pixel from 1998 to 2003 for **a** Bocchiglieri site and **b** Orsomarso site (Telesca and Lasaponara 2006a, b, c)

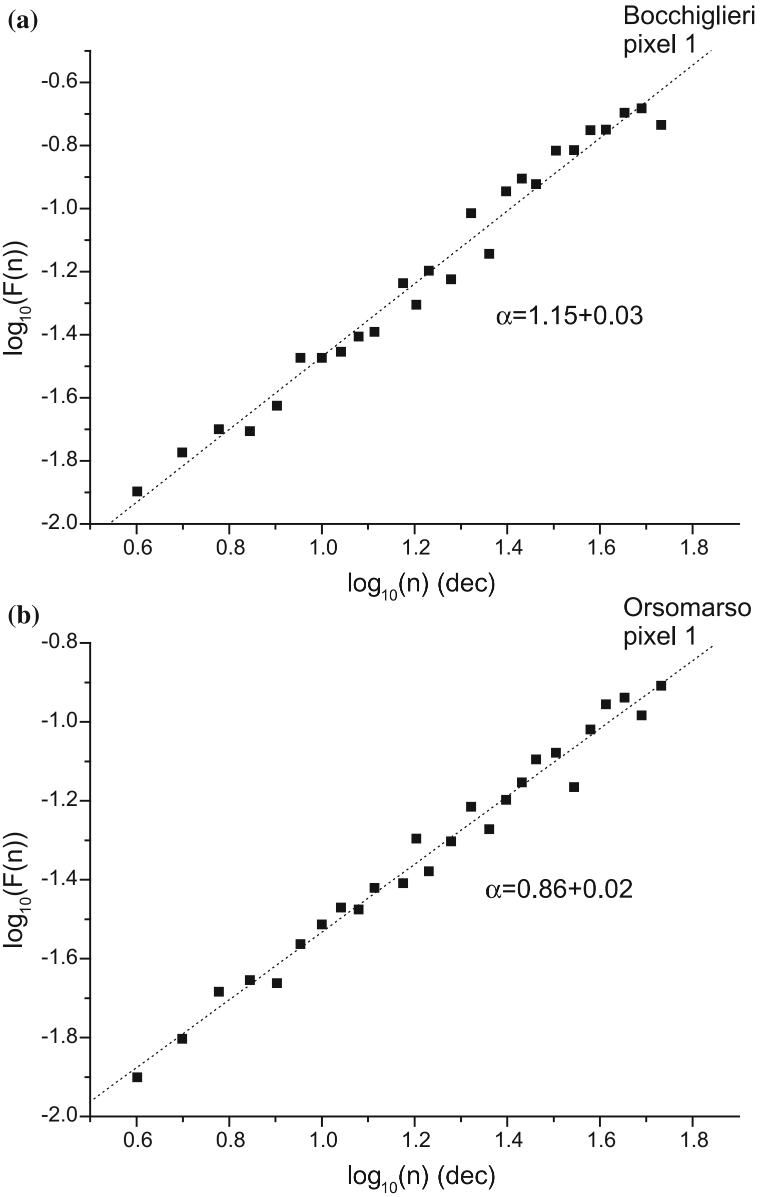

Fig. 17 DFA of the pixel time series shown in Fig. 16 (Telesca and Lasaponara 2006a, b, c)

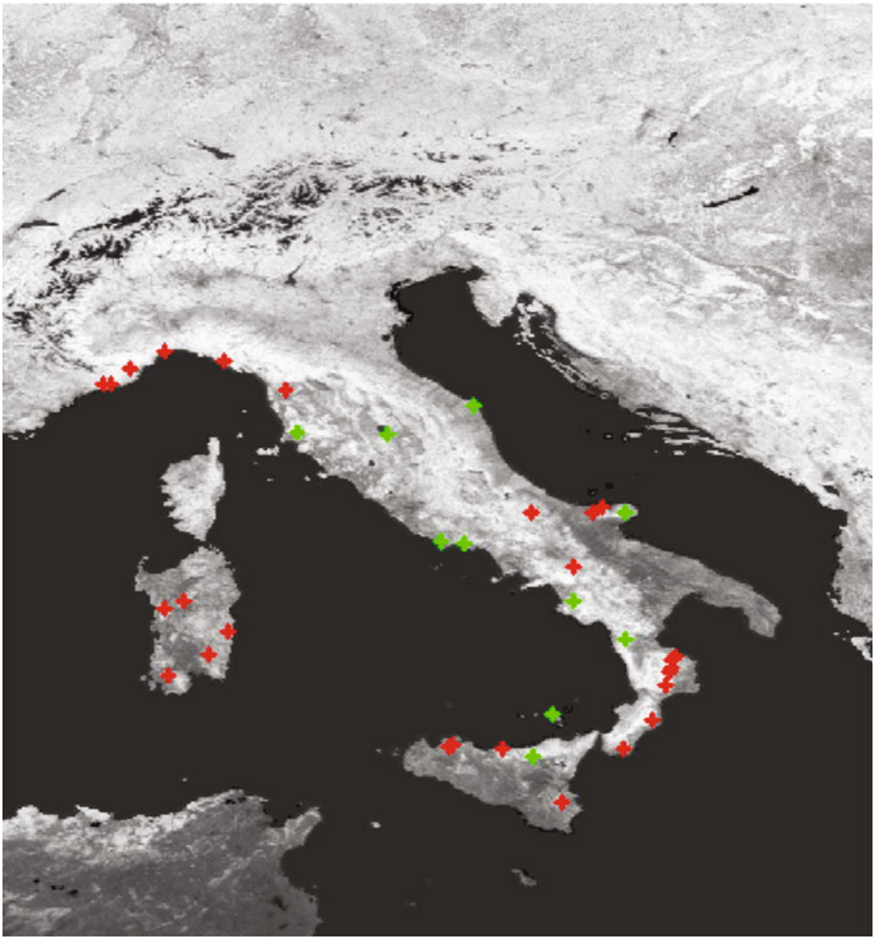

Fig. 18 Locations of the investigated burned (*red crosses*) and unburned (*green crosses*) test sites (Telesca et al. 2007)

phenomenon and therefore drives unstable patterns. Therefore the vegetational processes possess memory of external shocks, which drive the time dynamics of the vegetational covers (Telesca and Lasaponara 2006a, b, c).

Different types of vegetation covers (forest, shrub-land, and mixed) were analyzed by Telesca and Lasaponara (2005), who found that independently of the vegetation cover, the scaling exponents for fire-affected pixels range around the mean value of ~1.14, while those for fire-unaffected pixels vary around the mean value of ~0.77; and this indicates that fires play an important role in the temporal evolution of vegetation. This suggests the inherent character of the fire-related vegetation recovery processes, indicating the existence of positive relation between

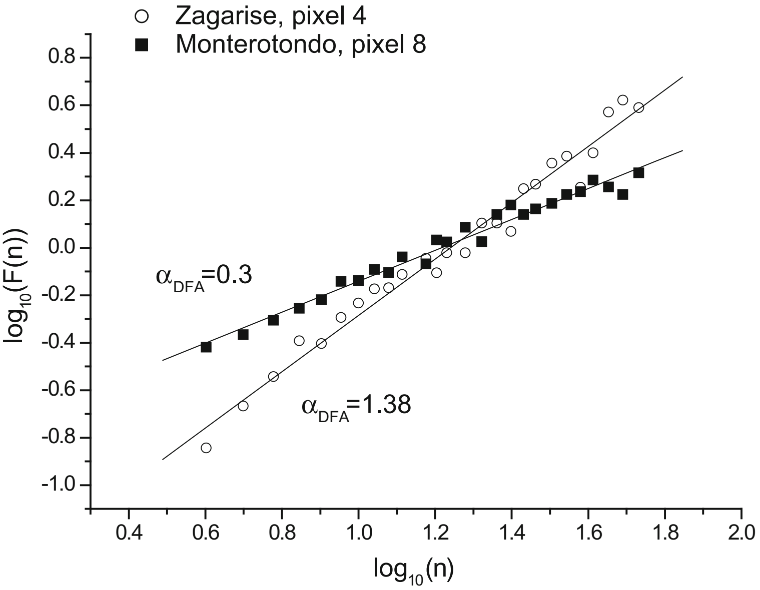

Fig. 19 Example of DFA performed on two pixel time series of two sites: fire-affected (Zagarise) and fire unaffected (Monterotondo) (Telesca et al. 2007)

the amounts of burned and regenerated biomass. Fires drive more unstable patterns in vegetational covers, leading to a more efficient fire-induced vegetation recovery process.

Telesca et al. (2007) extended such a study to the whole Italian territory (Fig. 18) where a further standardization was performed on the NDVI data, removing not only the decadal mean but also dividing by the decadal standard deviation. An example of application of DFA on two pixel NDVI time series is shown in Fig. 19.

Figure 20 shows the scaling exponents of the pixel time series for the sites shown in Fig. 18. The DFA exponents range around the mean value of ~1.22 for fire-affected sites, while those for fire-unaffected sites vary around the mean value of ~0.65. The fire-affected sites show significantly larger exponents than those calculated for the fire-unaffected sites. From the ecological point of view, the behavior of the exponent indicates the resilience of burned ecosystem (the tendency of return to the pre-fire initial conditions). In the burned sites the very strong perturbation causes the persistence of signal indicated by the exponent larger than those obtained for unburned sites, pointing out to the role played by fires in changing its vegetation dynamics (Telesca et al. 2007).

Fig. 20 DFA exponents of the pixel time series corresponding to the sites shown in Fig. 18 (Telesca et al. 2007)

The behavioral trends in the pre- and post-fire dynamics of vegetation were analyzed by Telesca and Lasaponara (2006a, b, c) by applying the DFA to five pre- and post-fire subseries of the decadal maximum value composite SPOT-VGT NDVI data of a forest site of Ventimiglia (northern Italy), mainly covered by *Quercus ilex* and *Quercus pubescens*, affected by a fire occurred on September 9, 2001. Figure 21 shows that the scaling exponents for post-fire subseries range around the mean value of ~1.46, while those for pre-fire pixels vary around the mean value of ~1.0.

The fire increased the persistence of vegetation, and this indicates that more unstable patterns have been induced in vegetation dynamics, after fire disturbance. The value of the DFA exponent, after the fire occurrence, can be used as a quantitative indicator of the vegetation resilience. The vegetation corresponds to Mediterranean Quercus forests, dominated by perennial re-sprouting species that recuperate the biomass rapidly post-fire; and due to the disruptive perturbation caused by fire disturbance, the persistence of signal indicates by the $\alpha > 1.4$ in the burned sites the strong trend of ecosystem to accumulate biomass rapidly (Telesca and Lasaponara 2006a, b, c).

The recovery capacity is slightly reduced after two consecutive fires. Figure 22 shows the mean scaling exponent calculated for the three NDVI time series of

Fig. 21 DFA exponents of the pre- and post-fire pixel time series in Ventimiglia site (Telesca and Lasaponara 2006a, b, c)

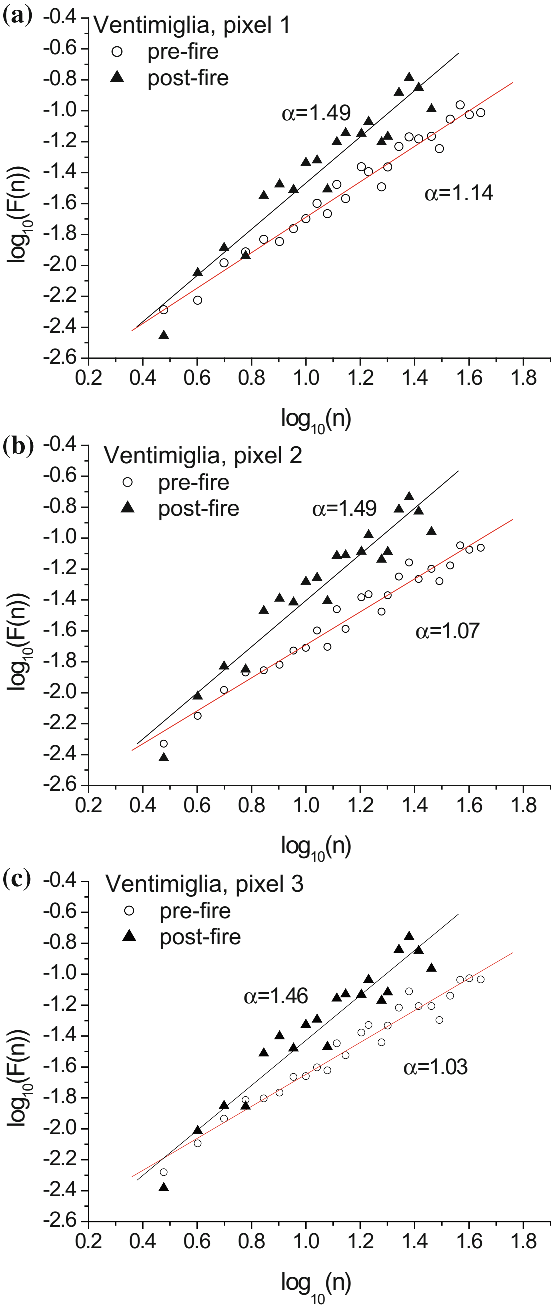

Fig. 21 (continued)

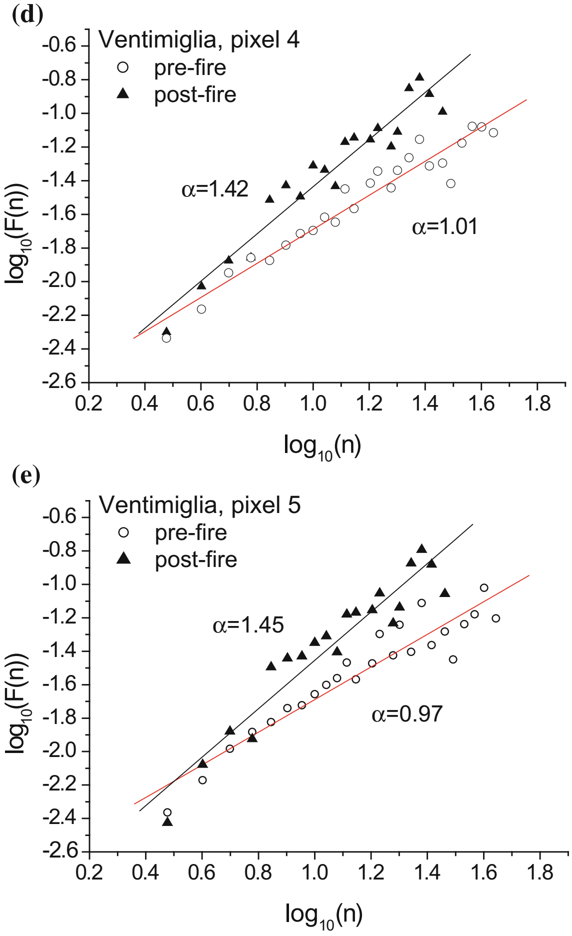

pixels not affected by any fire, those included within the two fires, and those after the second fire in Bolotana (southern Italy) (Telesca and Lasaponara 2008). It is clear the discrimination between the three status of vegetation, with the lowest persistent degree for the unburned pixels, the highest persistent degree for the pixel time series between the two fires. After the second fire the vegetation lowers its resilience, due to a more stable response of vegetation to the second fire stress.

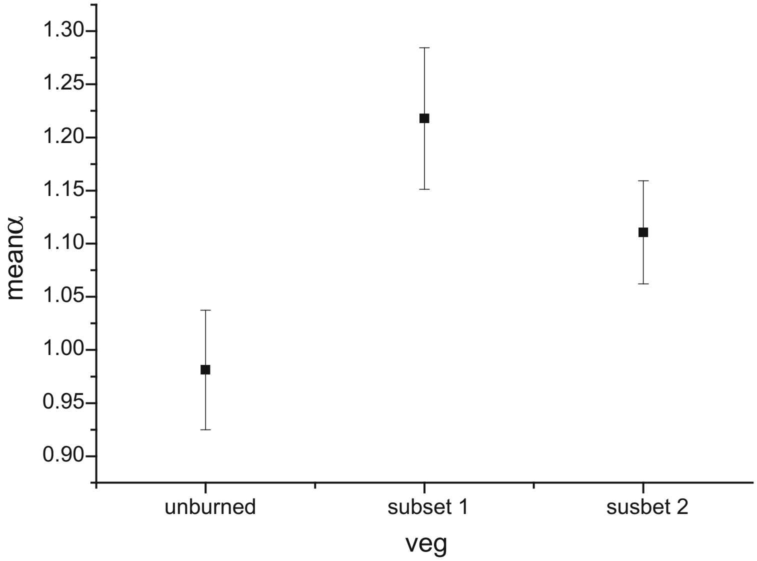

Fig. 22 Mean and standard deviation of the DFA exponents calculated for the Bolotana pixels (Telesca and Lasaponara 2008)

4 Conclusions

Investigating fire regime characteristics can support forest fire management for several activities including fire prevision and prevention. The knowledge of the temporal dynamics of fires is crucial for understanding lightning causes of forest fires, improving fire occurrence prediction and fire management planning, investigating the role of fires in landscape processes, land-cover changes and degradation, improving predictive models of plant succession following wildfires, etc.

The relevance of applying temporal fractal analyses to fire distributions or time-continuous signals sensitive to fires consists in a better understanding of the underlying dynamical mechanisms.

Fire processes show different scaling regimes, suggesting the existence of different underlying dynamical mechanisms, with different strengths of the power-law fluctuations, indicated by the quantitative value of the scaling exponent, which suggests a persistent behavior.

The different mechanisms are very likely mixed natural and anthropogenic causes. The periodicity at about 1 day observed in several cases of fire distributions worldwide can be put in relationship with both the diurnal meteorological cycle and the diurnal anthropogenic behavior. Pippen (1999) and Plucinski (1999) found a diurnal variation in the state of the dead fuel moisture content of open woodland fuel, in response to the normal diurnal weather changes, such as the rise and fall of temperature and solar radiation. Even the relative humidity sequence shows a daily cycle, thus being one of the causes of the daily cycle in the fire sequence (Wang et al. 2010). The annual frequency that characterizes fire sequences is linked with the typical seasonal variability, due to cumulative effects of weather, climate as well as normal bio-physiological life cycles. The vegetation, in particular the litter and the herb layer in the forest stand understory that have an important influence on the ignition and spreading of fires, has a typical annual seasonal growth cycle.

Persistence found in NDVI signal means that the investigated vegetation system is governed by positive feedback mechanisms, which tend to destabilize the system under external forces. Within this feedback framework, the concept of persistence is very useful in order to characterize the stability/instability properties of vegetation dynamics. It was observed that fires increase the persistence of vegetation. This indicates that more unstable patterns are induced in vegetation dynamics, after fire disturbance. And the value of the scaling exponent, after the fire occurrence, can be used as a quantitative indicator of the capability of vegetation recovery or resilience, indicative of a positive relation between the amounts of burned and regenerated biomass. The ability of vegetation to recover after fire disturbance is crucial in order to avoid or reduce land degradation. Several studies performed on post-fire regeneration in the Mediterranean Basin have found that vegetation communities generally tend to exhibit a rapid regeneration after fire disturbances. Due to the disruptive perturbation caused by fire disturbance, the persistence of NDVI signal indicated by a relatively high value of the scaling exponent in the burned sites indicates the strong trend of ecosystem in accumulating biomass rapidly.

Acknowledgements We thank V.P. Dimri for his invitation to write this overview.

References

Allan DW (1966) Statistics of atomic frequency standards. Proc IEEE 54:221–230

Campbell JB (1987) Introduction to remote sensing. Guildford, New York

Cowling RM, Rundel PW, Lamont BB, Arroyo MK, Arianoutsou M (1996) Plant diversity in mediterranean-climate regions. Trends Ecol Evol 11:362–366

Cox DR, Isham V (1980) Point processes. Chapman and Hall, London

Dimri VP (2000) Application of fractal in earth sciences. In: AA Balkema (ed) USA/Oxford and IBH Pub. Co., New Delhi, p 238

Dimri VP (2005a) Fractal behaviour of the earth system. Springer, New York, p 207

Dimri VP (2005b) Fractals in geophysics and seismology: an introduction, fractal behaviour of the earth system. Springer, New York, pp 1–22

Currenti G, Del Negro C, Lapenna V, Telesca L (2005) Multifractality in local geomagnetic field at Etna volcano, Sicily (southern Italy). Nat Hazards Earth Syst Sci 5:555–559

Ghermandi L, de Torres Curth M, Franzese J, Telesca L (2008) Analysis of time regimes in fire sequences occurred in Patagonia, Argentina. Flutuation Noise Lett 8:L175–L181

Gill AM, Allan G, Yates C (2003) Fire-created patchiness in Australian savannas. Int J Wildland Fire 12:323–331

Havlin S, Amaral LAN, Ashkenazy Y, Goldberger AL, Ivanov PCh, Peng C-K, Stanley HE (1999) Application of statistical physics to heartbeat diagnosis. Phys A 274:99–110

Huemmrich KE, Black TA, Jarvis PG, McCaughey JH, Hall EG (1999) Remote sensing of carbon/water/energy parameters: high temporal resolution NDVI phenology from micrometeorological radiation sensors. J Geophys Res 104:27935–27944

Kantelhardt JW, Zschiegner SA, Koscielny-Bunde E, Havlin S, Bunde A, Stanley HE (2002) Multifractal detrended fluctuation analysis of nonstationary time series. Phys A 316:87–114

Lasaponara R, Santulli A, Telesca L (2005) Time-clustering analysis of forest-fire sequences of southern Italy. Chaos Solitons Fractals 24:139–149

Lowen SB, Teich MC (1993) Estimating the dimension of a fractal point process. SPIE Chaos Biol Med 2036:64–67

Lowen SB, Teich MC (1995) Estimation and simulation of fractal stochastic point processes. Fractals 3:183–210

Malamud BD, Millington JDA, Perry GLW (2005) Characterizing wildfire regimes in the USA. Proc Natl Acad Sci USA 102:4694–4699

Mandelbrot BB (1982) The fractal geometry of Nature. Freeman Press, San Francisco

Myneni RB, Los SO, Tucker CJ (1996) Satellite-based identification of linked vegetation index and sea surface temperature anomaly areas from 1982 to 1990 for Africa, Australia and South America. Geophys Res Lett 23:729–732

Peng C-K, Havlin S, Stanley HE, Goldberger AL (1995) Quantification of scaling exponents and crossover phenomena in nonstationary heartbeat time series. CHAOS 5:82–87

Pippen BG (1999) Predicting fine fuel moisture in shrubby vegetation, Honours thesis, Australian National University

Plucinski MP (1999) The investigation of factors governing ignition and development of fires in heatland vegetation, Ph.D. thesis, University of New South Wales, ADFA

Song W, Wang J, Satoh K (2005) Distribution and correlation analysis of wildfire and weather data in Japan. Prog Nat Sci 15:363–367

Teich MC, Heneghan C, Lowen SB, Turcott RG (1996) Estimating the fractal exponent of point processes in bilogical systems using wavelet- and fourier-transform methods. In: A Aldroubi, M Unser (eds) Wavelets in medicine and biology. CRC Press, Boca Raton, FL, pp 383–412

Teich MC, Heneghan C, Lowen SB, Ozaki T, Kaplan E (1997) Fractal character of the neural spike train in the visual system of the cat. J Opt Soc Am A 14:529–546

Telesca L (2005) Quantifying the time-clustering in SGR1806-20 bursts. Fluctuation Noise Lett 5: L417–L422

Telesca L (2007a) Time-clustering of natural hazards. Nat Hazards 40:593–601

Telesca L (2007b) Identifying time-clustering structures in the sequence of solar flares hard X-ray bursts. Phys A 384:516–521

Telesca L, Bernardi M, Rovelli C (2008) Time-scaling analysis of lightning in Italy. Commun Nonlinear Sci Numer Simul 8:1099–1104

Telesca L, Chen C-C, Lee Y-T (2009a) Scaling behaviour in temporal fluctuations of crustal seismicity in Taiwan. Nat Hazards Earth Syst Sci 9:2067–2071

Telesca L, Cuomo V, Lapenna V, Macchiato M (2001) Intermittent-type temporal fluctuations in seismicity of the Irpinia (southern Italy) region. Geophys Res Lett 28:3765–3768

Telesca L, Lovallo M (2006) Are global terrorist attacks time-correlated? Phys A 362:480–484

Telesca L, Lovallo M (2007) Non-random components in aircraft accidents time series. Phys A 379:459–464

Telesca L, Lovallo M (2008) Analysis of the temporal properties in car accident time series. Phys A 387:3299–3304

Telesca L, Rouai M, Cherkaoui T-E (2009b) Time-clustering behavior in the sequence of the aftershocks of the Al-Hoceima (Morocco) 24 February 2004 earthquake. Nat Hazards Earth Syst Sci 9:2063–2066

Telesca L, Amatulli G, Lasaponara R, Lovallo M, Santulli A (2005) Time-scaling properties in forest-fire sequences observed in Gargano area (southern Italy). Ecol Model 185:531–544

Telesca L, Kanevski M, Tonini M, Boris Pezzatti G, Conedera M (2010) Temporal patterns of fire sequences observed in Canton of Ticino (southern Switzerland). Nat Hazards Earth Syst Sci 10:723–728

Telesca L, Lanorte A, Lasaponara R (2007) Investigating dynamical trends in burned and unburned vegetation covers using SPOT-VGT NDVI data. J Geophys Eng 4(2007):128–138

Telesca L, Lasaponara R (2005) Discriminating dynamical patterns in burned and unburned vegetational covers by using SPOT-VGT NDVI data. Geophys Res Lett 32:L21401

Telesca L, Lasaponara R (2006a) Emergence of temporal regimes in fire sequences. Phys A 359:747–751

Telesca L, Lasaponara R (2006b) Fire-induced variability in satellite SPOT-VGT NDVI vegetational data. Int J Rem Sens 27:3087–3095

Telesca L, Lasaponara R (2006c) Pre- and post-fire behavioral trends revealed in satellite NDVI time series. Geophys Res Lett 33:L14401

Telesca L, Lasaponara R (2008) Analysing vegetation response to two successive fires using satellite spot-vgt normalized difference vegetation index time series. In: Proceedings of the 10th IASTED international conference signal and image processing (SIP 2008), August 18–20, 2008. Kailua-Kona, HI, USA, pp 300–303

Telesca L, Lasaponara R (2010) Analysis of time-scaling properties in forest-fire sequence observed in Italy. Ecol Model 221:90–93

Telesca L, Song W (2011) Time-scaling properties of city fires. Chaos Solitons Fractals 44:558–568

Thurner S, Lowen SB, Feurstein MC, Heneghan C, Feichtinger HC, Teich MC (1997) Analysis, synthesis, and estimation of fractal-rate stochastic point processes. Fractals 5:565–596

Turner MG (1898) Landscape ecology: the effect of pattern on process. Annu Rev Ecol Syst 20:171–197

Viswanathan GM, Peng C-K, Stanley HE, Goldberger AL (1997) Deviations from uniform power law scaling in nonstationary time series. Phys Rev E 55:845–849

Wang J, Song W, Zheng H, Telesca L (2010) Temporal scaling behavior of human-caused fires and their connection to relative humidity of the atmosphere. Ecol Model 221:85–89